MEASUREMENT OF COMPLEX ULTRASHORT LASER PULSES USING FREQUENCY-RESOLVED OPTICAL GATING

A Dissertation
Presented to
The Academic Faculty

by

Lina Xu

In Partial Fulfillment
of the Requirements for the Degree
Doctor of Philosophy in the
School of Physics

Georgia Institute of Technology
August 2009

MEASUREMENT OF COMPLEX ULTRASHORT LASER PULSES

USING FREQUENCY-RESOLVED OPTICAL GATING

Approved by:

Dr. Rick Trebino, Advisor
School of Physics
Georgia Institute of Technology

Dr. John A. Buck
School of Electric & Computer Engineering
Georgia Institute of Technology

Dr. Ahmet Erbil
School of Physics
Georgia Institute of Technology

Dr. Stephen Ralph
School of Electric & Computer Engineering
Georgia Institute of Technology

Dr. Zhigang Jiang
School of Physics
Georgia Institute of Technology

Date Approved: August, 2009

ACKNOWLEDGEMENTS

I would like to express my deep gratitude to my advisor Professor Rick Trebino, who has spent great amount of time and energy in advising my research directions, reviewing my articles, encouraging my study progress. I would also like to extend my gratitude to Professor John A Buck, Ahmet Erbil, Stephen Ralph and Zhigang Jiang for serving on my PhD defense committee.

I would also like to thank Linda Trebino for all the work she has done for our group. She really helped us a lot. I will thank all my family members, including my mother, Shuzhen Ding, my husband, Yang Song, my lovely son, Nathan Song, and my in-laws for their unconditional support, understanding, love and encouragement. I will thank our entire group member Dongjoo, Jake, Pablo, Pam, Peter, Qiang, Selcuk, Vikrant, and Xuan for the wonderful collaboration.

TABLE OF CONTENTS

Page

LIST OF TABLES

LIST OF FIGURES

Page

SUMMARY

This thesis contains three components of research: a detailed study of the performance of Frequency-Resolved Optical Gating (FROG) for measuring complex ultrashort laser pulses, a new method for measuring the arbitrary polarization state of an ultrashort laser pulse using Tomographic Ultrafast Retrieval of Transverse Light E-fields (TURTLE) technique, and new approach for measuring two complex pulses simultaneously using PG blind FROG.

In recent decades, many techniques for measuring the full intensity and phase of ultrashort laser pulses have been proposed. These techniques include: Spectral Interferometry (SI)[1], Temporal Analysis by Dispersing a Pair of Light E-Field (TADPOLE)[2], Spectral Phase Interferometry for direct electric-field reconstruction (SPIDER)[3], and Frequency-Resolved Optical Gating (FROG)[4]. Each technique is actually a class of techniques that includes different variations on the original idea, such as SEA-SPIDER[5], ZAP SPIDER[6] are two variations of SPIDER. But most of these techniques for measuring ultrashort laser pulses either do not yield the complete time-dependent intensity and phase (e.g., autocorrelation), can at best only measure simple pulses (e.g., SPIDER), or need well characterized reference pulse.

In this thesis, we compare the performance of three versions of FROG: second-harmonic-generation (SHG) FROG, polarization-gate (PG) FROG, and cross-correlation FROG (XFROG), the last of which requires a well-characterized reference pulse. We found that the XFROG algorithm converged in all cases and required only one initial guess. The PG FROG algorithm converged for 99% of the moderately complex pulses that we tried, and for over 95% of the most complex pulses (TBP ~ 100). And the SHG

FROG algorithm converged for 95% of the pulses that we tried and for over 80% of the most complex pulses. After some analysis, we found that noise filtering and adding more sampling points to the FROG trace solved the non-converging problems and we got the retrieval to eventually converging for all of these traces.

The second part of this thesis describes a method for measuring the intensity, phase and the complete polarization state of a laser pulse having a time-dependent polarization state (i.e. a polarization shaped pulse). This technique is called tomographic ultrafast retrieval of transverse light E-fields (TURTLE), and it is based on Second-Harmonic-Generation Frequency-Resolved Optical Gating (SHG FROG). Turtle can measure the evolution of an arbitrary, potentially very complex, ultrashort laser pulse's polarization state in time. TURTLE typically involves making three FROG measurements: one of the intensity and phase of the pulse's horizontal polarization component, one of its vertical component, and another of the 45^{o} component. Performing a simple minimization using these three FROG measurements, the time-dependent polarization state of the ultrashort pulse can be determined. We simulate TURTLE using SHG FROG for measuring very complex pulses and find that it performs very well, essentially uniquely determining even complex polarization-shaped pulses.

The third part of this thesis introduces a method for measuring two complex pulses simultaneously using a single FROG device. This technique is based on Polarization-gate (PG) FROG and it is called PG blind FROG. It involves two measurements: One of them is a PG FROG trace using the intensity of pulse 1 to gate pulse 2 and other one is the PG FROG trace using the intensity of pulse 2 to gate pulse 1. An iterative phase retrieval algorithm based on generalized projection (GP) is used to

reconstruct the intensity and phase of these two pulses. This technique has no known ambiguities and is successful for PG blind FROG, because the phase information of each pulse is contained in the PG FROG trace when this pulse is gated by the intensity of the other pulse while the phase information of the gate pulse is not present in the trace. This approach is an elegant way to measure complex and/or very spectrally broad pulses such as those due to super continuum. This is because the nonlinear crystal to be used is a standard glass such as fused silica, and these materials yield automatic phase matching.

CHAPTER 1

FREQUENCY RESOLVED OPTICAL GATING TECHNIQUES

1.1 Introduction

In recent decades, the time duration of laser pulses has become shorter and shorter due to the demands of various applications in the fields of physics, chemistry, biology and etc. Currently the duration of an ultrashort laser pulse is routinely as short as a few femtoseconds and sub-femtosecond pulses have even been generated. These pulses of light are the shortest events ever created by mankind. It is not easy to know the properties of such short events because they are very difficult to measure. This is because in general, to measure an event, a shorter event is needed. But because femtosecond pulses are often the shortest events that we have, the best that can be done is to measure the pulse with itself. Early on, techniques that used this idea were invented, such as the intensity autocorrelation[7-10]. But unfortunately the intensity autocorrelation, which attempts to measure the intensity or brightness of the pulses versus time, only gives a crude estimation of the pulse length and even this only works for the simplest pulse shapes. But there is a lot of other very important information about the pulse besides its temporal duration. For example there is also the phase which tells you the relative arrival time of the colors, and this can be a complicated higher order polynomial function. Both the intensity and phase information is important for characterization and application of an ultrashort laser pulse. Several techniques other than the autocorrelation which can fully characterize the intensity and phase vs. time or frequency were introduced in the early

1990's. These are Frequency-Resolved Optical Gating (FROG)[11-16], Spectral Phase Interferometry for Direct Electric-field Reconstruction (SPIDER)[3, 17] and spectral interferometry (SI)[18, 19].

FROG is an autocorrelation-type measurement in which the autocorrelation signal's spectrum is measured at each delay[4], instead of measuring just the intensity at each delay as done in a standard autocorrelation. As a result, more information is included in a FROG trace and it uniquely determines the intensity and phase of an ultrashort laser pulse. There are a few ambiguities in a FROG trace, but these are trivial and can be ignored or removed by taking a few additional measurements. These ambiguities include the time of direction (DOT) ambiguity which can be removed by inserting a Fabry Perot etalon into the beam [20], or the π phase ambiguity between two well separated pulses in time domain or the frequency domain[16] which can be removed by adding chip to either one pulse or both pulses to make them overlap. Other ambiguities or missing information from the FROG trace are the zero order and first order spectral phases which corresponds to the pulse arrival time in time domain which are not of interest or important for most applications.

The intensity and phase of the pulse is retrieved from the FROG trace using a two-dimensional phase retrieval algorithm which is iterative, though usually able to return a unique solution. In this thesis, the phase retrieval algorithm that we use is based on the generalized projection (GP)[21-24].

There are a variety of FROG techniques each of which involves a different nonlinearity, such as second harmonic generation (SHG) FROG[11], polarization gated (PG) FROG[25], cross-correlation (XFROG)[26], transient-gating (TG) FROG[27, 28]

and third harmonic generation (THG) FROG[25]. SHG FROG, THG FROG, and PG FROG use the pulse to measure itself so a pre-characterized reference pulse is not needed. In contrast, XFROG and TG FROG do need a reference pulse to make the measurement. Each of these variations of FROG has its advantages and disadvantages. For example, the PG geometry is automatically phase matched and easy to align, but polarizer-leakage background and other effects limit its sensitivity. SHG FROG is sensitive, but its traces are unintuitive and it has an ambiguity in the direction of time.

Recently, the FROG algorithm (GP algorithm) has been extended from only being able to characterize the intensity and/or phase of simple pulses to also being able to characterize the intensity and/or phase of complex pulses. Now, additional pulse properties such as polarization evolution can even be measured. Another technique called tomographic ultrafast retrieval of transverse light E-fields TURTLE, which is based on SHG FROG has been shown to be accurate and robust for characterizing the polarization state of an ultrashort laser pulse. In this thesis I will also demonstrate a technique called TG double blind FROG which can be used to characterize two complex pulses simultaneously and without any ambiguities. In general, the FROG technique has been widely used for measuring different types of ultrashort laser pulses and performs very well.

1.2 Second Harmonic Generation FROG

SHG FROG involves spectrally resolving a standard SHG-based autocorrelation. Its apparatus is shown in Figure 1.

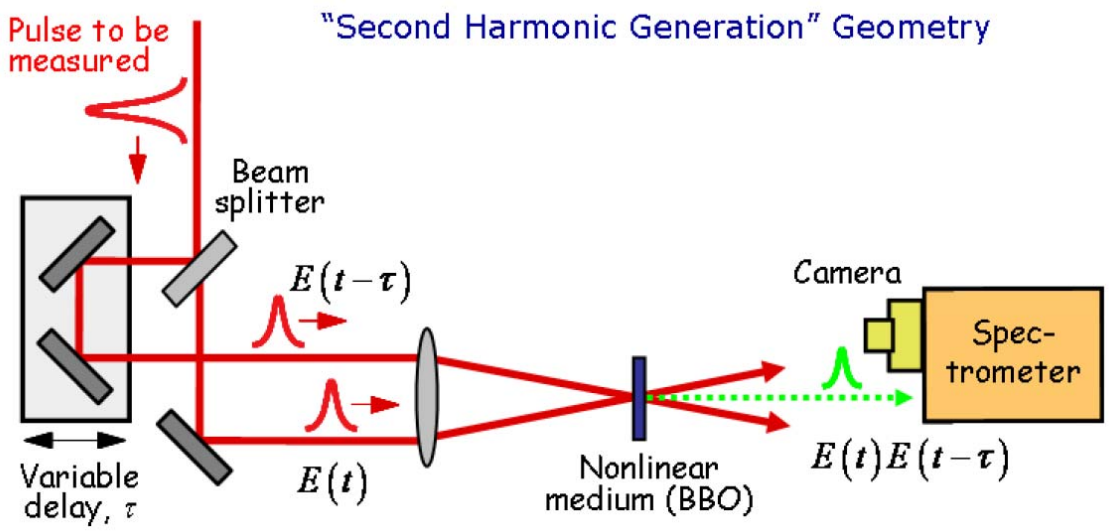

Figure 1. SHG FROG experimental setup.

The mathematical equation for an SHG FROG trace is,

$$I_{FROG}(\omega,\tau)=\left|\int_{-\infty}^{\infty}E(t)\,E(t-\tau)\exp(-i\omega t)\,dt\right|^2 \tag{1}$$

where the gate function is $E(t-\tau)$ which is a delayed version of the pulse. This equation illustrates that the SHG FROG technique measures the spectrum of the nonlinear signal at each delay instead of measuring just the intensity of the nonlinear optical signal. The result of a SHG FROG measurement is a two-dimensional image with one dimension of delay and the other dimension of frequency. Figure 2 shows the SHG FROG trace of a double-chirped pulse (shown on the left) and its corresponding SHG FROG trace (shown on the right). This pulse consists of two pulses with full width at half maximum (FWHM) values of 100fs and 50fs, respectively. The 2nd order spectral phase, which is the group

velocity dispersion (GVD) [29], was 200fs^2/rad and 150fs^2/rad, respectively for the two pulses.

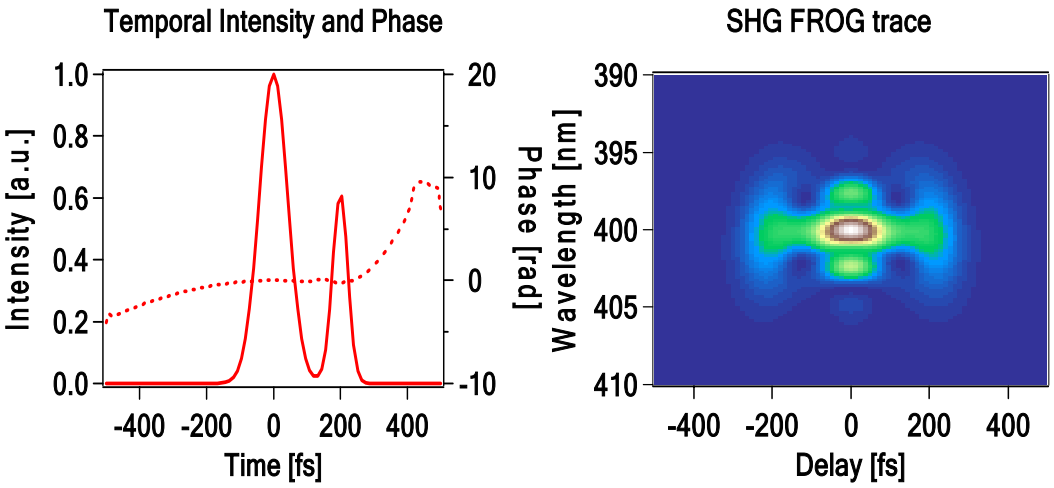

Figure 2. A double-chirped pulse and its corresponding SHG FROG trace.

One big advantage of SHG FROG compared to other versions of FROG is its high sensitivity which is due to the fact that it uses a second order nonlinear effect which yields more signal pulse energy for a given amount input pulse energy compared to FROG techniques using higher order effects. Also, it the has the best signal to noise ratio because it is easy to filter out the scattered light at other wavelength from the SHG FROG trace than other types of FROG traces. On the other hand, SHG FROG has some disadvantages due to the symmetry of its trace along the delay axis. For instance, an SHG FROG trace is the same for a field $\tilde{E}(\omega)$ and its complex conjugate, $\tilde{E}^*(\omega)$. In the time domain, this corresponds to an ambiguity in the direction of time (DOT) of the pulse [16]. For pulses that are well-separated in either optical frequency or time, an additional ambiguity arises in their relative phases $\Delta\varphi$, because in this case, both $\Delta\varphi$ and $\Delta\varphi + \pi$ yield the same SHG FROG trace [30]. But all these ambiguities can be removed by

making additional measurements. The DOT ambiguity can be removed by inserting an etalon into the beam [20], and the relative phase ambiguity can be removed by adding chip to either one of the pulses or on both of them to make these two pulses overlap. Because of its advantages and performance, the SHG FROG technique has been commercialized [31] and used for numerous applications. It can also be used to measure complex pulses[32].

1.3 Polarization-gate FROG

PG FROG[33] is another FROG technique. The PG FROG beam geometry involves splitting a laser pulse into two and then one beam is sent through crossed polarizers while the other is sent through a half-wave plate so that it has $\pm 45^{o}$ linear polarization with respect to the other pulse. Then, these resulting two pulses are sent into an instantaneously responding $\chi^{(3)}$ medium where they spatially overlap. In order to easily describe the PG FROG setup, we call the pulse to be measured the probe pulse, and the other pulse the gate pulse. In PG FROG beam geometry, the gate pulse is the intensity of the measured pulse. When the gate and the probe pulse interact in the nonlinear material, the gate pulse induces optical birefringence in the medium and this causes a slight polarization rotation of the probe pulse. This allows a small temporal slice of the probe to leak through the crossed polarizers. The transmitted probe (signal) is spectrally resolved, so that its intensity is measured as a function of frequency at each delay. A schematic for PG FROG is shown in Figure 3.

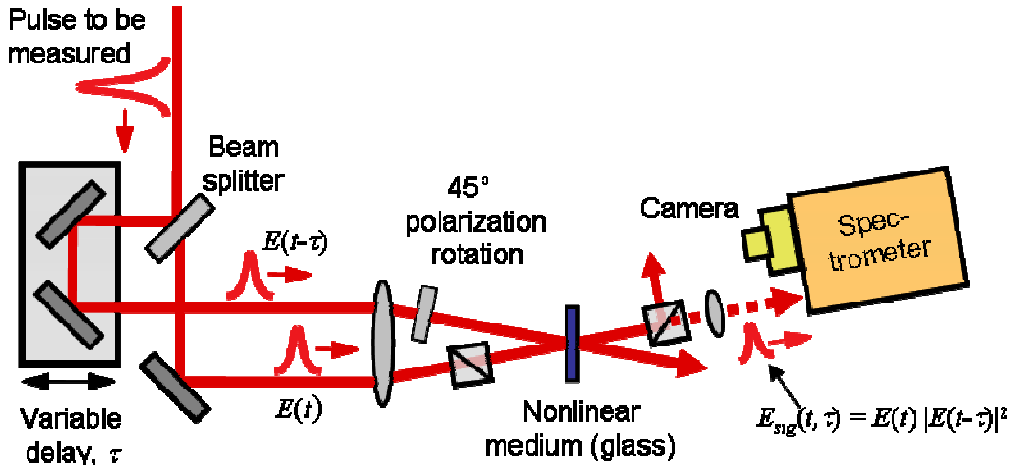

Figure 3. PG FROG experimental setup.

The mathematical equation for PG FROG is shown below

$$I_{FROG}(\omega,\tau)=\left|\int_{-\infty}^{\infty}E(t)\left|E(t-\tau)\right|^2\exp(-i\omega t)\,dt\right|^2, \qquad (2)$$

where $\left|E(t-\tau)\right|^2$ is the delayed gate function. The same double-chirped pulse used in the SHG FROG trace shown in Fig. 2 was used to generate the PG FROG trace, shown in Figure 4.

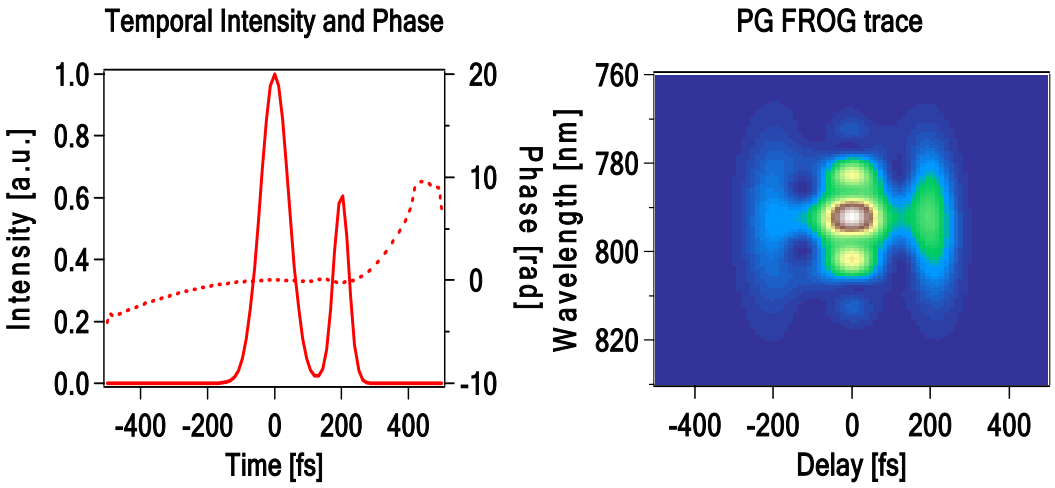

Figure 4. A chirped double pulse and its PG FROG trace

The gate function in PG FROG is the intensity of the unknown pulse because the gate pulse and the probe pulse are identical. PG FROG results in is the most intuitive FROG traces out of all of the FROG techniques, and it has many other desirable qualities. First, and most importantly, there are no ambiguities in PG FROG. Thus, PG FROG determines the complete and non-ambiguous pulse intensity and phase in all known cases. A second advantage of PG FROG is that the nonlinear-optical process is automatically phase-matched, which allows for large crossing angle leading to large delay ranges in a single short geometry. The second advantage results in two consequences: (1) alignment is easy; and (2) PG FROG is capable to measure pulses with extremely large bandwidth and/or very complex pulses. But some disadvantages exist too. For example, PG FROG requires a high-quality polarizer and these are often thick so they introduce some material dispersion and change the pulse parameters. However, this is usually not a serious problem if pulse being measured has a center frequency in the visible or near IR region.

1.4 Cross-correlation frequency resolved optical gating

XFROG[26, 34] is another variation of FROG that is based on a cross correlation. XFROG is different from SHG FROG and PG FROG, because it requires a known reference pulse as gate pulse, though there is no requirement on the spectral overlap between the probe pulse and the gate pulse. To make an XFROG measurement, both the gate pulse and the probe pulse propagate through a $\chi^{(2)}$ nonlinear medium. And, depending on the relative frequencies of the two pulses, or which is more convenient, sum frequency generation (SFG) or difference frequency generation (DFG) can be used to create this cross correlation signal. When the center wavelength of the gate pulse is same as that of the probe pulse, the nonlinear signal is an SHG signal, so this is referred to as SHG XFROG. The Schematic of the XFROG experimental setup is shown in Figure 5.

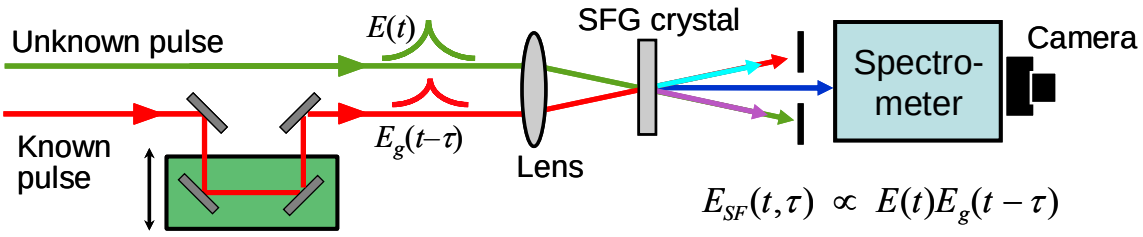

Figure 5. XFROG experimental setup

The mathematical equation describing an XFROG trace is

$$I_{FROG}(\omega,\tau)=\left|\int_{-\infty}^{\infty}E(t)E_g(t-\tau)\exp(-i\omega t)\,dt\right|^2, \tag{3}$$

where $E_g(t-\tau)$ is the delayed gate function that indicates the reference pulse. The same double-chirped pulse used to generate the traces shown in Figs 2 and 4 was used to

generate the XFROG trace shown below. The reference pulse used in this simulation is a transform limited Gaussian pulse with a temporal width (FWHM) of 50fs. This result is shown in Figure 6.

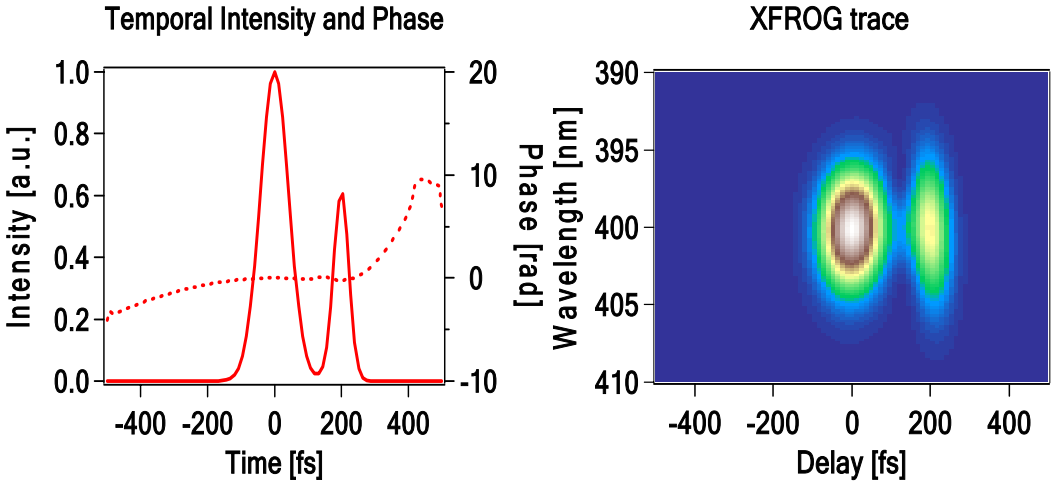

Figure 6. A double chirped pulse and its XFROG trace

XFROG is a very versatile and reliable method for measure ultrashort laser pulses and it has many desirable properties. For instance, XFROG does not require interferometric alignment accuracy. Another obvious advantage is that XFROG can characterize the weak pulse, a pulse with a center frequency in the UV, and also very complex pulses which can be defined by time bandwidth product (TBP) value. As a result DFG XFROG can be used to measure weak UV pulses. This is because the fact that XFROG does not require the spectrum of the unknown and reference pulses to overlap.

When the unknown pulse is complicated, XFROG traces can be easier to interpret than most other FROG techniques if a simple reference pulse is used. Some of the pulse information can even be read directly from the XFROG trace. For example, chirp results in a tilted trace and the sign of the chirp determines the direction of the tilt. Also, the retrieval algorithm for XFROG converges more easily than that of other FROG

techniques because of the additional known information of the reference pulse. These advantages make XFROG the ideal technique for measuring complex pulses.

1.5 The Generalized Projections FROG Algorithm

The FROG trace contains the complete information of an ultrashort pulse and can uniquely determine the intensity and phase of the pulse. But from the equation (1-3), we can see that the pulse's electric field $E(t)$ cannot be obtained directly from the corresponding FROG trace $I_{FROG}(\omega,\tau)$, so an indirect, or iterative method must be used. In order to retrieve the pulse field $E(t)$ from its FROG trace $I_{FROG}(\omega,\tau)$ a 2-D phase retrieval algorithm based on the iterative Fourier transform is often used. The flow chart describing this algorithm is shown in Figure 7 [16].

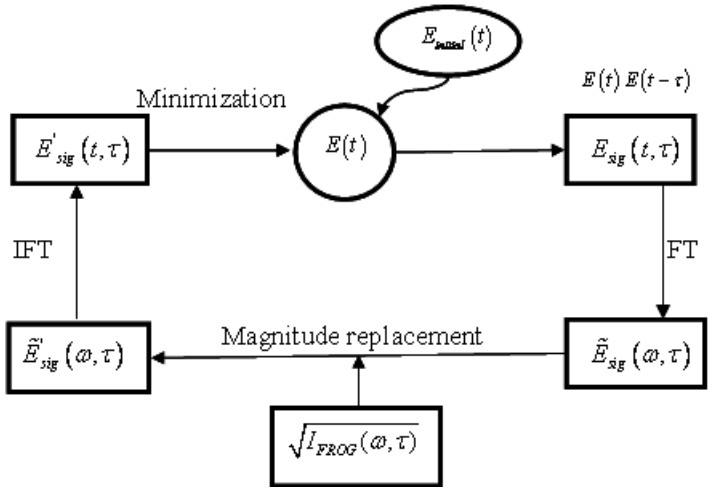

Figure 7. Description of the FROG algorithm

This method also is used commercially, for example, for retrieving field from traces measured by GRENOUILLE which is a simplified version of SHG FROG. For simplicity, the following explanation of the FROG algorithm is based on SHG FROG. I

have chosen to use SHG FROG as an example, because it is the most commonly used version of FROG.

The equation of the SHG FROG trace $I_{FROG}^{SHG}(\omega,\tau)$ was shown in equation (1). This equation illustrates the complicated relationship between the pulse field, $E(t)$, and the FROG trace, $I_{FROG}^{SHG}(\omega,\tau)$. The relationship between the unknown field and the FROG trace involves a Fourier transform and a taking the magnitude squared. This relationship determines the mathematically calculation between $E(t)$ and $I_{FROG}^{SHG}(\omega,\tau)$ irreversible. As a result, there is no direct way to invert the FROG trace to obtain $E(t)$ from $I_{FROG}^{SHG}(\omega,\tau)$. So an iterative algorithm with an initial guess has to be used to reconstruct $E(t)$.

For an iterative algorithm, the first step is to make an initial, random guess for the solution, $E(t)$. Then the corresponding signal field $E_{sig}(t,\tau)$ is generated using Eq. (4).

$$E_{sig}(t,\tau) = E(t)E(t-\tau), \tag{4}$$

The signal field is then Fourier transformed with respect to t in order to generate the signal field $\tilde{E}_{sig}(\omega,\tau)$ in the frequency domain. The measured FROG trace $I_{FROG}^{SHG}(\omega,\tau)$ is used to then used to generate an improved signal field $\tilde{E}'_{sig}(\omega,\tau)$. Since the magnitude squared of $\tilde{E}_{sig}(\omega,\tau)$ is equal to $I_{FROG}^{SHG}(\omega,\tau)$, this step involves simply replacing the magnitude of $\tilde{E}_{sig}(\omega,\tau)$ with the square root of the measured trace $I_{FROG}^{SHG}(\omega,\tau)$ to generate $\tilde{E}'_{sig}(\omega,\tau)$. The phase remains unchanged. This step is illustrated below

$$\tilde{E}'_{sig}(\omega,\tau) = \frac{\tilde{E}_{sig}(\omega,\tau)}{\left|\tilde{E}_{sig}(\omega,\tau)\right|}\sqrt{I_{FROG}(\omega,\tau)} \tag{5}$$

$\tilde{E}'_{sig}(\omega,\tau)$ is then inverse Fourier transformed back into the time domain. In the last step, the modified signal field $E'_{sig}(t,\tau)$ is used to generate a new guess for $E(t)$ using the following equation:

$$E(t) = \int E'_{sig}(t,\tau)d\tau \quad . \tag{6}$$

Each of these steps is repeated. Ideally, each iteration of the algorithm generates a better guess for $E(t)$, which eventually approaches the true electric field of the pulse. Because we are using an iterative algorithm, we usually cannot obtain the exactly the right field for the pulse. Therefore, we have to define a criterion for deciding when the retrieved pulse is close enough to the measured pulse, and this is used to decide when to terminate the algorithm.

In the FROG algorithm, the criterion for deciding when to terminate the algorithm, is the so-called FROG error which describes the difference between the experimental FROG trace and the calculated FROG trace from the guessed field at the k-th iteration. The FROG error is given by

$$G^{(k)} = \sqrt{\frac{1}{N^2}\sum_{i,j=1}^{N}\left|I_{FROG}(\omega_i,\tau_j) - I^{(k)}_{FROG}(\omega_i,\tau_j)\right|^2} \quad , \tag{7}$$

where $I^{(k)}_{FROG}(\omega_i,\tau_j)$ is the FROG trace calculated from the guessed pulse, $E^{(k)}(t)$ at the k-th iteration. Equation (7) is only used in the FROG algorithm to see if the next iteration has made the guess more accurate compared to that of the previous iteration. In case of SHG FROG $I^{(k)}_{FROG}(\omega,\tau)$ is

$$I_{FROG}^{(k)}(\omega,\tau)=\left|\int_{-\infty}^{\infty}E^{(k)}(t)E^{(k)}(t-\tau)e^{-i\omega t}dt\right|^2 \quad , \tag{8}$$

So basically, $G^{(k)}$ defines the normalized difference between the measured FROG trace and the calculated FROG trace. In practice, a constant G_0 is chosen empirically, and when $G^{(k)} \le G_0$ the algorithm will be terminated.

There are many phase retrieval algorithms available that can be used here. The Generalized Projection (GP) algorithm is the most common and robust choice for retrieving the intensity and phase from the FROG trace. The approach used in the GP algorithm is illustrated in Figure 8. From Figure 8, we can see that the final solution, or the pulse we are looking for, must satisfy two constrains. One is called the data constraint and the other is the nonlinear optical constraint. The upper ellipse represents the nonlinear optical constraint, and the lower ellipse represents the data constraint. The intersection point of these two ellipses is the final solution.

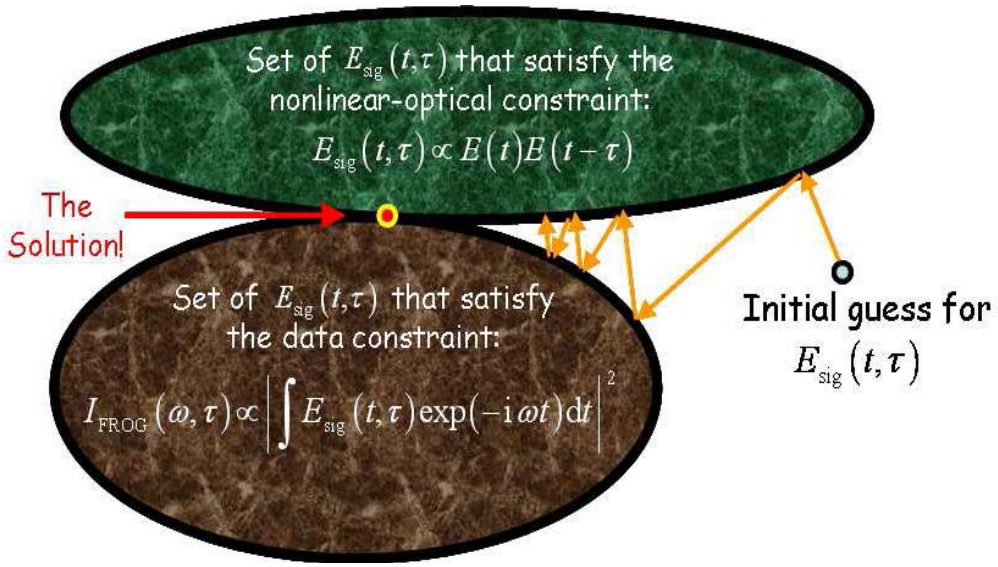

Figure 8. Generalized Projection

In practice, we start with an arbitrary point in the plane which indicates the random, initial guess. Then, this point is projected onto one of the two constraint sets to satisfy this constraint, then, this resulting point is projected onto the other constraints to satisfy the other constraint. Such projects are iteratively repeated until a final solution is reached. If these two constraints are convex, then convergence is guaranteed. But generally in FROG, the data constraint is not purely convex. Therefore, the convergence of the algorithm cannot be guaranteed. To eliminate this non-convergence caused by non-pure convex constrains, multiple trials of the initial guessed can be used. In order to satisfy the data constraint, it is necessary to replace the magnitude with the squared root of the intensity of the measured FROG trace at each iteration. In order to satisfy the nonlinear optical constraint, we must then find a new signal field $E_{sig}^{(k+1)}(t_i,\tau_j)$ that has the right nonlinear optical form, and meanwhile, it is the closest point to the current signal field $E_{sig}^{k}(t_i,\tau_j)$, since $E_{sig}^{(k+1)}(t_i,\tau_j)$ is the projection point of $E_{sig}^{k}(t_i,\tau_j)$. Therefore, the difference between these two fields must be minimized which is shown below.

$$Z=\sum_{i,j=1}^{N}\left|E_{sig}^{(k)}(t_i,\tau_j)-E_{sig}^{(k+1)}(t_i,\tau_j)\right|^2 \quad , \tag{9}$$

For SHG FROG Eq. 9 becomes:

$$Z^{SHG}=\sum_{i,j=1}^{N}\left|E_{sig}^{(k)}(t_i,\tau_j)-E^{(k+1)}(t_i)E^{(k+1)}(t_i-\tau_j)\right|^2 \quad . \tag{10}$$

In the FROG algorithm, the minimization of the Z error is treated as an unconstrained multi-dimensional optimization problem by computing derivatives of this error. The steepest decent method is used to find the direction in which the error decreases at each

iteration. The gradient of Z is calculated with respect to $E^{(k+1)}(k)(t_k = 1,2,3,...N)$ for each value of *t*. Instead of calculating the complex gradient, in practice compute the 2N parameters, $\partial Z^{SHG} \Big/ \partial \operatorname{Re}\left\{E^{(k+1)}(t_k)\right\}$ and $\partial Z^{SHG} \Big/ \partial \operatorname{Im}\left\{E^{(k+1)}(t_k)\right\}$

$$\frac{\partial Z^{SHG}}{\partial \operatorname{Re}\left\{E^{(k+1)}(t_k)\right\}} = 2\operatorname{Re}\left\{\sum_{j-1}^{N} -E_{sig}^{'}(t_k,\tau_j) * E^{(k+1)}(t_k-\tau_j) + E^{(k+1)}(t_k) * \left|E^{(k+1)}(t_k-\tau_j)\right|^2 \right. \\ \left. -E_{sig}^{'(k)}(t_k+\tau_j,\tau_j) * E^{(k+1)}(t_k+\tau_j) + E^{(k+1)}(t_k) * \left|E^{(k+1)}(t_k+\tau_j)\right|^2 \right\}, \quad (11)$$

$$\frac{\partial Z^{SHG}}{\partial \operatorname{Im}\{E^{(k+1)}(t_k)\}} = -2\operatorname{Im}\left\{-E_{sig}^{'(k)}(t_k,\tau_j) * E^{(k+1)}(t_k-\tau_j) + E^{(k+1)}(t_k) * \left|E^{(k+1)}(t_k-\tau_j)\right|^2 \right. \\ \left. -E_{sig}^{'(k)}(t_k+\tau_j,\tau_j) * E^{(k+1)}(t_k+\tau_j) + E^{(k+1)}(t_k) * \left|E^{(k+1)}(t_k+\tau_j)\right|^2 \right\}, \quad (12)$$

Because the FROG algorithm also is based on a gradient, the direction and gradient step are defined as *x* and *dE*. So the new pulse field can be written as

$$E^{(k+1)}(t_k) = E^{(k)}(t_k) + xdE^{(k)}(t_k), \quad (13)$$

where $dE^{(k)} = \frac{2\partial Z}{\partial E^{(k+1)}(t_k)}\Big|_{E^{(k+1)}(t_k)=E^{(k)}(t_k)}$. Therefore we can rewrite Z as follows:

$$Z = \sum_{i,j=1}^{N} \left| E_{sig}^{'(k)}(t_i,\tau_j) - [E^{(k)}(t_i) + x \cdot dE^{(k)}(t_i)][E^{(k)}(t_i-\tau_j) + x \cdot dE^{(k)}(t_i-\tau_j)] \right|^2. \quad (14)$$

In the minimization, Z is a polynomial function and it can also be described as

$$Z = a_0 + a_1 x + a_2 x^2 + a_3 x^3 + a_4 x^4, \quad (15)$$

where

$$a_0 = \sum_{i,j=1}^{N} \left| E_{sig}^{'(k)}(t_i, \tau_j) - E^{(k)}(t_i) E^{(k)}(t_i - \tau_j) \right|$$

$$a_1 = \sum_{i,j=1}^{N} 2\,\mathrm{Re}\{[E^{(k)}(t_i) E^{(k)}(t_i - \tau_j) - E_{sig}^{'(k)}(t_i, \tau_j)]$$
$$\times [E^{(k)}(t_i) dE^{(k)}(t_i - \tau_j) + E^{(k)}(t_i - \tau_j) dE^{(k)}(t_i)]\}$$

$$a_2 = \sum_{i,j=1}^{N} \left| E^{(k)}(t_i - \tau_j) dE^{(k)}(t_i) + E^{(k)}(t_i) dE^{(k)}(t_i - \tau_j) \right|^2 +$$
$$2\,\mathrm{Re}\{E^{(k)}(t_i) E^{(k)}(t_i - \tau_j) - E_{sig}^{'(k)}(t_i, \tau_j)] * dE^{(k)}(t_i) dE^{(k)}(t_i - \tau_j)\}$$

$$a_3 = \sum_{i,j=1}^{N} 2\,\mathrm{Re}[E^{(k)}(t_i - \tau_j) dE^{(k)}(t_i) + E^{(k)}(t_i) dE^{(k)}(t_i) dE^{(k)}(t_i - \tau_j)] * dE^{(k)}(t_i) dE^{(k)}(t_i - \tau_j)$$

$$a_4 = \sum_{i,j=1}^{N} \left| dE^{(k)}(t_i) dE^{(k)}(t_i - \tau_j) \right|^2$$

Finally, the algorithm is reduced to a one-dimensional minimization based on a polynomial function. The global minimum can be calculated directly for a polynomial function. So in the end, the GP algorithm is able to accurately find the correct pulse. And numerous experiments over more than 10 years have proven that this approach is reliable and robust.

1.6 Noise effect on the FROG trace and its suppression

In measurements, noise cannot be avoided, and a FROG measurement is of course no exception to this rule. As a result, it is very important to test the performance of the FROG algorithm in the presence of noise and make sure that it still converges. A lack of convergence is almost always an indication that the trace is contaminated by too much noise, and that the measurement needs to be retaken. In the absence of noise, determining whether or not the algorithm has converged is generally straightforward; either the error between the retrieved FROG trace and the measured trace goes to zero or not. But when

noise is present, determining when convergence has happened is no longer straightforward and everything is based on practical experience. In simulations, because we know the actual pulse, it is easy to compare the retrieved pulse with the right answer.. We have found that a FROG trace with 1% additive Poisson noise and a grid size less than 1024 x1024, the FROG algorithm converges when the FROG error is less than 1%. When discussing the FROG error the grid size must be given, because as shown in Eq. 7, the FROG error depends on this. The FROG error will be infinitely small if an infinitely large grid is used regardless of whether or not the algorithm is converging. But according to our experience with the data, when the grid size is less than 1024 x1024, the value of the FROG error is at the same order of magnitude. So, we do not need to worry about the grid size. This conclusion about the FROG error was made by inspecting the consistency between the generated pulse and the retrieved pulse for a given FROG error.

Additive noise will be used in the simulations shown here and the results will be discussed. The noise that we add simulates the scattered light or dark current that will likely be encountered in measurements. It also provides an effective nonzero Poisson distributed background. Subtracting experimental noise is very important to ensure convergence of the algorithm. The noise background is problematic because it results in some intensity at large delay which implies a nonzero intensity in the pulse wings, and also in some intensity at large frequencies which implies that high-frequency oscillations are present in the pulse. The background at both large delay and large frequency results in artificial wings in the retrieved pulse. Therefore, the region of nonzero values in the FROG trace must be an island in a sea of zeros in order to ensure that the algorithm convergences.

To obtain many zeros around the FROG trace, several noise filter methods exist. One option is to use filters for removing noise at a certain frequency without significantly affecting the pulse-intensity-and-phase information present in the trace. Corner-suppression is also helpful and this involves multiplying the trace by a function to preferentially reduce its values at the edges. Subtracting out the constant background in the FROG trace is also useful. The performance of the algorithm is significantly improved after using all of these noise suppression tricks.

CHAPTER 2

MEASURING COMPLEX ULTRASHORT LASER PULSE BY FROG TECHNIQUE

This chapter originally appeared as a paper by the author:

L.Xu, E.Zeek., and R. Trebino, Simulations of frequency-resolved optical gating for measuring very complex pulses. J. Opt. Soc. Am. B. 25: p. A70-A80,2008.

2.1 Introduction

The shaping of ultrashort laser pulses into complex intensities and phases vs. time or frequency is finding many applications, including coherent control[35], telecommunications[36], micro-machining[37], and multi-photon imaging[38]. In addition, several commercial pulse shapers[39-43] have become available and can generate pulses with time-bandwidth products (TBP's) up to ~ 100. Complex pulse shapes also occur in continuum generation[44]. Unfortunately, methods for measuring the actual shapes (intensity and phase vs. time) of such complex pulses have not received much attention.

Most techniques for measuring ultrashort laser pulses either do not yield the complete time-dependent intensity and phase (e.g., autocorrelation[9]) or can at best only measure simple pulses (e.g., SPIDER[3]). A method has recently been introduced (MIIPS[45]) that simultaneously shapes and measures pulses, but it uses the same pulse shaper to both shape and measure the pulse and so cannot be said to constitute an independent measurement of the shaped pulse, and it has not been tested on complex pulse shapes. If a well-characterized reference pulse is available, linear spectral interferometry is, in principle, capable of measuring complex pulses, but most versions

of it have artificially limited spectral resolution and so have not been able to do so. Also, spectral interferometry suffers from extreme alignment sensitivity and so is difficult to use. A simplified version of spectral interferometry (SEA TADPOLE[46]) was introduced recently, which has approximately an order of magnitude better spectral resolution than conventional versions, and it avoids the debilitating alignment sensitivity. SEA TADPOLE is capable to measure shaped pulses with TBP's of several hundred. It also can measure the complete spatio-temporal intensity and phase at and near the focus. Like all other version of spectral interferometry, however, it requires a well-characterized reference pulse whose spectrum contains the information of the shaped pulse to be measured. Fortunately, when pulse-shaping, such a pulse is generally available in the form of the *unshaped* pulse. Thus SEA TADPOLE is ideal for measuring shaped pulses, but such measurements require the use of two separate devices, one to measure the unshaped pulse and the SEA TADPOLE to measure the shaped pulse. And the reference-pulse requirement prevents spectral interferometry from measuring continuum.

Currently, the most commonly used method for measuring shaped and a complex pulse (and the simplest) is Frequency-Resolved Optical Gating (FROG[16]), which does not require a reference pulse, and so the same device can be used to measure *both* the unshaped and shaped pulses. Since its introduction in 1991, FROG and its many variations have been used to measure the full intensity and phase of a wide range of ultrashort laser pulses. FROG has measured the intensity and phase of few femtosecond pulses and pulses over many wavelength regions. Variations on it Cross-correlation FROG (XFROG) have even measured attosecond pulses[47], but, more importantly, for our purposes herein, XFROG has measured the most complex pulses—continuum—ever

measured[44]. XFROG, like spectral interferometry, requires a well-characterized reference pulse, but the XFROG reference-pulse spectrum need not contain that of the shaped pulse. The unshaped pulse is also ideal for XFROG measurements of the shaped pulse, as well. Nevertheless, the version of FROG most commonly used to measure shaped pulses is second-harmonic-generation (SHG) FROG. SHG FROG is self-referenced, using the pulse to measure itself. Like its fellow FROG techniques, it has many advantages for measuring shaped pulses, including built-in independent checks on its measurements, geometries for single-shot operation, and versatile, often very simple, arrangements. A single SHG FROG—or any self-referenced FROG—device can be used to measure both the unshaped and shaped pulses. And the various FROG iterative algorithms[47] are known for their reliability and robustness in measuring relatively simple pulses (TBP $< \sim 5$) where they have been used most of the time. However, because pulse-shaping applications can involve rather complex pulses, it is important to check the performance of various FROG techniques combining with iterative algorithms to measure complex pulses. This has never been done. Indeed, since in this case such measurements would involve the use of a complex pulse to measure a complex pulse, the performance of SHG FROG is not highly expected for such pulses and spectral interferometry or XFROG is recommended because they use a simple (unshaped) pulse to measure the complex pulse, for such measurements. But, as this advice has generally been ignored, and SHG FROG is already in common use for measuring complex pulses, this chapter is in this contribution. Indeed, it is interesting to see how well the various FROG methods measure such complex pulses.

Specifically, we test three FROG iterative algorithms. These include those of SHG FROG, polarization-gate (PG) FROG, which is also self-referenced, and XFROG. They are all based on the same generalized-projections [16] approach. To do so, we generated complex test pulses in both the time and frequency domains and then added 1% Poisson noise to all the resulting traces. We find that the XFROG algorithm converges with 100% reliability on the first initial guess, in agreement with an existing proof that (noise-free) spectrogram (XFROG) inversion should always succeed[48]. On the other hand, we find, as expected, that PG and SHG FROG are not 100% reliable in the presence of noise, but, surprisingly, are much closer to perfection than expected. PG FROG achieves 100% convergence for pulses with TBP < 30, and ~ 95% for more complex pulses (including TBP ~ 100). SHG FROG achieves > 80% effectiveness at retrieving even the most complex pulses, provided that several initial guesses are allowed if the first fails to yield convergence. Also, when the algorithm fails to converge, it nevertheless succeeds in retrieving the approximate length and general shape of the pulse, failing only in the details, which could still be adequate for many purposes. Thus, while SEA TADPOLE and XFROG remain preferable, if not ideal, for measuring shaped pulses (in our opinion), SHG FROG and, in particular, PG FROG should also provide adequate and relatively robust measurements of such complex pulses, especially if the user desires to use only one device for measurements of both the unshaped and shaped pulses or a reference pulse is not available.

2.2 FROG, the Generalized Projections Algorithm, and Simulation Details

The expression for the SHG FROG, PG FROG or XFROG trace is:

$$I_{FROG}(\omega,\tau)=\left|\int_{-\infty}^{\infty}E(t)\,E_g(t-\tau)\exp(-i\omega t)\,dt\right|^2$$

where $E(t)$ is the unknown input-pulse electric field that we are trying to measure. These simple versions of FROG are distinguished by their gate pulses: in SHG FROG, $E_g(t) = E(t)$; in PG FROG $E_g(t)=|E(t)|^2$; and in XFROG, $E_g(t)$ is an independently measured pulse. XFROG is mathematically equivalent to the well-known spectrogram, and SHG FROG and PG FROG yield "auto-spectrograms" (the pulse gates itself). Like all time-frequency-domain methods, all three FROG methods involve measurements of intensity vs. two variables, frequency (ω) and delay (τ). In other words, SHG FROG and PG FROG are spectrally resolved autocorrelations, and XFROG is a spectrally resolved cross-correlation[4].

All versions of FROG were shown to be examples of mathematical problems called *Two-Dimensional Phase-Retrieval*, and hence able to yield essentially unique solutions as long as the entire FROG trace is nearly completely contained in the data set (that is, not significantly cropped at its edges), and the trace details are properly resolved in time and frequency. The phase-retrieval algorithm usually used to retrieve the pulse from the measured trace is the generalized projections (GP) algorithm[16, 21]. It involves one-dimensionally Fourier-transforming the signal field, $E_{sig}(t,\tau) = E(t)E_g(t-\tau)$ back and forth between the t and ω domains, effectively alternately iteratively projecting onto two constraint sets (corresponding to the two equations above; see Fig. 5), eventually leading to the intersection of these two constrains—the final solution. Early versions of the FROG code were reliable, but slow; fortunately, more recent versions are much faster

due to the use of faster programming languages (e.g., C), faster code, and the realization that the generalized projections algorithm is so reliable that additional algorithms included for extra reliability were unnecessary and so have been eliminated. Commercial FROG codes now routinely achieve 20 pulse-retrievals per second and are very reliable[49].

The initial guess can affect the convergence of the GP algorithm. When retrieving very simple pulses, the GP algorithm is generally not sensitive to the particular choice of an initial guess. But, when measuring complex pulses, the initial guess could, in principle, become more important. Early on, random noise was found to be the best initial guess for the FROG algorithm for simple pulses and is generally used as the initial guess in FROG programs. Random noise and flat-phase Gaussian pulse are compared to be initial guess. The result turns out that random noise is a better choice. So in all the simulations, random noise is chosen as initial guess.

In order to test the performance of the GP algorithm in SHG FROG, PG FROG, and XFROG for measuring complex pulses, a large set of complicated pulses is generated. All these pulse are generated by starting with a sequence of random complex numbers and multiplying it by a Gaussian pulse in the time domain. The next step is Fourier transforming the resulting pulse and multiplying its frequency-domain version by a Gaussian spectrum. The widths of the Gaussians can be controlled to yield the desired complexity. This yielded a complex pulse in both intensity and phase and in both time and frequency, ideal for testing the ability of these methods to measure generally complex pulses. The steps are shown in Figure 9.

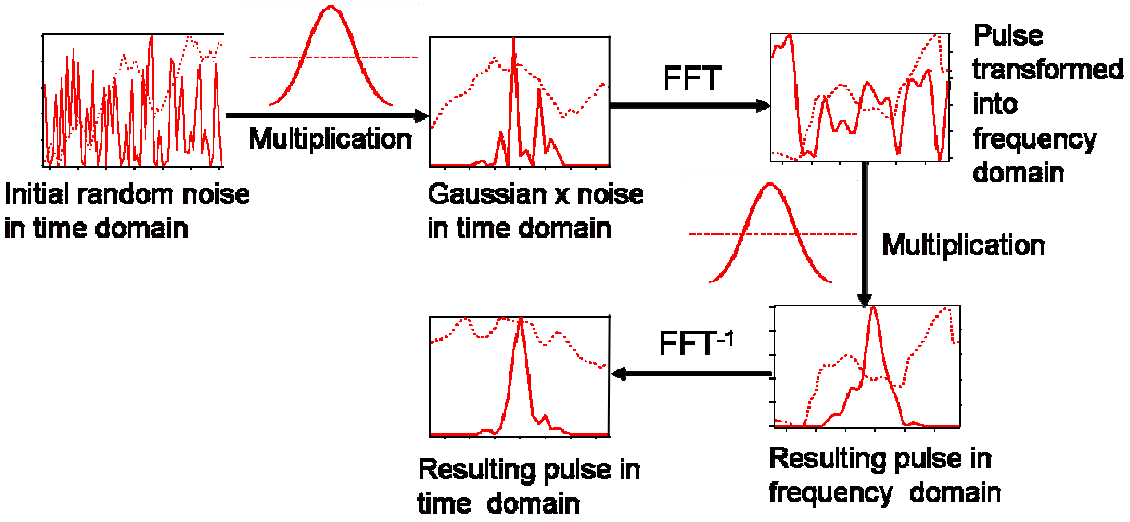

Figure 9. The process of generating a complex pulse in both time and frequency domains

While specifying the Gaussian widths yielded a good estimate of the pulse TBP, it is not exact. So, for each pulse, the precise root-mean-square (rms) TBP is computed. TBP is a common tool to measure the complexity of the pulse:

$$TBP_{rms} = t_{rms}\omega_{rms}$$

where $$t_{rms}^2 = \left\langle t - \langle t \rangle^2 \right\rangle = \left\langle t^2 \right\rangle - \langle t \rangle^2$$

and where $$\left\langle t^2 \right\rangle = \int_{-\infty}^{\infty} t^2 I(t) dt$$

and $$\omega_{rms}^2 = \int_{-\infty}^{\infty} A'(t)^2 dt + \int_{-\infty}^{\infty} A(t)^2 \phi'(t)^2 \qquad (16)$$

In the above expressions, $I(t)$ is the normalized intensity, t_{rms} is the rms temporal width, ω_{rms} is the rms spectral width. $A(t)$ is the real amplitude, and $\phi(t)$ is the temporal phase. The prime indicates the derivative[50].

The FROG traces are generated from the generated complex pulses. In order to simulate the experimental environment, 1% additive Poisson noise is added to each

FROG trace. This additive noise yields pixel-to-pixel signal variations independent of the FROG trace intensity. The reason for using Poisson noise is that it approximates the noise from practical noise sources, such as dark current and thermal noise. Such additive noise is also more challenging for the algorithm than multiplicative noise, which necessarily goes to zero in the wings of the trace. In this approach, the measured trace with the additive noise at each pixel will be[51]:

$$I_{FROG}^{(\bar{\eta})}(\omega_i, \tau_j) = I_{FROG}(\omega_i, \tau_j) + \eta_{ij}\alpha / \bar{\eta} \qquad (17)$$

where η_{ij} is a pseudorandom number drawn from a Poisson distribution of mean $\bar{\eta}$, and α is the noise fraction, which was set to 0.01 and the mean of the Poisson distribution was 5 counts.

Suppressing background noise is important in FROG measurements. Any non-zero average background (due to noise) in a FROG trace implies spurious nonzero intensity at large times and with high frequency in the pulse, that is, spurious pulse wings with high frequency noise. So, in practice, before running the pulse retrieval program, background subtraction is always performed. Several methods are available, and they include Fourier low-pass filtering, corner-suppression, and mean background subtraction. In this thesis, mean-background subtraction is enough to reduce the noise and make the algorithm converge. For the particular examples in this chapter, the mean of the noise was obtained by averaging the values in the 5x5 pixel squares in the four corners of the FROG trace (i.e., far from the center of the trace, where the most important pulse information is located). After subtracting this constant background from all points in the trace, the resulting negative points are set to aero (as is usually done).

Figure 10 gives an example of a moderately complex pulse with a TBP of 4.7 and its SHG FROG trace (with noise) and the resulting retrieved pulse. The retrieved intensity and phase of the pulse and the generated one agree well with each other. A measure of the success of a pulse retrieval is the FROG error (the rms difference between the input and retrieved traces), which is 0.00341 for this 256×256 grid, which is very good. Other measures of the retrieval success are available when performing simulations and they are the mean rms intensity and phase errors between the generated pulse and the retrieved pulse . For this pulse, we found them to be 0.007 and 0.0209, respectively. The excellent pulse retrieval in this case is not surprising because the SHG FROG GP algorithm is known to work very well when measuring such moderately complex pulses.

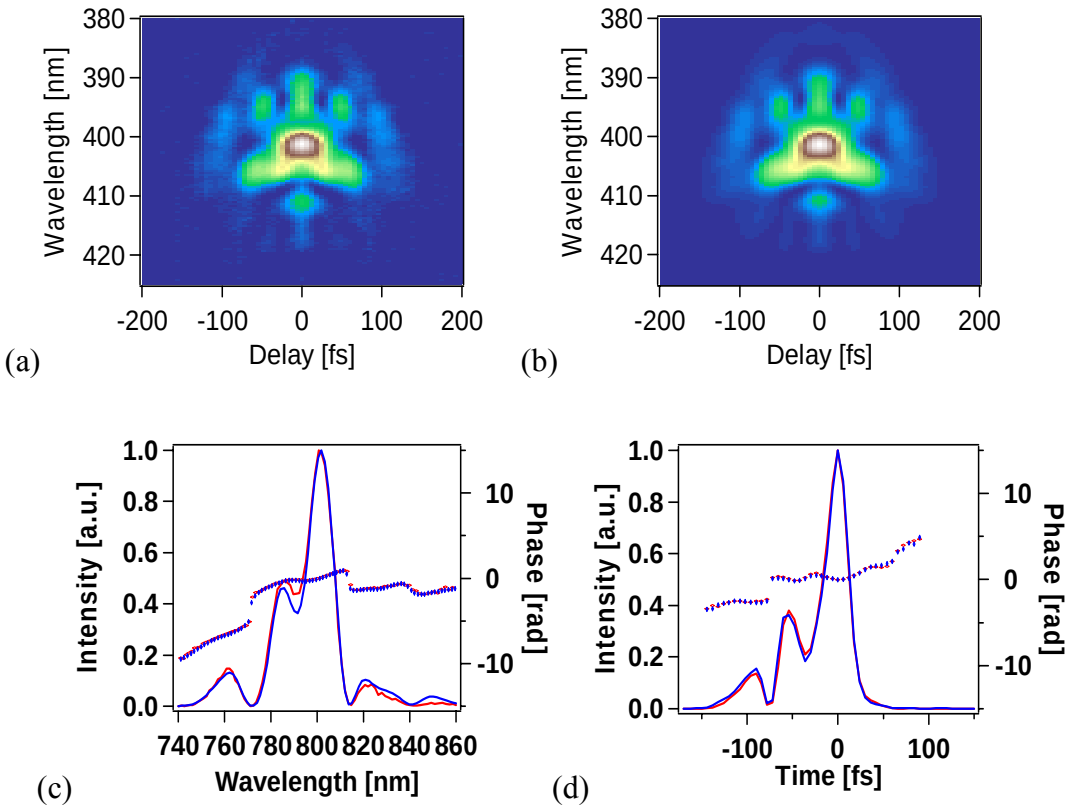

Figure 10. Moderately complex pulse with TBP = 4.7

(a) original SHG FROG trace with noise, (b) retrieved trace, (c) generated and retrieved spectral intensity and phase, (d) generated and retrieved temporal intensity and phase. In c and d (and in all

subsequent analogous figures), the generated pulse is indicated by lines, and the retrieved pulse by dots. Good convergence has occurred here. The FROG trace is well contained in the image window. For better display, the shown FROG traces were cut from the generated one, which had a wavelength range from 327.675 nm to 514.385 nm and a delay range from -768 fs to 762 fs. The maximum value of three rows and columns along the perimeter of the image window is 0.88% of the peak value after background subtraction, so the trace was only slightly cropped.

A considerably more complex pulse, with a TBP of 40.6, and its corresponding SHG FROG trace are shown in Figure.11. The retrieved intensity and phase of the pulse agree very well with the generated curves. The FROG error is 0.0052 for this 512×512 grid. The mean rms intensity and phase errors are 0.0274 and 0.0219, respectively.

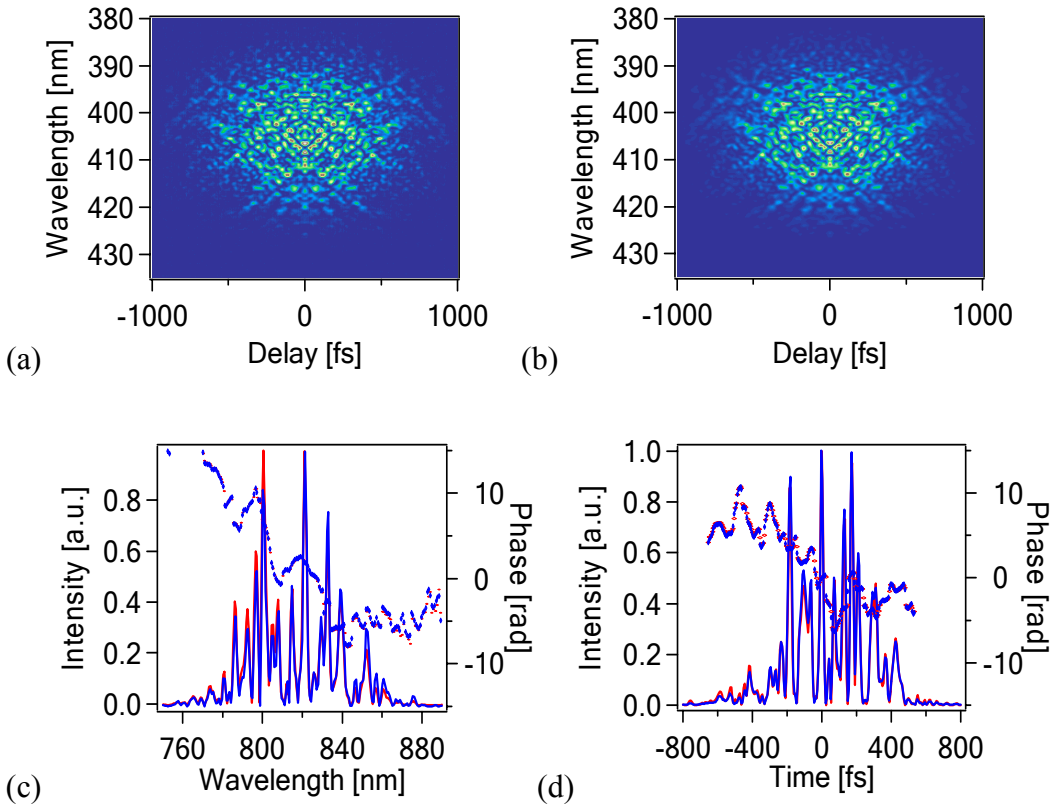

Figure 11. Very complex pulse with TBP = 40.6.

(a) original SHG FROG trace with noise, (b) retrieved trace, (c) generated and retrieved spectral intensity and phase, (d) generated and retrieved temporal intensity and phase. Good convergence has occurred here. The generated trace (here and in later figures also) appears somewhat darker due to the additive noise applied to it (and whose mean has been subtracted prior to running the

algorithm); this subtraction and the algorithm combine to remove most of the added noise. Indeed, note the identical structure in both pulses and traces. For better display, the shown FROG trace is cut from the generated one with wavelength range from 326.503 nm to 512.02 nm and the delay range from -1536 fs to 1530 fs. The FROG trace is well contained in the image window. The maximal value of the three rows and columns along the perimeter of the image window is 1.25% of the peak value after background subtraction.

An extremely complex pulse, with a TBP of 94.3, and its corresponding traces are shown in Figure 12. The retrieved pulse agrees very well with the generated pulse here as well. The FROG error is 0.4% for the 1024×1024 grid. The mean rms intensity and phase errors are 0.0337 and 0.0452, respectively.

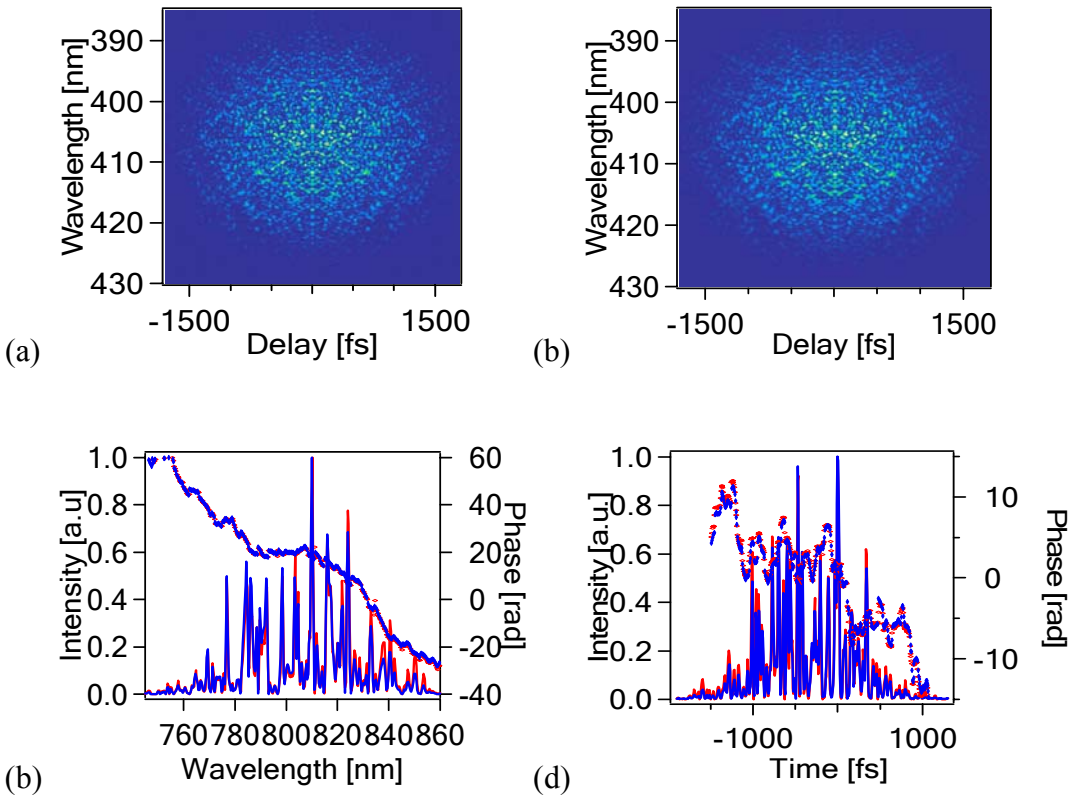

Figure 12. Extremely complex pulse with TBP = 94.3

(a) original SHG FROG trace, (b) retrieved FROG trace (with noise), (c) generated and retrieved spectral intensity and phase, (d) generated and retrieved temporal intensity and phase. Good convergence has occurred here. The FROG trace is well contained in the image window. For better display, the shown FROG trace is cut from the generated one with wavelength range from 327.348 nm to 514.385 nm and the

delay range from -3072 fs to 3066 fs. The maximal value of three rows and columns along the perimeter of the image window is 1.11% of the peak value after background subtraction.

Because the mathematical constraints in SHG and PG FROG are not purely convex, convergence of the GP algorithm is not necessarily guaranteed. The algorithm is not converging for all traces.

In practice, convergence of the GP algorithm is generally indicated by the FROG error. In this work, as in previous work, for FROG data (with grid size less tham 1024X1024) with about 1% additive noise, convergence is achieved when the FROG error is less than about 1%. When the FROG error is greater than 1%, the GP algorithm can be seen to have generated a pulse that is visibly different from the generated pulse. See Figure 13, which shows an example for which convergence has not been achieved (TBP_{rms} of 38.9). The SHG FROG error for this case is 1.6 % for this 512×512 grid size.

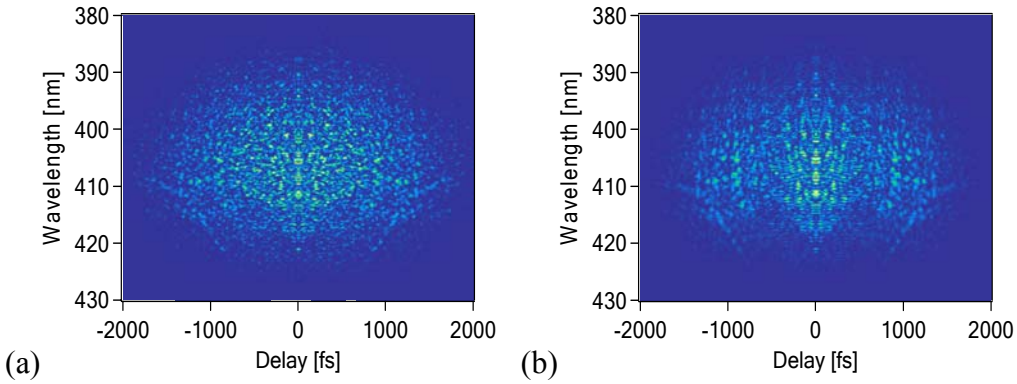

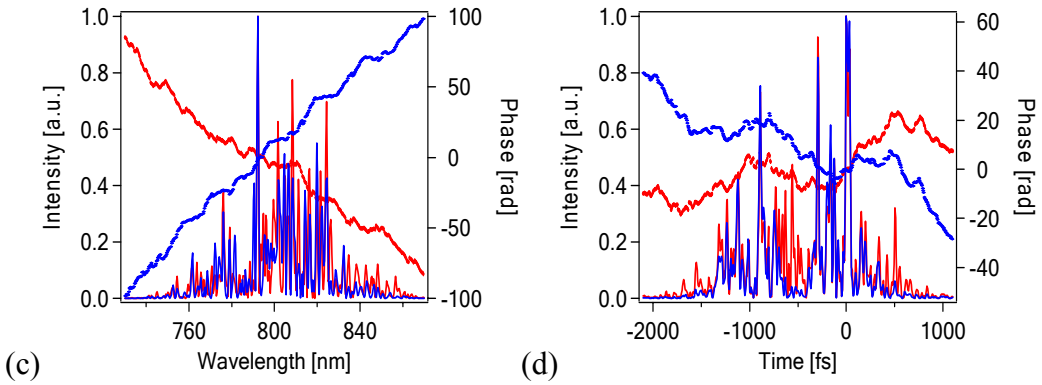

Figure 13. A pulse for which convergence has not been achieved

(a) generated SHG FROG trace with noise, (b) retrieved trace, (c) generated and retrieved spectral intensity and phase, (d) generated and retrieved temporal intensity and phase. Note the discrepancies between the generated and retrieved pulses. For better display, the shown FROG trace is cut from the generated one with wavelength range from 327.464 nm to 514.385 nm and the delay range from -1530 fs to 1536 fs. The FROG trace is not as well contained in the image window as in the previous examples, perhaps the reason for the poor convergence. The maximal value of the three rows and columns along the perimeter of the image window is 1.51% of the peak value after background subtraction.

In Figure 14, the distribution of the SHG FROG error for 30 pulses with TBP values from 30 to 40 is shown. For all converging cases, the FROG error is much less than 0.5%, and for the non-converging cases, the FROG error is greater than 1.5%. This confirmed the converging and the non-converging cases by can be visual inspected.

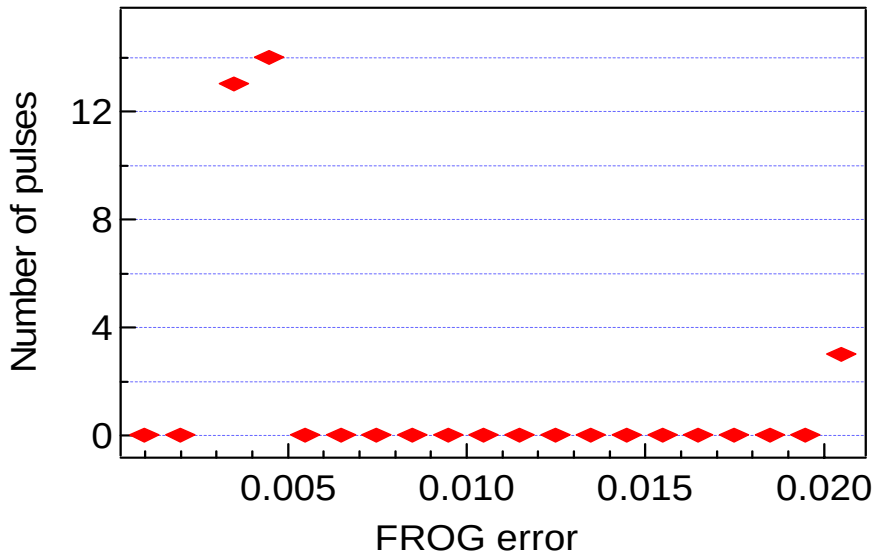

Figure 14. Histogram of FROG errors for 30 pulses with TBP value from 30 to 40, showing a clear delineation between converging (FROG error < 1%) and non-converging (FROG error > 1%) cases.

As a result, in this analysis, the convergence to have failed for a given initial guess if a FROG error of < 1% has not been achieved, and the convergence to have failed in general if a FROG error of less than 1% has not been achieved after ten runs of the algorithm using ten different randomly generated initial guesses. We should point out that, at first glance, it would seem that use of the rms intensity and phase errors would be more rigorous and hence more appropriate. However, use of these definitions is actually significantly complicated by several factors. First, one would need to take into account SHG FROG's ambiguity in the direction of time and the need to curve-fit each intensity and phase curve to the precise center of time, peak intensity, and absolute phase—quantities not measured by FROG (or any other method for measuring ultrashort pulse shapes). Also, phase-unwrapping issues as well as the meaninglessness of the phase when the intensity approaches zero (and the associated arbitrariness in the definition of the phase error) further complicate the problem. As a result, the FROG error is a far

better approach for automating this analysis, which involves more than 1000 pulses. However, we also visually inspected a large fraction of the retrieved intensities and phases to verify convergence and also to confirm the absence of ambiguities (possible very different pulses with the same traces) beyond the trivial ones mentioned above.

Using this approach, we studied the general performance of the various FROG GP algorithms for measuring complex pulses with TBP's up to 100. We generated 350 pulses for each statistical analysis. The TBP's of these pulses ranged from 1 to 100. For the purposes of displaying our results, we binned sets of 35 pulses evenly into intervals of TBP ranging from 1 to 10, 11 to 20, etc.

2.3 Testing the SHG FROG GP algorithm

The results of our analysis for SHG FROG are shown in Figure 15. We find that, in general, the more complex the pulse, more initial guesses on average are needed for convergence. In other words, the SHG FROG algorithm is more sensitive to the initial guess for more complex pulses.

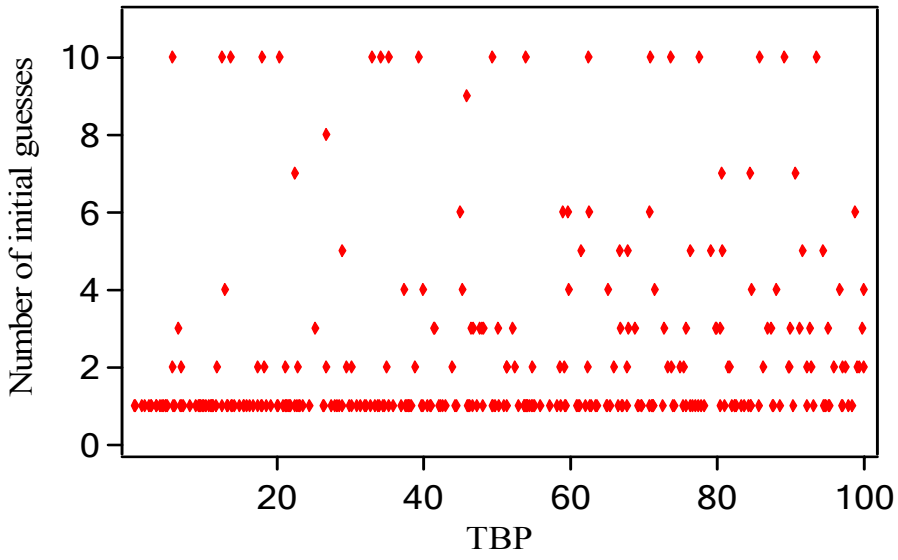

Figure 15. Number of initial guesses required for correct pulse retrieval in SHG FROG vs. TBP for the pulses in our analysis. Note that most pulses can be retrieved in SHG FROG using only a few initial guesses, but some (shown as requiring ten pulses) cannot.

Figure 16 shows the percentage convergence for pulses as a function of the pulse rms TBP. Of course, with more initial guesses, the percentage of convergence increases. In general, we find that SHG FROG works remarkably well for such complex pulses, given the complexity of the problem. When five initial guesses are allowed, more than 80% of the pulses, and occasionally 90%, can be retrieved, even for extremely complicated pulses with TBP of ~ 100. In most cases, even when convergence is not achieved after five initial guesses, convergence is achieved after a few more tries. Only 5% of the pulses failed to achieve convergence after ten initial guesses.

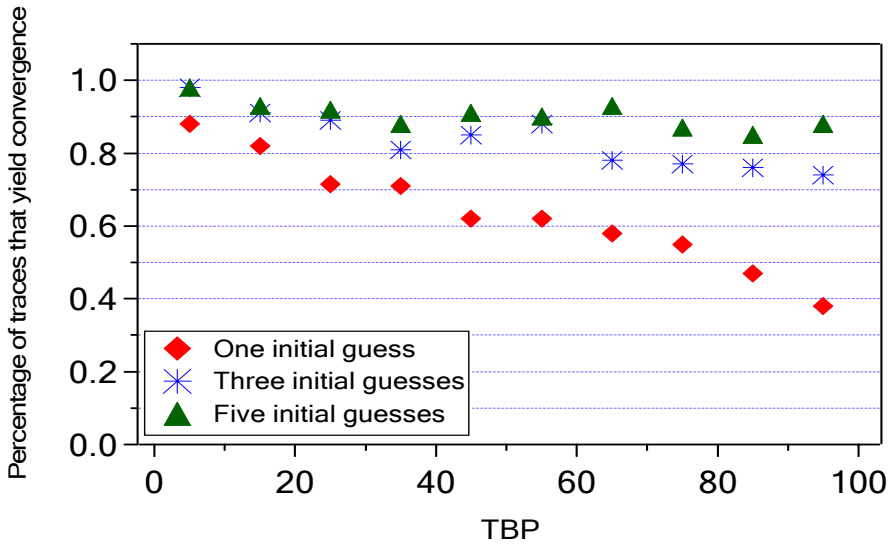

Figure 16. Statistical analysis of the performance of the GP algorithm in SHG FROG. In most cases, when convergence is not achieved after one initial guess, convergence is achieved after a few more tries, but not always.

2.4 Testing the PG FROG GP algorithm

We performed an analogous simulation for PG FROG. A typical example is shown in Figure 17. The TBP of the generated pulse is 15.5. The retrieved intensity and phase vs. time and wavelength agree with the generated ones. The FROG error is 0.0034 for this 512×512 grid. The mean rms intensity and phase errors are 0.0236 and 0.0293, respectively.

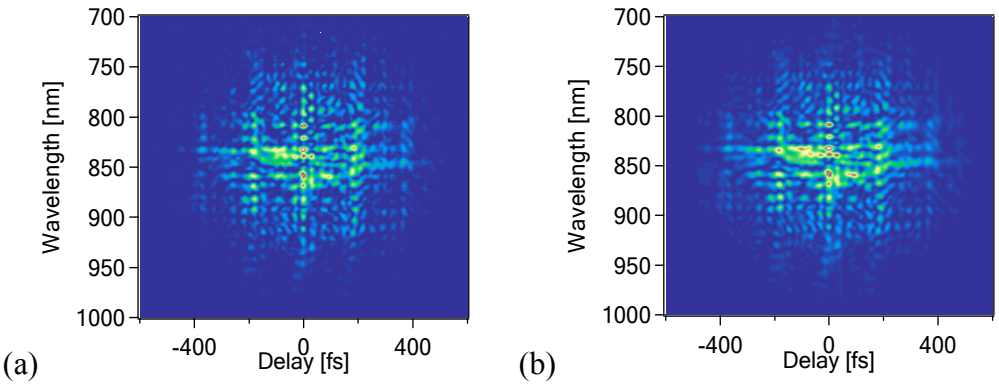

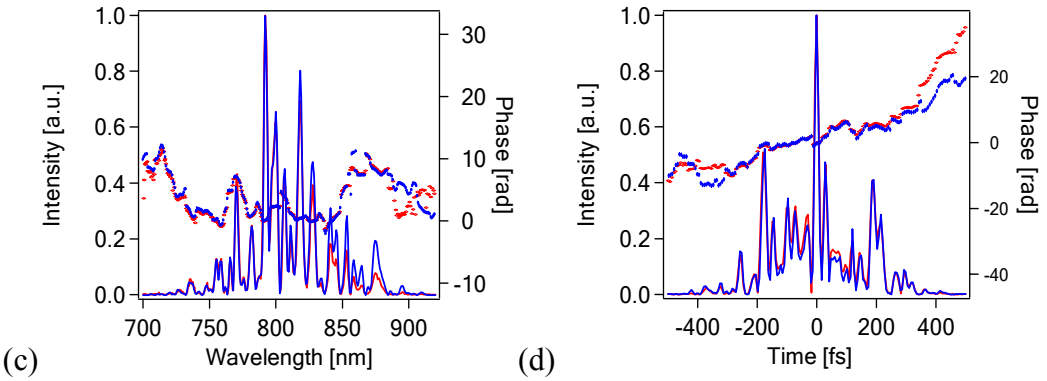

Figure 17. Example of PG FROG for measuring a complex pulse (here a pulse with TBP = 15.5) (a) generated FROG trace with noise, (b) retrieved trace, (c) generated and retrieved spectral intensity and phase, (d) generated and retrieved temporal intensity and phase. For better display, the shown FROG trace is cut from the generated one with wavelength range from 327.464 nm to 514.385 nm and the delay range from -1536 fs to 1530 fs. The PG FROG trace is well contained in the image window. The maximal value of three columns along the perimeter of the image window is 0.89% of the peak value after background subtraction.

We generated 300 new random pulses with TBP's from 1 to 100 to test the general performance of the PG FROG GP algorithm. Thirty pulses were generated for each TBP interval. The results are shown in Figsure 18 and 19. We found that the PG FROG GP algorithm works extremely well for retrieving complex pulses with TBP's less than 40. Even for extremely complex pulses, the PG FROG GP algorithm converged most of the time. Only one initial guess was needed to obtain the correct pulse in most cases. Only three non-converging cases occurred, and it is interesting that no traces yielded convergence for four to nine initial guesses, implying that the non-convergent traces were pathological in some way. Indeed, we believe that, by chance, these PG FROG traces were not well contained in the array. We plan to rerun this analysis later, checking for such cropping and eliminating such cropped traces from the analysis (or enlarging the array before running the algorithm).

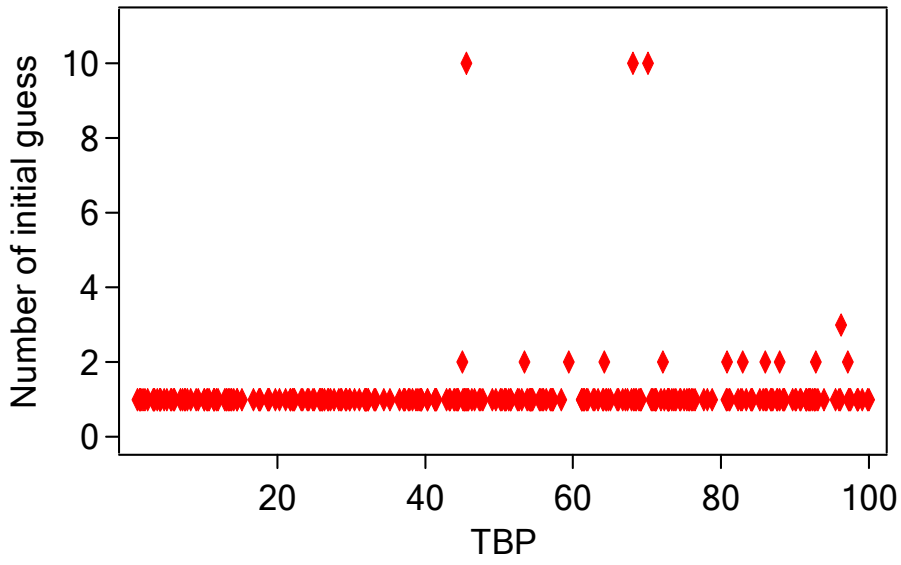

Figure 18. Number of initial guesses required for correct pulse retrieval in PG FROG vs. TBP. Note that most pulses can be retrieved using only one initial guess, and nearly all can be retrieved after two or three.

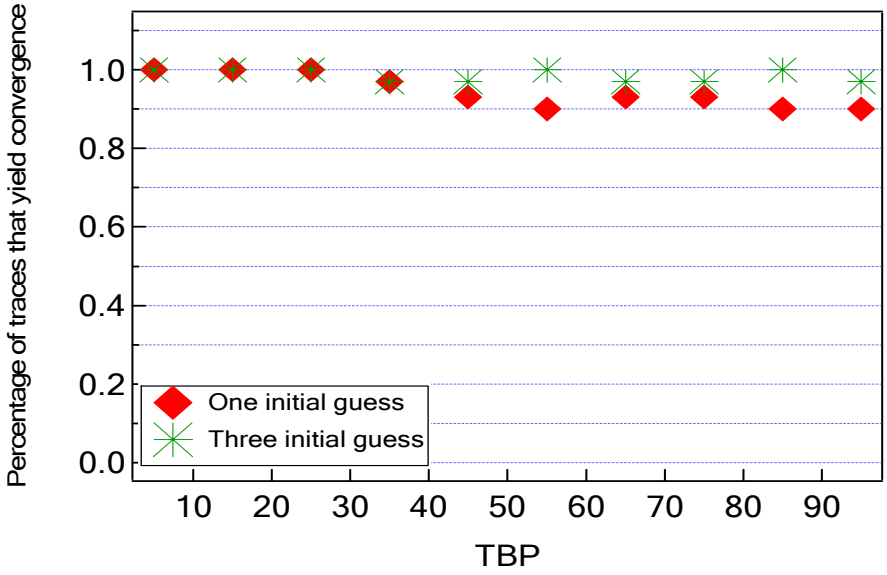

Figure 19. Statistical analysis of the performance of the GP algorithm in PG FROG.

2.5 Testing the XFROG GP algorithm

We performed an analogous simulation of complex pulse measurement using XFROG. We used a reference pulse that was a simple Gaussian pulse with FWHM of 50 fs and zero phase. Although a great deal has been written about choosing optimal pulses for generating spectrograms, we made no effort to optimize this pulse for optimal results. A typical example pulse and trace are shown in Figure 20. The TBP value of this generated pulse is 66. The retrieved phase and intensity vs. time and vs. wavelength agree with the generated ones. Note that this trace is simpler than SHG and PG FROG traces for similarly complex pulses due to the simplicity of the gate pulse in XFROG. The FROG error is 0.003 for this 512×512 grid. The mean rms intensity and phase errors are 0.0411 and 0.0314, respectively.

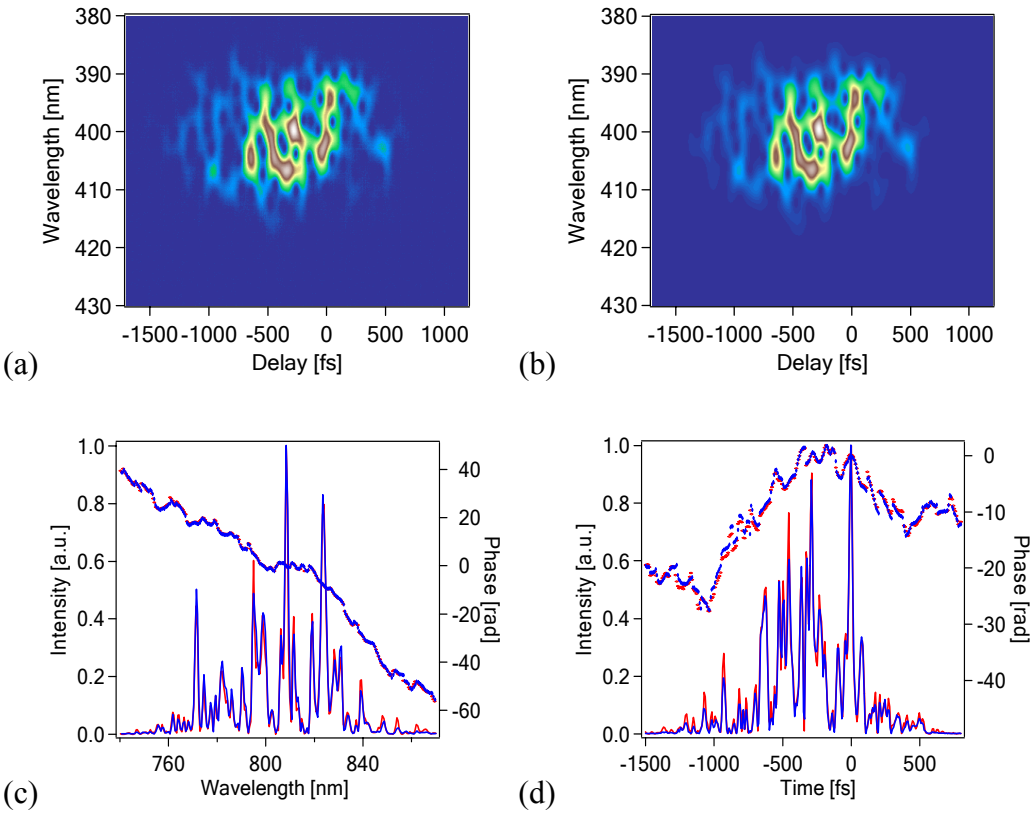

Figure 20. Example of XFROG for measuring complex pulses (here a pulse with TBP = 66)

(a) generated FROG trace with noise, (b) retrieved trace, (c) generated and retrieved spectral intensity and phase, (d) generated and retrieved temporal intensity and phase. For better display, the shown FROG trace is cut from the generated one with wavelength range from 343.02 nm to 480.065 nm and the delay range from -2048 fs to 2040 fs. The XFROG trace is well contained in the image window. The maximal value of three columns along the perimeter of the image window is 1.013% of the peak value.

We also generated 350 new pulses with TBP's from 1 to 100 to test the general performance of the XFROG GP algorithm. As before, 35 pulses were generated for each TBP interval from 1 to 10, 11 to 20, etc. The results are shown in Figure 21. We found that the XFROG GP algorithm works extremely well for retrieving even the most complex pulses in the presence of noise, *converging for every pulse on the first try*. Only one initial guess was needed to obtain the correct pulse for every case; and the FROG error was always less than 0.01. Our results verify that the spectrogram always yields the correct pulse, and that the GP algorithm is an excellent algorithm to do so.

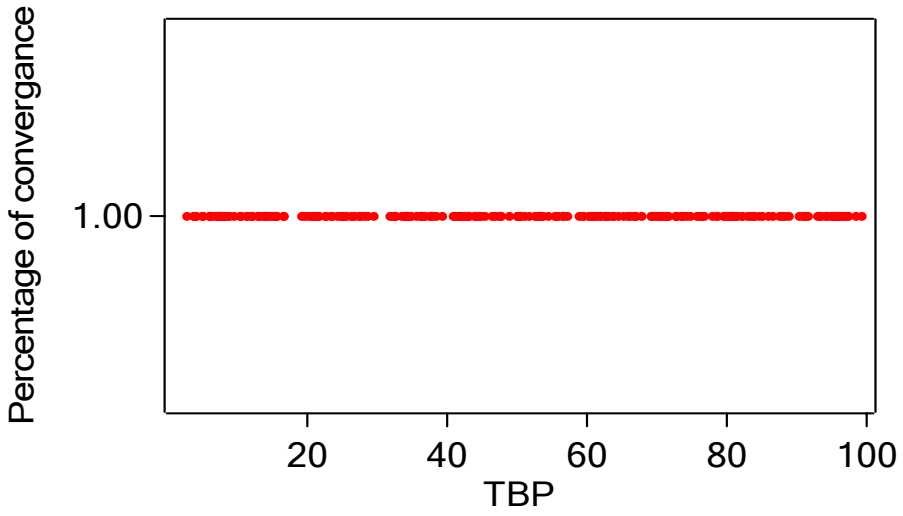

Figure 21. Statistical analysis of the performance of the XFROG GP algorithm. Convergence is always achieved after only one initial guess, even for extremely complicated pulses.

2.6 Discussion and Additional Observations

The three FROG algorithms we considered in this study performed quite well. XFROG performed perfectly, PG FROG performed very well. And SHG FROG performed reasonably well. The performance order scales with the complexities of the gate pulses in these techniques. XFROG generally uses a very simple gate pulse and ours was particularly simple; PG FROG uses the intensity of the unknown pulse, and SHG FROG uses the unknown pulse intensity and phase. The simpler the gate pulse, the better the performance.

The question that naturally arises is why the SHG and PG FROG algorithms converge so reliably for most extremely complex pulses but not for some considerably less complex pulses. In the course of working with the various FROG techniques over time, we have noted that one way to yield poor convergence is to crop the trace in time or frequency. And we have noticed that, in this study, the traces that failed to yield

convergence were those with the largest nonzero values along their perimeters. The simple solution in this case would simply be to scan further in delay and frequency. In a future study, we plan to further investigate this issue, and we believe that we will achieve even better convergence then. Also, it would be interesting to see if the use of additional noise-filtering techniques and additional algorithmic techniques, such as those used in previous versions of the FROG algorithm but abandoned when the GP approach proved to work so well, would help.

Another question that our study addressed is the issue of the possibility that other, previously unknown, ambiguities exist in these techniques. It is well known that SHG FROG possesses a (trivial) ambiguity in the direction of time (which is easily removed by a second measurement with additional glass in the beam), and most pulse measurement techniques, including FROG, do not measure the absolute phase and the pulse arrival time and also have (trivial) ambiguities in the relative phases of well-separated pulses and modes (although a properly designed XFROG measurement lacks these). But our study of complex pulses allowed us to search for additional previously unknown ambiguities (trivial or otherwise) that could in principle occur for complex pulses. And in view of the fact that we added noise to the traces, it was also possible that we could find "approximate ambiguities," that is, additional pulses whose traces are not identical to that of the correct pulse, but, due to the presence of noise, are within the experimental error of the trace of the correct pulse and yet are quite different from the correct pulse. However, in the ~ 1000 randomly generated complex pulses studied in this effort, we found no pulse whose retrieved trace was equal to or very similar to its original trace, but whose retrieved intensity and phase differed significantly from the original pulse. Thus, we

found no new exact—or approximate—ambiguities in SHG FROG, PG FROG, or XFROG. This confirms that these techniques should work well for the measurement of simple and complex pulses.

It should also be mentioned that, while the FROG algorithm is very fast for relatively simple pulses (typically using 64 x 64 traces and requiring a fraction of a second), it is much slower for complex pulses, such as those of this study, scaling as N^2 ln N, where N x N is the size of the array.

Another issue is the accuracy with which FROG can measure zeros and weak regions of the pulse. Logarithmic plots of one of our SHG FROG simulations, Fig 4 (c) and Fig 4 (d), are shown in Fig 15. Only the intensity is shown. The generated and retrieved pulses agree very well in the lower intensity regions, with some slight discrepancies, usually well below 1%. In view of our addition of 1% noise to the trace, this represents very good performance. Thus, FROG could be expected to measure relatively weak regions of the pulse with good accuracy.

Finally, we should point out that, when the FROG algorithm does not converge, this fact is made clearly evident by the relatively large FROG error, so one always knows when an additional initial guess is required.

2.7 Conclusions

We have simulated the performance of the Generalized Projections algorithm for retrieving very complex pulses (with TBP up to 100) from SHG FROG, PG FROG, and XFROG traces in the presence of additive noise.

For SHG FROG, we find that, even if the pulse is extremely complicated, the intensity and phase of the pulse can usually be retrieved. But more than one initial guess is often needed for such complicated pulses in the presence of noise.

The PG FROG algorithm performance is considerably better. It always converged for simple and moderately complex pulse with TBP up to 30. Overall, it could retrieve 99% of the pulses we tried, and when the TBP value is greater than 30, approximately 95% of the complex pulses could be retrieved using only one initial guess.

XFROG worked perfectly, retrieving all complex pulses on the first initial guess, even in the presence of noise.

We conclude that, if a suitable reference pulse is available, and the user is willing to build two separate devices, the XFROG and SEA TADPOLE techniques remain the best choices for measuring complex pulses, but, if not, PG FROG is an excellent choice, and SHG FROG is a reasonable choice also.

CHAPTER 3

IMPROVING THE CONVERGENCE OF THE FROG ALGORITHM FOR COMPLEX PULSES

3.1 Causes of non-convergence in SHG FROG and PG FROG

Frequency-Resolved Optical Gating (FROG) allows us to measure both simple and complex pulses [16]. Recently we reported that the SHG FROG and PG FROG GP algorithms sometimes exhibit non-convergence in the presence of noise, and especially as the complexity of the pulses increases [32]. On the other hand, we found that the XFROG algorithm always converged which is not surprising considering that it involves using a known characterized reference pulse unlike PG FROG and SHG FROG. Also, the reference pulse is usually a simple, transform limited pulse which makes XFROG traces for a given pulse considerably simpler than other FROG traces and therefore it is much easier to retrieve the pulse from these traces. This makes XFROG this best choice for measuring complex pulses, and we have found that the XFROG GP algorithm always converges on the correct answer and with only one random, initial guess [32].

Usually, the SHG FROG and PG FROG GP algorithms both need multiple initial guesses to obtain a correct solution for an extremely complex pulse. And even then, the correct solution, or convergence of the algorithm cannot be guaranteed. If ten initial, ten random guesses are tried, and the correct pulse still cannot be found, we define the algorithm as non-convergent.

Here we attempt to determine the causes of non-convergence in the SHG FROG and PG FROG algorithms in order to find a solution to this problem. Immediately there

are some simple and obvious problems that introduce errors such as the unit conversion that must be done on an experimental FROG trace before it can be retrieved. In the lab, the FROG trace is sampled on a constant wavelength interval because spectrometers linearly map wavelength, rather than frequency onto position. But the FROG algorithm uses Fourier transforms to go back and forth between time and frequency, so the FROG traces' vertical axis must be converted from λ to ω before the algorithm can be used. Also, the points on the frequency axis must have an equal spacing to use the standard Fast Fourier Transform algorithm. To simulate experiments, the FROG trace is generated in the frequency and delay domains but then converted to wavelength using the conversion shown below (18)

$$I_{\omega}(\omega) = \frac{\lambda^2}{2\pi c} I_{\lambda}(\lambda)\big|_{\lambda=2\pi c/\omega} . \tag{18}$$

Before the FROG trace is retrieved, it must be converted back to the frequency and delay domains. To do this, cubic spline interpolation is used to make sure that the points on the vertical axis are equally spaced in ω and not λ [52]. These two steps distort the trace a little, even though in principle the two unit conversions should cancel each other. But this unit conversion is not really essential, and should not noticeablely affect the trace, so to test the algorithm without its influence, we just leave out these two steps.

So to avoid these errors, we took 30 non-converging cases of SHG FROG simulated traces and treated these in the frequency and delay domains leaving out the unit conversion steps. Other causes of the non-convergence are likely the noise added or the perhaps the algorithm itself is not capable of retrieving these pulses? To determine which of these the case is, we tried retrieving these FROG traces both with and without noise. We found that 40% of the non-converging cases due to the additive noise. And we also

found that the other 60% of these were due to insufficient sampling, meaning that either more points were needed on the grid to capture all of the small features, or the FROG trace was truncated at the edge because a bigger grid was needed. This truncation usually can be noticed due to the colormap chosen. We found that all of these non-converging cases in SHG FROG could be made to converge by solving these two problems which we did using some simple techniques for noise reduction and to increase the sampling rate. Since adding these simple, preliminary steps to the FROG algorithm, we have not been able to find any non-converging PG FROG traces and we have done over 150 trials.

3.2 Methods for noise filtering

In practice, noise is present in all measurements. In our simulations we add Poisson noise to simulate real experimental traces which we choose because it is a close approximation to thermal noise which is always present in digital cameras (such as the one used to measure a FROG trace). So, our goal is to find a method for effectively reducing this type of noise. Many techniques, Such as Fourier filtering [53], Wiener filtering [54], Gaussian filtering [55], corner suppression and deconvolution [56], are useful for suppressing noise in digitally acquired images. Here we chose to use low-pass Fourier filtering and corner suppression because the other filtering techniques require knowledge of the experimental instrument response function which would be nice to avoid if possible. Our goal is to reduce the high frequency noise and to make sure that the values at the edge of the image window have intensity much lower than the peak value of the FROG trace.

First, constant background subtraction was employed for each simulated FROG trace and then additional, non-constant noise reduction was performed. Corner

suppression reduces the values at the edge and guarantees that the signal intensity around the perimeter of the trace is zero (as it should be). High values at the edge are due to noise and these make the algorithm stagnate and return the wrong answer for large delays or frequencies. Low-pass Fourier filtering removes the high frequency noise without significantly affecting the trace information and it smoothes out the FROG trace. Depending on the specific FROG traces, we either use on or both of these methods to reduce the noise.

3.2.1 Super-Gaussian corner suppression

Corner suppression involves multiplying the FROG trace by a function to reduce the values at the edges of the trace where it should be equal to 0. To perform the corner suppression, we multiplied the FROG traces by a radially symmetric super-Gaussian function which is given by

$$\Gamma(\omega_i, \tau_j) = e^{-[(\omega_i - \omega_0)^2 + (\tau_j - \tau_0)^2]^2 / d^4}, \quad (19)$$

where d is the full-width at half maximum of the super-Gaussian. The reason that we choose a Super-Gaussian over other functions is because it has a flat top shape, which prevents it from changing the shape of the center of the FROG trace which mostly contains the actual information about the pulse information. This method is suitable for traces that are fully contained in the image window, but high noise values around the perimeter where they should be equally to 0, which is often the case for measured traces. If this is the case, multiplying the trace by a supper-Gaussian function will cause us to lose any real information. Figure 22 shows a simulation of the SHG FROG trace for an extremely complex pulse with a TBP of 82.4. When we retrieved this simulated trace without adding noise, the algorithm converged on the correct answer and with a low

FROG error of 5.74e-6. But when we added 1% Poisson added, the pulse could not be retrieved. Therefore, it is obvious that the non-convergence is caused by the added noise. To solve this problem we used corner suppression, and with the appropriate super-Gaussian, we were able to get the algorithm to converge.

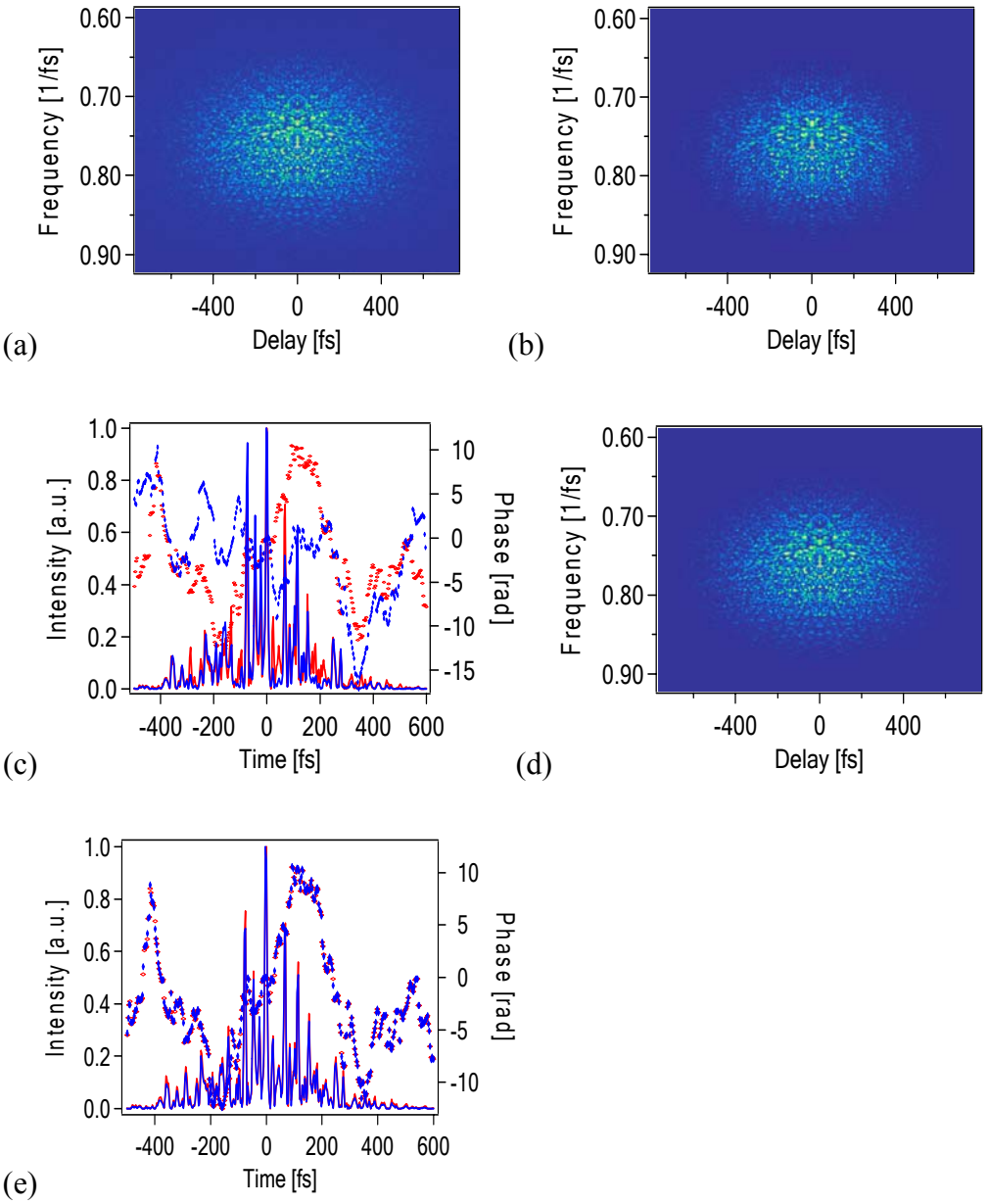

Figure 22. Corner suppression using a super-Gaussian improves the algorithm's convergence: (a) Generated trace with 1% niose, (b) retrieved trace, (c) generated pulse and retrieved pulse in time domain, (d) trace after the corner suppression, and (e) generated pulse and

retrieved pulse from (d). After retrieval, the FROG error obtained for (b) is 0.0253 for a 512 x 512 grid size and the FROG error for (d) is 0.00398 which is less than that required by the convergence criteria described in this paper [32]

3.2.2 Low-pass Fourier filtering

Another noise suppression method that we found to be helpful is Fourier filtering which is commonly used in image processing [53, 57, 58]. In the FROG technique, low-pass Fourier filtering is used when the FROG trace is surrounded by high frequency noise. It is especially useful when the FROG trace almost fills the image window because in this case corner suppression cannot be used without changing the real information in the trace.

To do this we take a 2-D Fourier transform of the FROG trace going from $I(\omega,\tau)$ to $I(t,\Omega)$. In the Fourier domain, $I(t,\Omega)$ is multiplied by a super-Gaussian function, (see Eq (19)) to eliminate the data in the high frequencies which is purely noise. Then this resulting image is inverse Fourier transformed back the ω-τ domain resulting in an image with much less high frequency noise. The width of the super-Gaussian determines the lowest frequency that is not filtered or left in the image. If the width of this window is very narrow, then this filter not only filters out the noise, but also filters out some of the data, so this has to be avoided. We check to avoid this by visually inspecting the image before and after the Fourier filtering. And example of this process is shown in Figure 23. The FROG error for the trace before adding any noise was 5.11e-6. And after we added the noise, the FROG error is 0.0264 and non-convergent. This means the non-convergence is caused by noise. To filter the noise, we chose $d = 1$ for the super-Gaussian

filtering function. After applying the low-pass Fourier filter, we retrieved correct pulse intensity and phase achieving a FROG error of 0.0079.

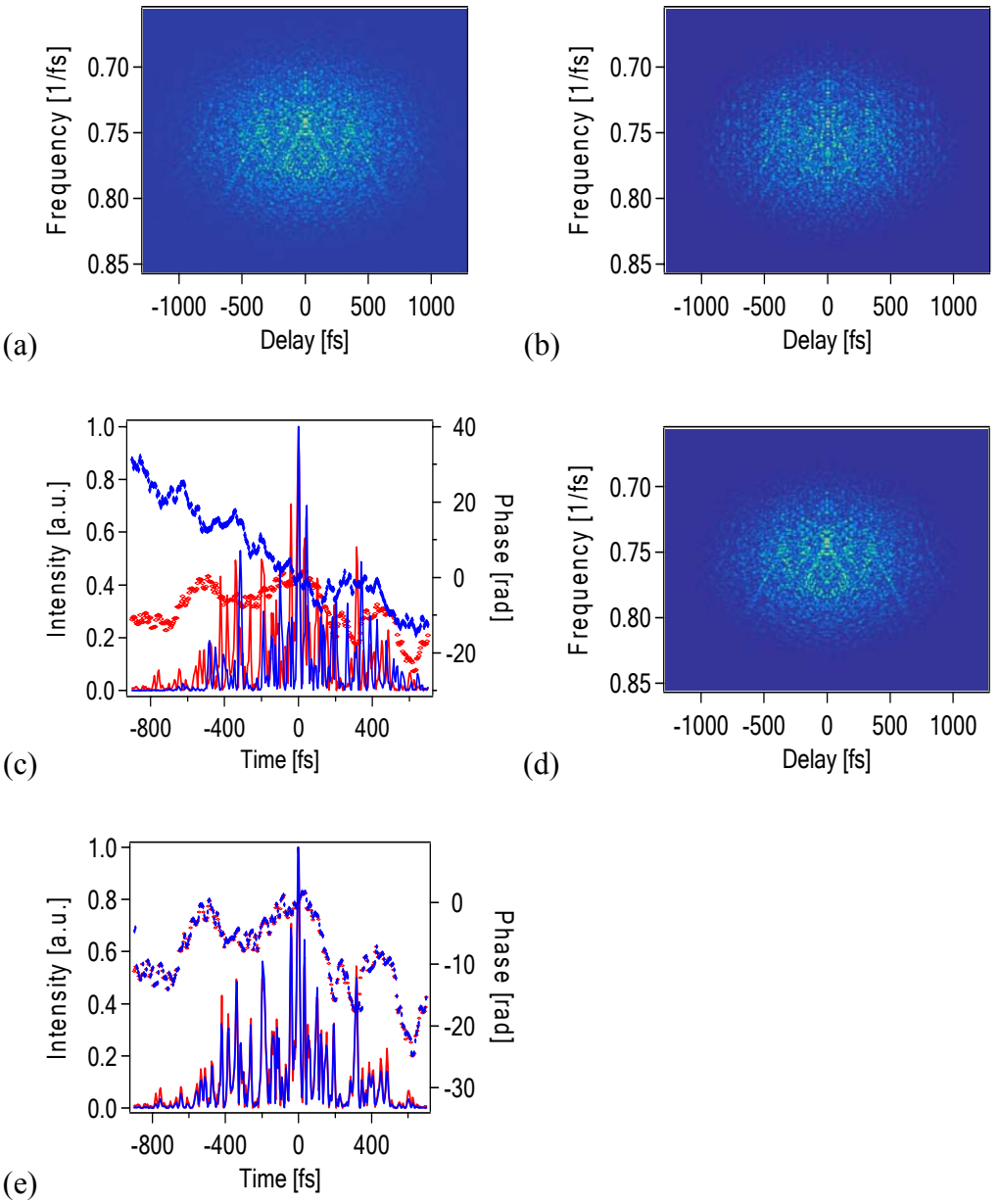

Figure 23. Low-pass Fourier filtering improves the FROG algorithm's convergence: (a) The generated trace, (b) the retrieved trace, (c) the generated pulse and retrieved pulse in the time domain, (d) the trace after the corner suppression, (e) and the generated pulse and retrieved pulse from (d). After retrieval, the FROG error obtained for (b) is 0.0264 for a 512 x 512 grid size, and the FROG error for (d) is 0.0079 which is less than the converging criteria stated in paper [32].

3.3 Increasing the sampling rate and range of the FROG trace

Having a proper sampling rate and range is important for a FROG measurement in order to achieve convergence in the FROG algorithm. We obtained this conclusion from our simulation result in which 60% of the non-converging cases were due to a poor sampling rate or range. A correct sampling range guarantees that the FROG trace is an island in a sea of zeros or that no cropping of the part of the trace that contains information about the pulse has occurred. Without any noise the FROG sampling range (FSR) criterion is that the intensity of the data points at the perimeter of the FROG trace must be 10^{-4} or less relative to the peak intensity of the trace [59]. The Nyquist sampling theorem [60], must also be obeyed to ensure that the FROG trace sampling rate is sufficient to capture the small features. This says that the highest frequency occurring in the signal is equal to the inverse of twice of the time range. Out of these two sampling requirements, the sampling range requirement is more stringent, and therefore simply ensuring that the FROG trace is surrounded by many zeros will also satisfy the Nyquist theorem [16]. This is because a pulse sampled at Nyquist rate will have FROG trace data that are truncated at significantly higher values. So, we choose the FSR sampling range as our sampling criterion. If the sampling rage is poor, we are able to improve it by increasing the FROG trace grid size from $N \times N$ to $2N \times 2N$ or larger. This will include all the FROG data points in the image window. The trade off is that the bigger grid size slows down the algorithm.

We increased the number of grid points when generating the pulse thus increasing both the range and resolution of the FROG trace's grid. Because our algorithm is based on a Fourier transform, we have to obey the relationship between the frequency interval

and delay interval $\Delta\omega = 1/(N\Delta\tau)$ [61], where $\Delta\omega$ is the frequency sampling interval and $\Delta\tau$ is the delay sampling interval and satisfying this relationship guarantees that we will satisfy the Nyquist sampling theorem. Therefore, increasing the sampling rate along one dimension of the trace helps to satisfy the FRS sampling range criterion along the other dimension.

Figure 24 illustrates what we did to achieve convergence by changing the FROG trace's grid. The time bandwidth product (TBP) of the pulse that we used for this test was 79. In the original non-convergent FROG trace, intensity of the trace in the three columns along the perimeter was 0.0059, which is much higher than 10^{-4} (the maximum of the trace is 1), and it does not satisfy the FSR sampling range described above. The FROG error achieved using this trace was 2.28e-2. Next, we increased the grid size to try and solve this problem. To decide whether to add resolution to the frequency or the time axis we visually inspect to the trace to which axis needs more range added to it (though we could improve the resolution in both dimensions if we needed to) [59]. In this example, we increased the sampling rate in the frequency dimension because visually we could see that more range was needed on the delay axis. These results are shown in Figure 24 (a). The resulting maximum value in the three columns along the perimeter are now 0.002, which does not meet the FSR criterion. The FROG algorithm converged and had a retrieval error of 8.59e-6, which is a big improvement. After we added 1% Poisson noise to the enlarged FROG trace, it still converged and with an error of 3.69e-3. This illustrates the importance of having a sufficiently big grid when measuring complex pulses with FROG and using this trick should allow researchers to measure more complex pulses that they are already measuring with SHG FROG.

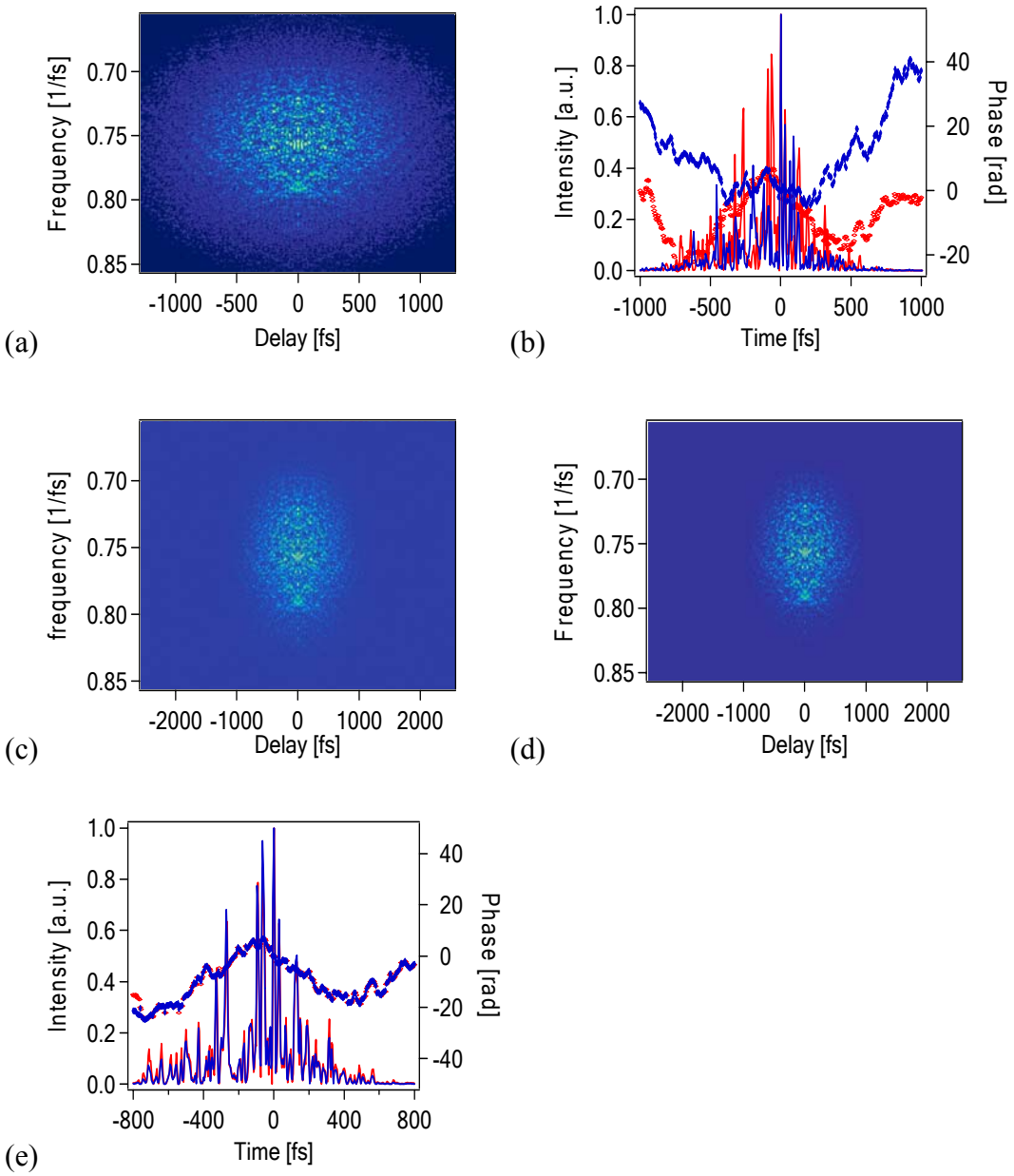

Figure 24. Increasing the sampling range improves the algorithm converging

(a) generated trace, (b) retrieved trace, (c) generated pulse and retrieved pulse in time domain, (d) trace after the increasing the sampling rate in frequency domain, (e) generated pulse and retrieved pulse from (d). After retrieval, the FROG error obtained for (b) is 0.028 for a 512 x 512 grid size, and the FROG error for (d) is 0.00369 for a 1024 x 1024 grid size.

3.4 Conclusions

In general, the non-convergence of the SHG FROG and PG FROG algorithms are caused noise around the perimeter of the FROG trace and an insufficient sampling rate or range. The non-convergence caused by noise can be prevented by using different noise suppression methods, and that due to an insufficient sampling grid can be removed either by improving the sampling rate or choosing an a large enough sampling range. Using these simple tricks, the overall convergence of both the SHG FROG and PG FROG GP algorithms can be as great as 100%. This proves that SHG FROG and PG FROG can be suitable for measuring even complex pulses as long as noise suppression and an appropriate sampling rate and range are used.

CHAPTER 4

ABIGUITY ISSUE IN PULSE MEASUREMENT

This chapter appears on the paper by the author:

Lina Xu, Daniel J. Kane, and Rick Trebino, "Comment on "Amplitude ambiguities in second-harmonic generation frequency-resolved optical gating" by B. Yellampalle, K.Y. Kim, and A. J. Taylor", accept for publication by Optics Letters

The most important characteristic of any measurement technique is the avoidance of ambiguities. Unfortunately, all general ultrashort-pulse measurement techniques have ambiguities, such as the absolute phase and pulse arrival time which is corresponding to the first order spectral phase, DOT and π phase ambiguity. Fortunately, all known ambiguities in the FROG technique are *trivial*, that is, unimportant, or easily removed. In the above paper, however, the authors (YKT) point out a potentially very serious *nontrivial* ambiguity in SHG FROG[62]: two relatively simple pulses with slightly different intensity substructure that yield similar SHG FROG traces that they claim cannot be distinguished in practice—a very serious ambiguity, if true.

To show how similar the traces are for the two pulses, YKT computed the rms difference between the FROG traces of the two pulses, usually called the "FROG error," which would be very small for an ambiguity. Indeed, YKT quoted a very small value of 7×10^{-6}, easily indicative of an ambiguity.

Unfortunately, YKT did not report the definition of the error they used. The appropriate definition of the FROG error for such comparisons is the "energy-normalized" error, which normalizes the error by the nonzero area of the trace [16, 51, 63]:

$$G' \equiv \left[\frac{1}{N^2} \sum_{i=1}^{N} \sum_{j=1}^{N} \left[(I_1^{FROG})_{ij} - (I_2^{FROG})_{ij} \right]^2 \right]^{1/2} \Bigg/ \left[\frac{1}{N^2} \sum_{i=1}^{N} \sum_{j=1}^{N} \left[(I_1^{FROG})_{ij} \right]^2 \right]^{1/2} \tag{20}$$

where $N \times N$ is the array size. This error definition is used to compare traces for different pulses and to estimate convergence. It compares the traces only where they are nonzero and deliberately omits the infinite sea of zeros that necessarily surrounds all traces. Using this definition of the error, we obtain a FROG error of 2.6% for the "ambiguous" pulses of YKT. This is a large difference, and one easily distinguished in practice, where multiplicative noise of about 1% is common.

Simple visual inspection of YKT's own plot of the difference between the two traces (YKT Fig. 3e) confirms this value. The average difference between the traces over the nonzero area of the traces is about 1%, but, because these differences occur on the sides of the trace, the maximum errors correspond to relative errors larger than 2%, and we expect to obtain slightly more than a 2% G' error (which is what we compute).

It is possible that YKT used a more common, alternative FROG error definition (Eq.(7)) that omits the denominator (and called G) and which is generally used mainly to compare iterations in the FROG algorithm, where it is only necessary to decide whether the error has decreased or not, and omitting the denominator saves computation time. The well-known problem with this definition is that it yields FROG errors that are highly array-size dependent[59]. This is because the discrete-Fourier-transform constrains the

FROG trace axes' ranges and increments and forces large-array traces of simple pulses to necessarily include very large delays and very large frequency offsets, relegating the nonzero region of the trace to a tiny island in a vast ocean of zeros, as has been discussed many times. Thus, the use of this (incorrect) FROG-error definition with a very large trace necessarily averages over numerous zeros, guaranteeing a very small FROG error between essentially all pairs of traces, even wildly different traces corresponding to wildly different pulses. This is, of course, a well-known issue for any average: no average should artificially include a large number of meaningless zeros. To understand the magnitude of this effect, use of a 512×512 or 1024×1024 array for the traces of these simple pulses (where 32×32 or 64×64 is realistic) would yield a trace with approximately 99.9% of the trace points essentially equal to zero, artificially reducing the resulting FROG error by a factor of ~1000. However, a reasonable (and the most common) FROG trace size of 64 x 64 yields a G error of 0.2%—still much larger than the value reported by YKT and which is easily distinguishable in practice (as we show below).

We can also easily visually confirm the value of G from Fig. 3e in YKT's paper. The average difference is about 1% over the nonzero area of the trace and zero in the background. The nonzero region of the trace covers about 1/5 of the array, so the value of G should be about 0.2%, and this is what we compute—not 7×10^{-6} as YKT report. Unfortunately, YKT did not report their trace size N. Even if YKT had used G, rather than G', and an unrealistically large array size of 4096×4096, they have still reported an incorrect value, one that is far too small.

Table 1. FROG errors, *G* and *G'*, for different grid sizes. 64 x 64 is reasonable for the pulse in YKT Fig. 3.

Grid size	*G*	*G'*
64×64	0.0021	0.026
128×128	0.0015	0.026
256×256	0.001	0.026
512×512	7.28E-04	0.026
1024×1024	5.15E-04	0.026
2048×2048	3.61E-04	0.026
4096×4096	2.55E-04	0.026

More importantly, simply obtaining two traces and quoting *any* difference between them is an insufficient approach to determining ambiguities in modern pulse-measurement techniques. That approach is, of course, all that can be done in autocorrelation-based methods because such methods lack pulse-retrieval algorithms. FROG, on the other hand, benefits from a powerful algorithm that retrieves the pulse intensity and phase from its measured trace. Thus the relevant question is *not* how the measured traces look to the eye, or even their difference, but instead whether the pulses *retrieved* from them would be confused in a measurement.

To answer this question, we generated SHG FROG traces of the two "ambiguous" pulses and added up to 2% additive noise to simulate a poorly performed, noisy experiment. Also, additive noise yields noise throughout the trace, whereas multiplicative noise, which is actually the type of noise present in SHG FROG, mainly yields noise only in the intense regions of the trace. We then performed the usual average-background

subtraction and ran the usual Generalized Projections SHG FROG algorithm to retrieve the pulses from their respective traces. Finally, as is usually done, we used random noise as the initial guess for the pulses. The SHG FROG algorithm easily retrieved the correct pulses on the first try from their respective traces in all cases.

Also, to attempt to fool the algorithm into falling into this alleged ambiguity, we used the *other pulse* as the initial guess in each case. Despite this deception, the algorithm achieved excellent convergence to the correct pulse in all cases, even in the presence of 2% additive noise. Clearly, such pulses would not fool the FROG algorithm in practice and so cannot be considered ambiguities in any sense of the word.

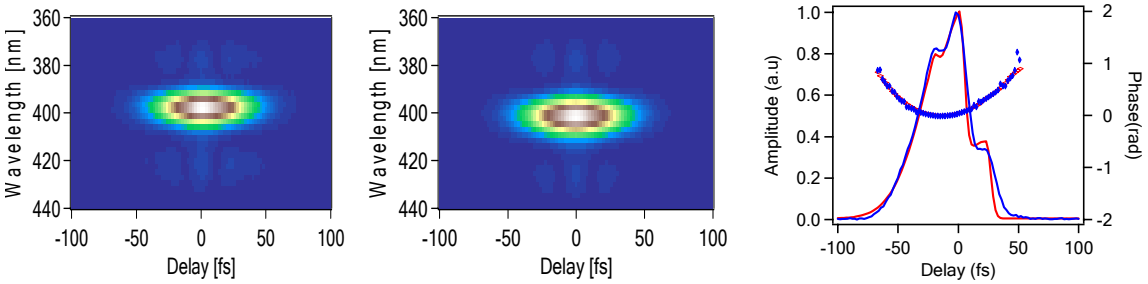

Figure 25 From left: SHG FROG trace of YKT's pulse #1 with 1% noise added, retrieved SHG FROG trace, and the generated and retrieved pulses in the time domain.The red curve indicates the generated pulse and the blue curve indicates the retrieved pulse. The initial guess for the algorithm was the "ambiguous" pulse. The array size was 128 x 128, the FROG *G* error of the retrieval is 0.0036, and the *G'* error is 0.0824.

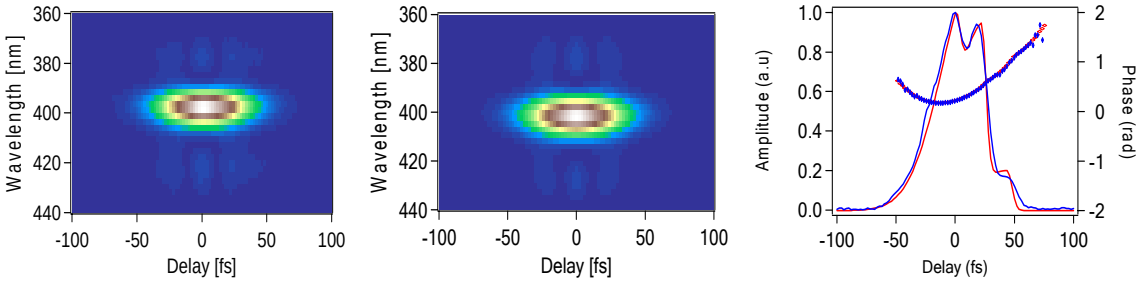

Figure 26. From left: SHG FROG trace of pulse #2 with 1% noise added, retrieved SHG FROG trace and the generated and retrieved pulse in the time domain.The initial guess for

the algorithm was the "ambiguous" pulse. The FROG *G* error of the retrieval is 0.004, and the *G'* error is 0.0803.

In their paper, YKT also reminded us of an ambiguity present in SHG FROG, which, as YKT point out, was described earlier on two occasions, first by one of the authors herself[64, 65] and then later by one of us[20]. It involves double pulses well-separated in time (see YKT Figs. 1a, b). It is well known that relative phases, amplitudes, and directions of time (DOT) for well-separated pulses or modes present difficulties for most pulse-measurement techniques. It is perhaps not so well known that another FROG variation, XFROG (when performed correctly), does not suffer from them. It is apparently also not so well known that, in our publication on the subject, we also provided a simple procedure for *removing* it (a fact unfortunately not mentioned by YKT when referencing this paper in their publication). Our method also removes the overall DOT ambiguity in SHG FROG and in addition automatically calibrates any FROG device. It involves simply replacing the beam splitter in the FROG device with an *etalon*, chosen to yield a train of overlapping pulses in each arm of the FROG. Such a train of pulses is easily measured by FROG, and retrieving the individual waveform (E) from the train (E_{train}) is trivial:

$$E(t) = E_{train}(\tilde{t})\ E_{train}(\tilde{t}T) \tag{21}$$

where T is the round-trip time of the etalon and ε is the ratio of field strengths of successive individual pulses in the train. We called our method Procedure for Objectively Learning the Kalibration And Direction Of Time (POLKADOT) FROG. In Figure 27, we show how this approach easily removes the ambiguity in the case of the double pulses mentioned by YKT.

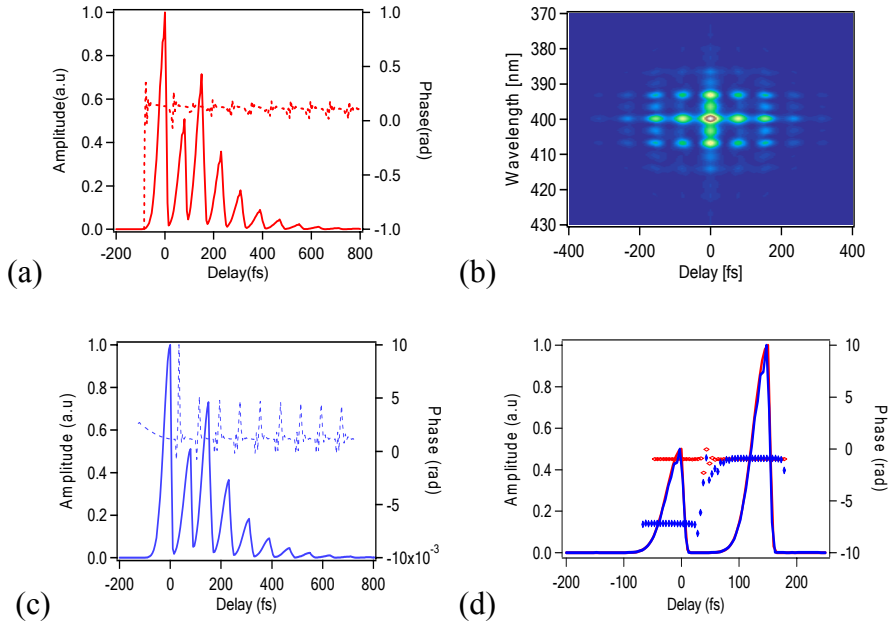

Figure 27. (a) the double pulse train after the etalon, (b) the SHG FROG trace of the etalon-transmitted pulse train, (c) the retrieved pulse train from the trace, (d) the original generated double pulse and the double pulse retrieved using $E(t) = E_{train}(t)$ $E_{train}(\tilde{t}T)$. The solid line indicates the generated pulse and the dashed line indicates the retrieved pulse. The FROG G error of the retrieval is 0.00027, and the G' error is 0.0056.

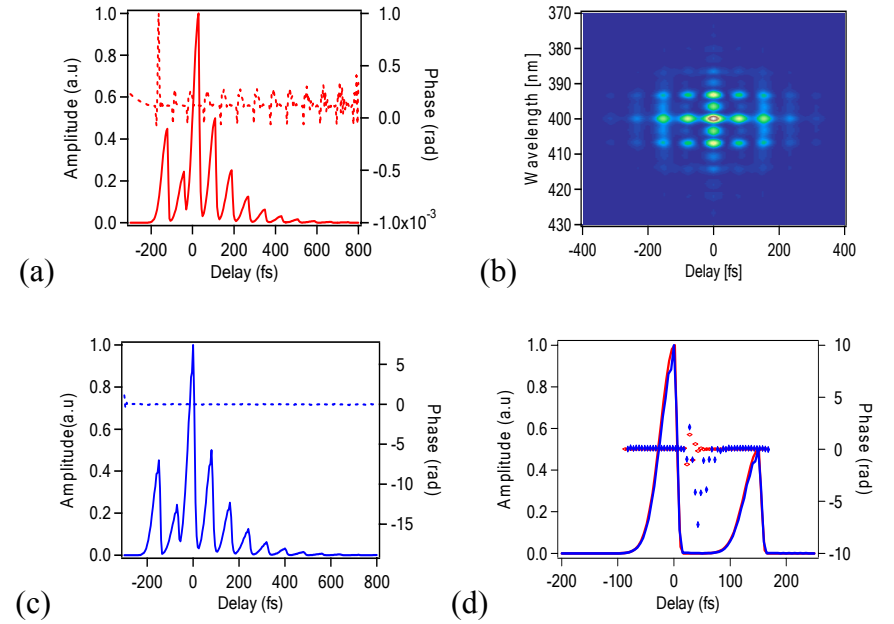

Figure 28. (a) the double pulse train after the etalon, (b) the SHG FROG trace of the etalon-transmitted pulse train, (c) the retrieved pulse train from the trace, (d) the original generated double pulse and the double pulse retrieved using $E(t) =$

$E_{train}(\tilde{t})$ $E_{train}(\tilde{tT})$. The solid line indicates the generated pulse and the dashed line indicates the retrieved pulse. The FROG *G* error of the retrieval is 0.00024, and the *G'* error is 0.0049.

YKT conclude that interferometric autocorrelation is a better approach to pulse measurement in some cases. Since neither of their examples, in fact, presents a problem for FROG, this conclusion is, of course, unjustified. However, even if these examples did present problems for FROG, intensity autocorrelation and interferometric autocorrelation (IA) (and their various relatives) do not offer appealing alternatives for measuring pulses. It is well known that pulses *cannot* be retrieved from such traces—even when additional measures (such as the spectrum) are included—unless arbitrary assumptions are made regarding the pulse or the pulse is trivially simple. Worse, even the ambiguities themselves in autocorrelation have not been determined due to the complexity of the mathematics involved. Thus, in autocorrelation, it is not possible even to know what the ambiguities are. Figure 29 show that one autocorrelation traces corresponds to many ambiguous pulse shapes. We retrieve the pulse using temporal information via intensity[66]. This is an iterative phase retrieval algorithm based on Fourier transformation. From this simulation result, we can conclude that infinitely different pulses shapes yield exactly same intensity autocorrelation trace and intensity autocorrelation is not able to retrieve the full information of the pulses.

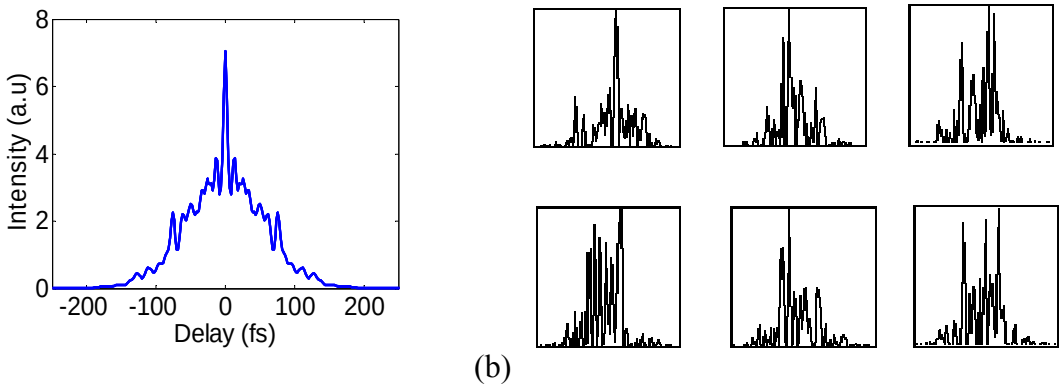

Figure 29. (a) An autocorrelation trace (b) six different pulses generating exactly same autocorrelation trace in (a)

Interferometric autocorrelation trace contains more information than intensity autocorrelation trace, but it has never been demonstrated to uniquely determine the intensity and phase of an ultrashort laser pulse. This is because the algorithm usually is hard to converge. Jung-ho Chung etc. showed numerical simulations and concluded that IAC trace might be quite challenging to distinguish in a practical experimental context[67]. We used the structured pulse in Figure 22, which is one of the pulses used in YTP paper to generate an IAC trace, then we used a phase retrieval algorithm based on iterative Fourier transform[68] to retrieve it. We found a symmetric pulse yielding a very similar IAC trace. The maximum difference between these two IAC traces is less than 0.5% which is difficult to distinguish in practice. So these two pulses are approximately ambiguous pulses. In the retrieval procedure, it is supposed know the field autocorrelation, intensity autocorrelation and the 2^{nd} order field autocorrelation. The result is shown in Figure 30.

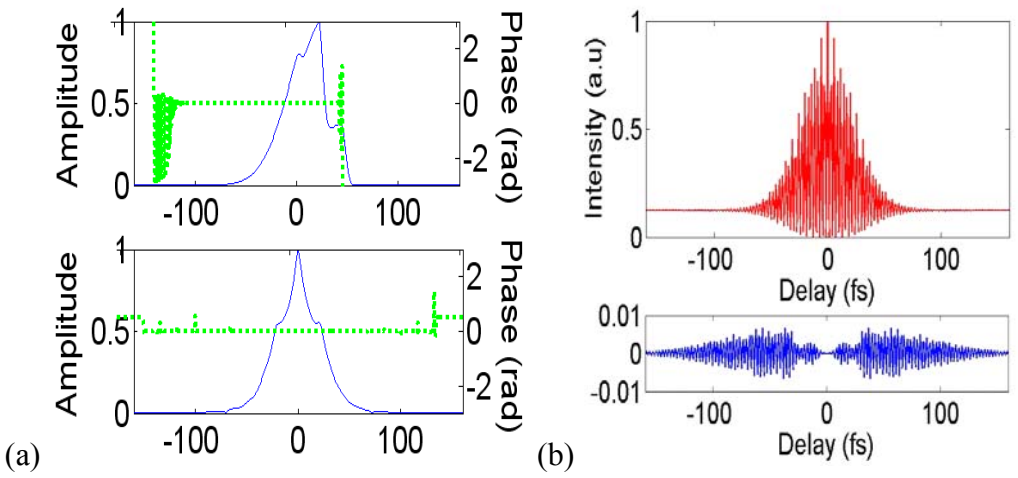

Figure 30. Two different pulses and their similar IAC traces

To further appreciate the difficulties of autocorrelation, note that, as the pulse to be measured becomes more complex, both intensity and interferometric autocorrelation traces actually become *simpler*, meaning that most information about the pulse is clearly irretrievably lost, buried in even a miniscule level of noise. See Figure 31 a, b, c. FROG, on the other hand, not only yields highly structured traces for such pulses (with structure with close to 100% visibility) (Figure 28d); it can retrieve their complete intensity and phase, as has been demonstrated.

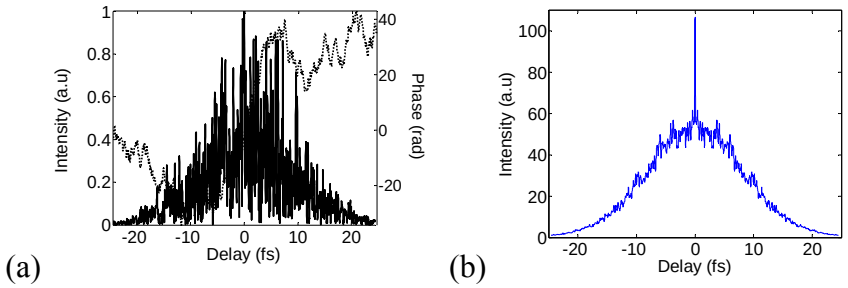

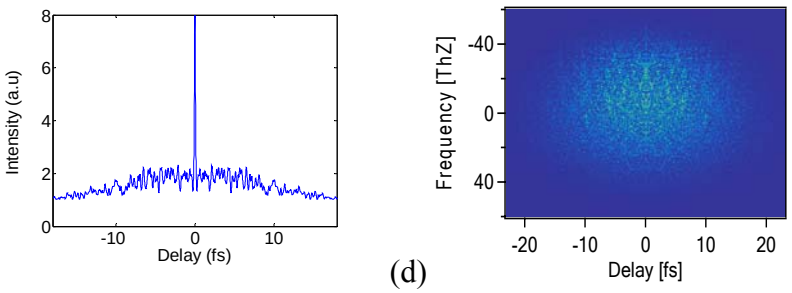

(c) (d)

Figure 31. (a) Generated complex pulse with TBP of 475, (b) Intensity autocorrelation trace of this complex pulse, (c) Interferometric autocorrelation trace of this complex pulse, (d) SHG FROG trace of this complex pulse. While the structure (which contains the pulse information) in the autocorrelation and interferometric autocorrelation is nearly washed out, the highly complex structure in the FROG trace has a visibility of close to 100%.

CHAPTER 5

MEASUREMENT OF THE POLARIZATION STATE OF AN ULTRASHORT LASER PULSE (TURTLE)

This chapter originally appeared as a paper by the author:

L. Xu, P. Schlup, O. Masihzadeh, R. A. Bartels, and R. Trebino, Analysis of the measurement of polarization-shaped ultrashort laser pulses by tomographic ultrafast retrieval of transverse light E-field (TURTLE), submitted to J. Soc. Am. B.

5.1. Introduction

Polarization-varying complex ultrashort laser pulses were first used in quantum control [69-73], and are now playing roles in many areas of research. Such "polarization-shaped" pulses have been considered for the generation and measurement of high-harmonic pulses [74] and for the control of two-dimensional lattice vibrations in crystals [75]. Polarization-shaped pulses have been generated by various means, mostly based on Fourier-domain pulse shaping of individual polarization components [71, 76-79]. On the other hand, only a few methods exist to measure them. Time-resolved ellipsometry (TRE) [80, 81] was one of the first technologies used to characterize the polarization evolution of ultrashort pulses. It involves measuring all four Stokes parameters of the pulse, but it is labor intensive. A simpler technique is POLLIWOG [82], which uses spectral interferometry [83] to characterize, successively or simultaneously, the two orthogonal polarization components relative to a well-characterized reference pulse. Other approaches involve measuring the spectrum and cross-correlation of the polarization components or the cross-phase modulation, both combined with iterative numerical algorithms [84, 85]. POLLIWOG is the most commonly used technique, and it works

well, but it requires careful phase stabilization and measurement of the relative phase between the two polarizations, and it requires a separate self-referenced technique for measuring the required reference pulse.

Recently, we introduced a self-referenced technique for measuring polarization-shaped pulses, which we called tomographic ultrafast retrieval of transverse light *E*-fields (TURTLE) [86]. It does not require a separate well-characterized reference pulse and is based on measuring the electric field vs. time at three different linear polarizations, obtained by making such measurements after a polarizer for three different polarizer angles. Two of the measurements characterize the electric field for mutually orthogonal field components, and the third, measured at an arbitrary angle in between (typically 45°), is used to determine the phase relationship between these components, which yields the full vector polarization evolution of the pulse. Any established method that determines the complex field $\tilde{E}(\Omega)$ of a single, linear polarization can, in principle, be used in TURTLE. In addition the pulse energy or average power must be measured for each polarization. No modifications to the standard pulse-measurement apparatus are needed.

Here we study the TURTLE technique using SHG FROG by performing detailed simulations. We simulate TURTLE's performance using SHG FROG for simple and complex polarization-shaped pulses and find that it works very well, even for very complex pulses. Our simulations show that an error minimization algorithm using the SHG FROG trace performs robustly, even in the presence of additive noise. We attribute this robust behavior to the well-known over-determination of the pulse complex electric field afforded by a FROG trace.

We chose FROG because it is the most mature self-referenced pulse measurement technique available and has been shown to measure accurately the full intensity and phase of an arbitrary complex ultrashort pulse [32], subject only to trivial ambiguities. Specifically we chose SHG FROG due to its high sensitivity and prevalence. Trivial ambiguities of standard SHG FROG include the direction of time (DOT) of the pulse; that is, SHG FROG cannot distinguish between a reconstructed field $\tilde{E}(\Omega)$ and its complex conjugate, $\tilde{E}^*(\Omega)$. For pulses that are well-separated in either optical frequency or time, an additional ambiguity arises in their relative phases $\Delta\varphi$.[11, 30] For example, relative phases of φ and $\Delta\varphi + \pi$ yield the same SHG FROG trace for double pulses in time. However, it has been shown that these trivial ambiguities can easily be removed using simple techniques that involve minimal additional effort. Adding a known spectral dispersion (chirp) and performing a second FROG measurement removes the DOT ambiguity. Even better, replacing the FROG beam splitter with an etalon generates identical trains of overlapping (and decaying) pulses in both arms of the device; such waveforms do not experience such ambiguities, and the original pulse can be retrieved from them easily and unambiguously [20], except for the usual absolute-phase and arrival-time ambiguities common to all self-referenced pulse-measurement techniques. Thus FROG and its variations yield the best-posed (least ambiguous) set of self-referenced pulse-measurement techniques currently available.

While these remaining two ambiguities are generally considered trivial, and they are not so trivial for the measurement of polarization-shaped pulses. Non-measurement of the absolute phase and time preclude the determination of key quantities of the full vector field. Specifically, what distinguishes monochromatic 45° linear polarization from

circular polarization is the relative phase of the horizontal and vertical polarizations, which is the difference between the two pulse absolute phases, which are not measured in self-referenced pulse-measurement techniques in general. And what distinguishes a 45° linear polarization from two well-separated pulses of orthogonal polarization is, of course, their relative arrival times. Thus these two trivial ambiguities are not so trivial for polarization-shaped pulses and thus become the principal unknowns that TURTLE aims to determine. It is the third FROG trace that accomplishes this. The only case we have found in which TURTLE, as described above, does not work is the trivial case in which the two polarization components are identical, and the polarization thus does not actually evolve, but this ambiguity can easily be removed with one additional measurement.

5.2. TURTLE theory

In the frequency domain, we write the polarization-shaped vector field as

$$\tilde{\boldsymbol{E}}(\Omega) = \tilde{E}_x(\Omega)\,\hat{\mathbf{x}} + r\tilde{E}_y(\Omega)e^{-i(\Omega\tau+\theta)}\,\hat{\mathbf{y}} \qquad (22)$$

where the optical angular frequency $\Omega \equiv \omega - \omega_0$, and $\tilde{E}_x(\Omega)$ and $\tilde{E}_y(\Omega)$, represent the complex frequency-domain polarization components along the Cartesian axes, with the beam propagating along $\hat{\mathbf{z}}$. We use this formulation because ultrafast polarization-shapers typically operate by independently shaping orthogonal polarization components. To obtain the full polarization information, we need to know, not only the fields $\tilde{E}_x(\Omega)$ and $\tilde{E}_y(\Omega)$, but also the relative amplitude r, relative delay τ, and relative phase θ between the components. No existing self-referenced single-polarization pulse-measurement technique is able to provide absolute time or phase information, but it is easy to measure

the relative amplitude using a simple energy detector, as given below. The measurement technique that we call tomographic ultrafast retrieval of transverse light *E*-fields, or TURTLE, determines these relative quantities from an additional SHG-FROG trace of the polarization component, here projected at 45° between $\hat{\mathbf{x}}$ and $\hat{\mathbf{y}}$. In the following, we label this projection angle η.

The easiest ambiguity to resolve is the relative amplitude ratio r. We can determine it experimentally by measuring the average power P for each linear projection measurement. The power can be written as

$$P \propto \int_{-\infty}^{\infty} |r' \tilde{E}(\Omega)|^2 \, d\Omega = r'^2 \int_{-\infty}^{\infty} |\tilde{E}(\Omega)|^2 \, d\Omega \qquad (23)$$

where r' is a scaling factor that relates the reconstructed, arbitrarily normalized field $\tilde{E}(\Omega)$ to the physically present field. So, if we normalize the retrieved fields according to $\int|\tilde{E}(\Omega)|^2 \, d\Omega = 1$, then we can find r in Eq. (1) from $r = \sqrt{P_y / P_x}$. As we show below, the power measurements are critical for the trivial case of pure elliptical polarization as shown below, where the reconstructed fields are identical except for the amplitude factor. In the following simulations, we set $r = 1$ without loss of generality.

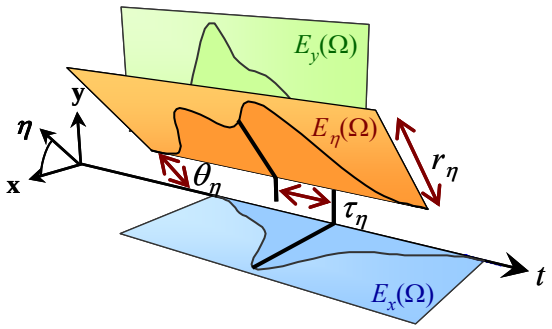

Figure 32. Schematic visualization of the TURTLE principle. The time-evolving electric field vector $\mathbf{E}(t)$ (not shown) is characterized by measuring linear

projections $\tilde{E}_x(\Omega)$, $\tilde{E}_y(\Omega)$, and $E_\eta(\Omega)$ in the frequency domain using an existing ultrashort pulse characterization technique. The algorithm establishes the relative amplitude r, delay τ, and phase θ between the projections to retrieve the full vector field.

TURTLE aims to determine the relative delay τ and phase θ in Eq. (1) using an additional polarization projection at angle η. We denote this projected field $\tilde{E}_\eta(\Omega)$, and it can be written as

$$\tilde{E}_\eta(\Omega) = \cos\eta\, \tilde{E}_x(\Omega) + r \sin\eta\, \tilde{E}_y(\Omega)\, e^{-i(\Omega\tau + \theta)} . \tag{24}$$

A choice of $\eta = 45°$ will usually give the best results because $\tilde{E}_x(\Omega)$ and $\tilde{E}_y(\Omega)$ contribute equally to the projected field, $\tilde{E}_\eta(\Omega)$. We choose this angle in the simulations below.

The expression for the SHG FROG trace of a single, linearly-polarized pulse temporal electric field $E(t)$ is [16]

$$I_{\mathrm{FROG}}(\omega, T) = \left| \int_{-\infty}^{\infty} E(t)\, E(t - T)\, e^{-i\omega t}\, dt \right|^2 . \tag{25}$$

The FROG trace is collected by recording the second-harmonic spectra generated as the delay T between two replicas of $E(t)$ is varied. From the SHG FROG trace, an established generalized projections algorithm reliably finds the full intensity and phase of an arbitrary ultrashort laser pulse[16]. Thus, $\tilde{E}_x(\Omega)$ and $\tilde{E}_y(\Omega)$ can readily be determined experimentally without the need for additional reference pulses.

Having found $\tilde{E}_x(\Omega)$ and $\tilde{E}_y(\Omega)$, we use a minimization algorithm to find the relative delay τ and relative phase θ for which $\tilde{E}_x(\Omega)$ and $\tilde{E}_y(\Omega)$ yield the projected field

$\tilde{E}_\eta(\Omega)$. The algorithm can find these parameters using the additional information contained in the η-projected SHG FROG trace. We sample the FROG traces onto regularly-spaced optical frequency ω_i and delay T_j axes in an $N \times N$ grid. We calculate the projected FROG trace from $\tilde{E}_\eta(\Omega)$ using Eq. (4), and TURTLE involves minimizing the difference between the calculated $I_\eta^{\text{calc}}(i,j)$and measured $I_\eta^{\text{meas}}(i,j)$ traces. We use the criterion or RMS error defined as [51],

$$e = \frac{\sqrt{\sum_{i,j=1}^{N}\left[I_\eta^{meas}(i,j) - I_\eta^{calc}(i,j)\right]^2}}{\sqrt{\sum_{i,j=1}^{N}\left[I_\eta^{meas}(i,j)\right]^2}}, \tag{26}$$

which describes the difference between the two FROG traces I_η^{meas} and I_η^{calc} divided by the non-zero area. The error e is then minimized with respect to the iterated values of τ and θ, with the optimal values corresponding to those values of τ, θ that minimize e. In the simulations, we calculate the error surface $e(\tau, \theta)$ about the optimal values.

We must also ensure that TURTLE uses the correct *relative* DOT between the components $\tilde{E}_{x,y}(\Omega)$, since a wrong DOT in one projection and the correct DOT in the other no longer corresponds to the vector field being measured. This ambiguity is easily resolved in two ways: We can determine the overall correct DOT for both fields, $\tilde{E}_x(\Omega)$ and $\tilde{E}_y(\Omega)$, by placing an etalon, or adding a known amount of material chirp, in one of more of the SHG FROG measurements. This is the standard method for resolving the time ambiguity in SHG FROG. In TURTLE, knowing the DOT of one component, $\tilde{E}_x(\Omega)$ or $\tilde{E}_y(\Omega)$ is sufficient to determine that of the other and hence that of the entire

polarization-shaped pulse. In other words, if only the shape of the vector field, but not its absolute DOT, is needed, we can calculate the error $e(\tau,\theta)$ separately for both combinations of relative DOTs: $\tilde{E}_x(\Omega) + \tilde{E}_y(\Omega)$ and $\tilde{E}_x(\Omega) + \tilde{E}_y^*(\Omega)$. The TURTLE trace for non-trivial vector pulse shapes is sensitive to the relative DOT, so the minimum error in e will be lower for the correct relative DOT.

To simulate the practical environment, we added 0.5% Poisson noise to each SHG FROG trace. In this approach, the measured trace with such additive noise [16] at each pixel We verified that the maximum trace value at the edges of the array is less than 0.5% of the peak value of the FROG trace. Suppressing background noise is important in SHG FROG measurements. Any non-zero average background (due to noise) in a FROG trace implies spurious nonzero intensity at large times and with high frequency in the pulse, that is, spurious pulse wings with high frequency noise. So, in practice, before running the pulse retrieval program, background subtraction is always performed. Several methods are available, and they include Fourier low-pass filtering, corner-suppression, and mean background subtraction. In our simulations, we chose to perform only simple mean-background subtraction (although performing the others as well would likely have further improved the performance beyond what we observe). The mean of the noise was obtained by averaging the values in the 5x5 pixel squares in the four corners of the FROG trace (i.e., far from the center of the trace, where the most important pulse information is located). After subtracting this constant background from all points in the trace, we set all the resulting negative points to zero (as is usually done).

We found the values of the relative phase and delay using the 45°-polarized FROG trace and the fields determined from the x- and y-polarized traces, using a

MATLAB Nelder-Mead minimization routine for multi-dimensional unconstrained optimization[87]. This routine is ideal for the TURTLE technique because, whileNelder-Mead routines are known to be slow, TURTLE involves only a two-parameter minimization, and so it converges relatively quickly. Although Nelder-Mead minimization only finds the local minimum, this drawback can be overcome by using different initial guesses.

5.3 TURTLE simulations

Below we give several examples of using the TURTLE technique to find the polarization state of an ultrashort pulse. While the majority of TURTLE measurements are anticipated to be used to characterize complex pulses with complex polarization evolution, we begin with some simple cases, since the extremely simple case of non-evolving-polarization with identical x and y components revealed the only ambiguity we encountered in our study. The ambiguity disappears in the presence of even slight polarization complexity and so is unlikely to present problems for the use of TURTLE.

The first example pulse comprises two identical $\hat{\mathbf{x}}$ and $\hat{\mathbf{y}}$ components consisting of transform-limited Gaussian pulses with a full width at half maximum (FWHM) duration of 30 fs, so that $E_x(t) = \exp\{-2\ln 2\,[t / 30\text{ fs}]^2\}$ and $E_y(t) = \exp\{-2\ln 2\,[(t + \tau/2) / 30\text{ fs}]^2\}$. The relative delay and phase between the polarization components was $\tau = 170$ fs and $\theta = \pi/3$. The resulting SHG FROG traces for the projected fields $\tilde{E}_x(\Omega)$, $\tilde{E}_y(\Omega)$ and $\tilde{E}_\eta(\Omega)$ are shown in Figgure 30 (a), (b), and (c), respectively. In Figure 33 (d) and (e), we show the pulse intensity and temporal phase reconstructed from the SHG FROG traces for $E_x(t)$ and $E_y(t)$. The peak intensity is set at $t = 0$. The zero order and first order spectral phases,

which correspond to the relative phase and delay in the evolution of the polarization, are not reflected in these two retrieved fields. The relative phase and delay are obtained from the SHG FROG trace of $\tilde{E}_{\eta}(\Omega)$. Since the pulses are symmetrical in time and frequency, the reconstructed field projections closely match the generating fields, in particular with regard to the absolute time and phase of each component.

Figure 33 (f) shows the error surface e, about the target value of τ and θ, calculated using the reconstructed $\tilde{E}_{x,y}(\Omega)$ and the η-projected FROG trace I_{η} from Eq. (26). On this error surface, the parameter minimization retrieved a relative delay of 169.65 fs and a relative phase is 0.3344π or 1.3316π rad, depending on the initial guess. This is the expected π-rad phase ambiguity that arises from SHG FROG traces for pulses separated in time; as discussed above, an additional measurement by adding additional chip on either one of the pulses or both pulse to make $E_x(t)$ and $E_y(t)$ overlap in time can be used to eliminate this ambiguity. A three-dimensional representation of the vector field $\mathbf{E}(t)$ is sketched in Figure 30. Examination of the η-projected SHG FROG trace of Figure 33 (c) reveals spectral intensity modulations at a FROG delay of $T = 0$. As discussed in Section 2.1, these fringes correspond to spectral interferometry fringes, and their spacing is inversely proportional to τ, and the peak locations relative to $\Omega = 0$ is given by θ.

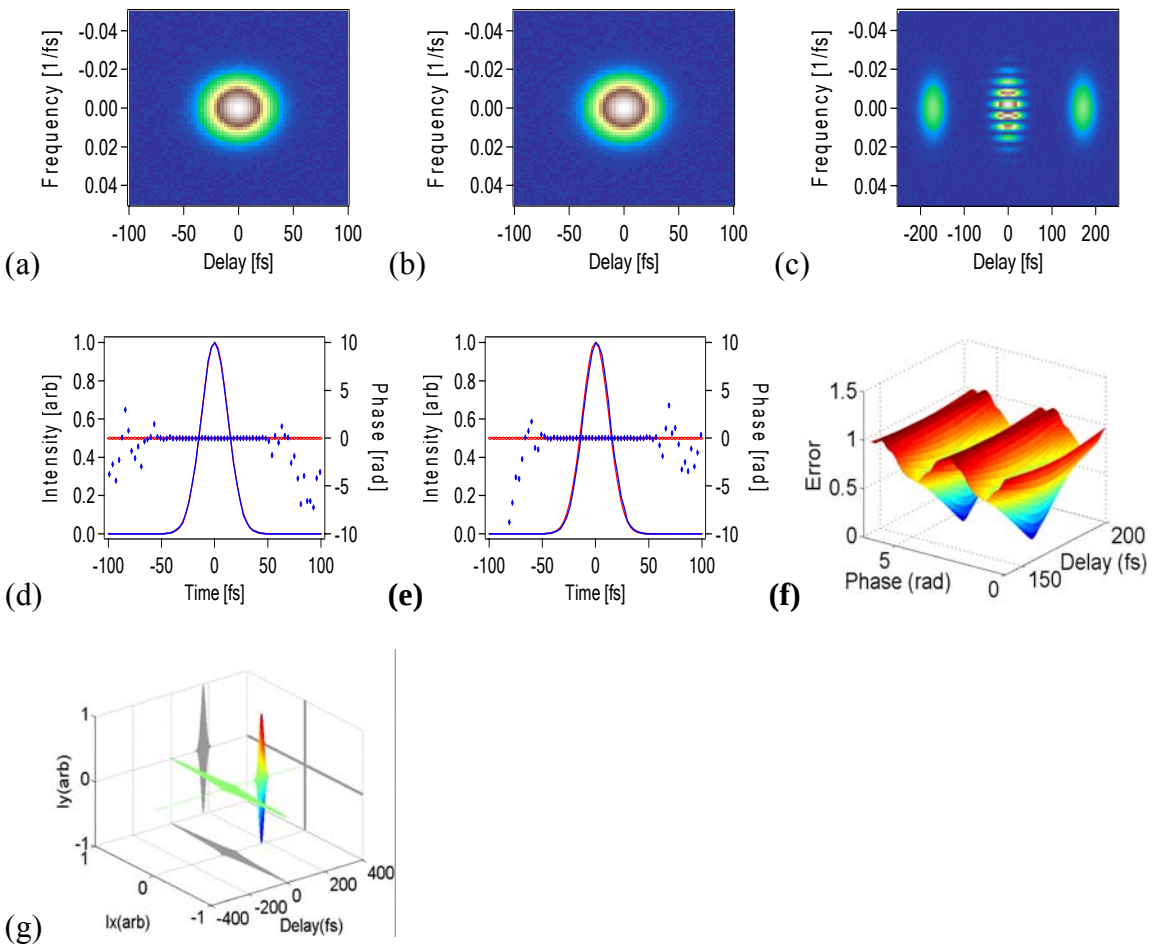

Figure 33.TURTLE retrieval steps for a vector field consisting of two transform-limited Gaussian components separated by 170 fs.

(a), (b), (c), Simulations of measured SHG FROG traces for $\tilde{E}_x(\Omega)$, $\tilde{E}_y(\Omega)$ and $\tilde{E}_\eta(\Omega)$, with $\eta = 45°$. (d), (e), Pulse fields $E_x(t)$, $E_y(t)$ obtained using the standard reconstruction algorithm (blue dots), compared to the generating fields (red solid line). (f) The error surface; the two minima indicate the π rad phase ambiguity arising from the SHG FROG trace of two pulses well separated in time. (g) Sketch of the full vector field $\mathbf{E}(t)$.

Combining the identical fields $\tilde{E}_x(\Omega)$ and $\tilde{E}_y(\Omega)$ from the previous example with $\tau = 0$ and $\theta = \pm\pi/2$ yields a circularly-polarized pulse shown in Figure 34. In this case, we can relate the field components by $\tilde{E}_y(\Omega) = \tilde{E}_x(\Omega)e^{-i\theta}$, so that the η-projected SHG FROG trace for $\eta = 45°$ will be given by

$$I_{\mathrm{FROG}}(\omega, T) = \left|(1 + e^{-i\theta})^2\right|^2 \left| \int E_x(t)\, E_x(t - T) e^{-i\omega T}\, \mathrm{d}t \right|^2. \tag{27}$$

Thus, the projections $\hat{\mathbf{x}}$ and $\hat{\mathbf{y}}$ yield identical SHG FROG traces, Figure 34 (a), with the η-projection being qualitatively the same but scaled by an intensity-weighting factor of $|(1 + e^{-i\theta})^2|^2 = [2(1 + \cos\theta)]^2$. Since this factor does not depend on the sign of θ, which determines the handedness of the vector field, TURTLE cannot distinguish between left and right circularly polarized fields. This can be seen in the error surface shown in Figure 34(b), which indicates two symmetric minima at $\pm\theta$. The TURTLE fitting algorithm retrieved a relative delay of $\tau = 0.0174$ fs and a relative phase of $\theta = 0.5014\pi$ or -0.5015π rad, depending on the initial guess. Further, in this case of indistinguishable SHG FROG traces, the normalization of Eq. (26) and that inherent in the standard FROG reconstruction algorithm means that the ellipticity, determined by the relative amplitude r of the $\hat{\mathbf{x}}$ and $\hat{\mathbf{y}}$ components, cannot be directly determined. The independent power or pulse energy measurement is thus necessary to determine the ellipticity.

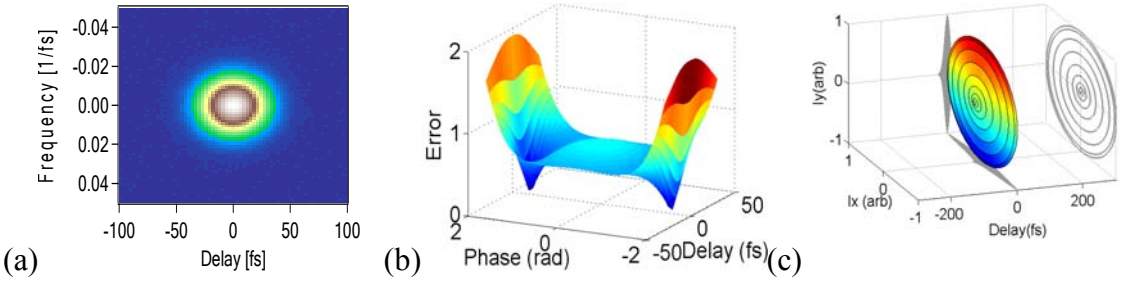

Figure 34. (a) Simulation of measured SHG FROG traces, in this case all three projections yield the same trace. (b) The error surface; the two minima indicate an ambiguity in the chirality of the vector field $\mathbf{E}(t)$, which is shown in (c).

The handedness ambiguity can be resolved by introducing different chirps to the two components, as shown in Figure 32 Here, we added $\varphi^{(2)}(\Omega) = \pm 200$ fs^2/rad quadratic

spectral phase to each of the $\tilde{E}_{x,y}(\Omega)$. The SHG FROG traces for these components are still indistinguishable, Figure 35 (a), but, due to the knowledge of the signs of the added chirps, we can correctly reconstruct the fields as shown in Figure 35 (b),(c). The η-projected SHG FROG trace, shown in Figure 35 (d), is now distinct, and its shape uniquely determines the correct phase since the error surface, Figure 35 (e), exhibits only a single minimum. The retrieved relative delay and phase were $\tau = -1.0242$ fs and $\theta = 0.5183\pi$ rad, identifying the pulse as right circularly polarized. Alternatively, we could characterize the pulses transmitted through a circular polarizer, analogously to the determination of one of the four Stokes vectors needed to fully define the vector field. The ambiguity in the sign of θ arises only in the case of transform-limited, temporally symmetric pulses, and is not expected to occur for polarization-shaped pulses.

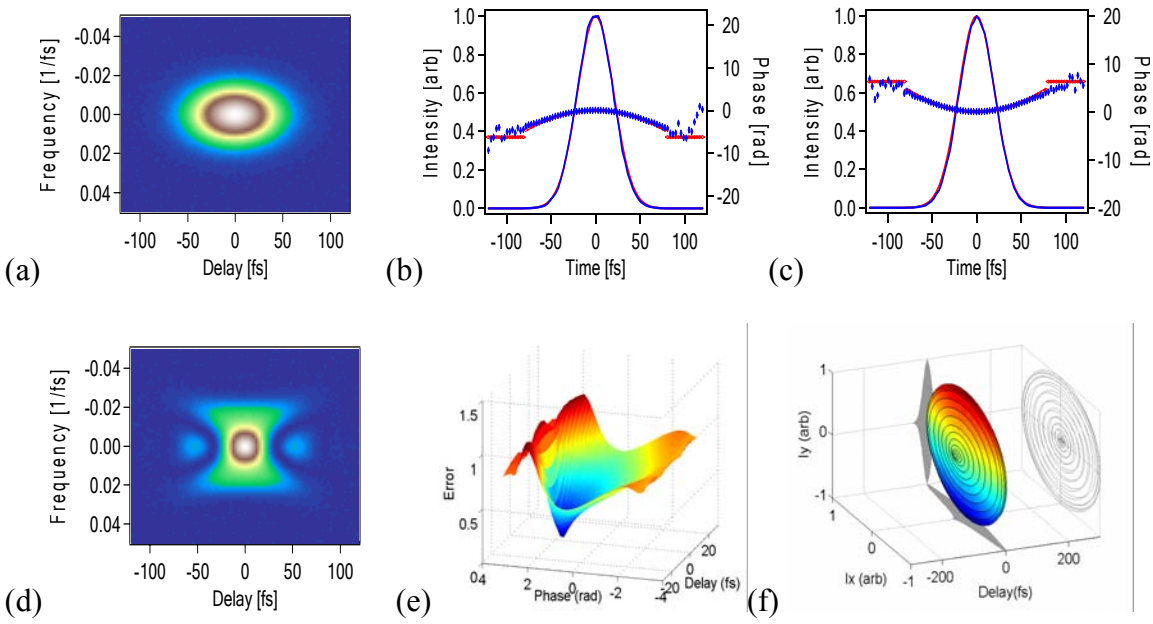

Figure 35. Establishing the chirality of a circularly polarized field by adding a known chirp

(a) Simulation of measured SHG FROG trace for $\tilde{E}_x(\quad)$; an identical trace is recorded for $\tilde{E}_y(\quad)$. (b), (c), Pulse fields $E_x(t)$, $E_y(t)$ obtained using the standard

reconstruction algorithm (blue dots), compared to the generating fields (red solid line). (d) SHG FROG trace for the -projected component. (e) The error surface that shows only a single minimum at = +π/2. (f) Sketch of the full vector field **E**(*t*).

We show in Figure 36 results from a randomly-generated, more complex pulse. We simulate an arbitrary vector field **E**(*t*) by creating a random complex field components for $\tilde{E}_x(\Omega)$ and $\tilde{E}_y(\Omega)$, and applying Gaussian amplitude filters in both time and frequency domains. For the pulse shown in Fig. 5, the temporal and frequency filter FWHM widths were Δt = 180 fs and $\Delta\Omega$ = 0.3 rad/fs. The resulting time-bandwidth products (TBP) were 17.8 for the **x̂**-, 13.0 for the **ŷ**-polarized components. We chose relative delay and phase values of τ = 60 fs and θ = π/3 rad, respectively. The SHG FROG traces of Figure 36 (a),(b),(c) show rapid structure characteristic of non-trivial pulses. As shown in Figure 36 (d),(e), we verified that the FROG reconstructions were in good agreement with the generating fields, and from the error surface, Figure 36 (f), the minimization algorithm retrieved relative delay and phase values of 62.74 fs and 0.3349π rad, respectively.

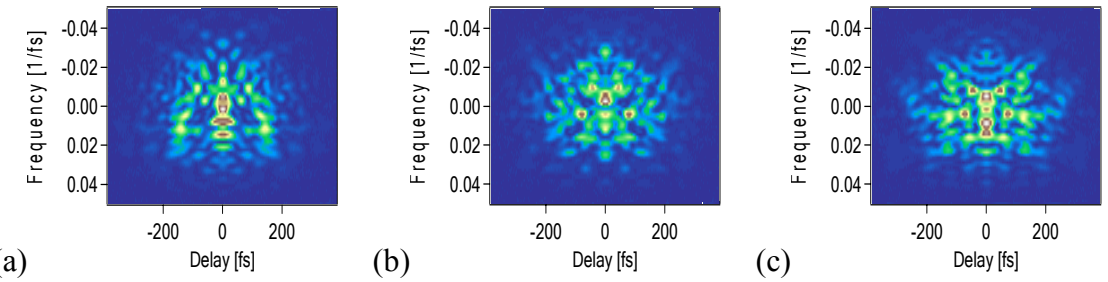

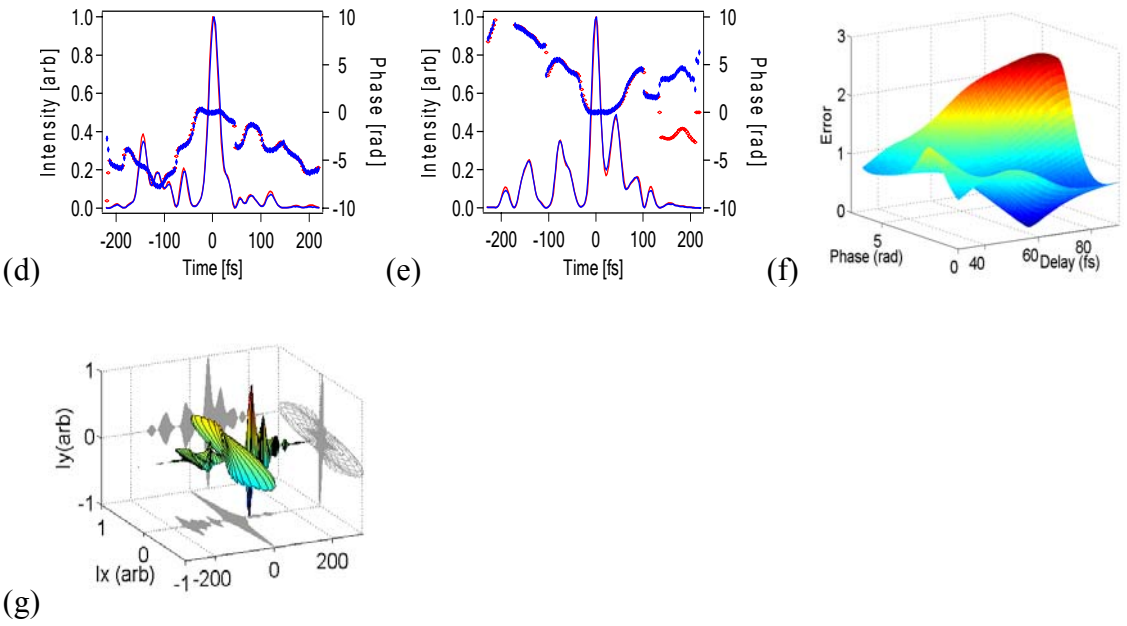

Figure 36. TURTLE retrieval steps for a randomly-generated vector field

(a), (b), (c), Simulations of measured SHG FROG traces for $\tilde{E}_x(\quad)$, $\tilde{E}_y(\quad)$ and $\tilde{E}\ (\quad)$. (d), (e), Pulse fields $E_x(t)$, $E_y(t)$ obtained using the standard reconstruction algorithm (blue dots), compared to the generating fields (red solid line). (f) The error surface; and (g) sketch of the full vector field $\mathbf{E}(t)$.

Another case with a more complex pulse is shown in Figure 37. The method to generate these two complex pulses is same as the previous case. The temporal and frequency filter FWHM widths in this case were Δt = 1800 fs and $\Delta\Omega$ = 0.3 rad/fs. The resulting time-bandwidth products (TBP) were 169.7 for the $\hat{\mathbf{x}}$-, 180.4 for the $\hat{\mathbf{y}}$-polarized components. Due to the limitation of the computer memory, these are the most complicated pulse generated. We chose relative delay and phase values of τ = 500 fs and $\theta = \pi/3$ rad, respectively. The SHG FROG traces of Figure 37 (a),(b),(c) show rapid structure characteristic of highly non-trivial pulses. As shown in Figure 37 (d),(e), we verified that the FROG reconstructions were in good agreement with the generating fields, and from the error surface, Figure 37 (f), the minimization algorithm retrieved relative delay and phase values of 504.96 fs and 0.35π rad, respectively.

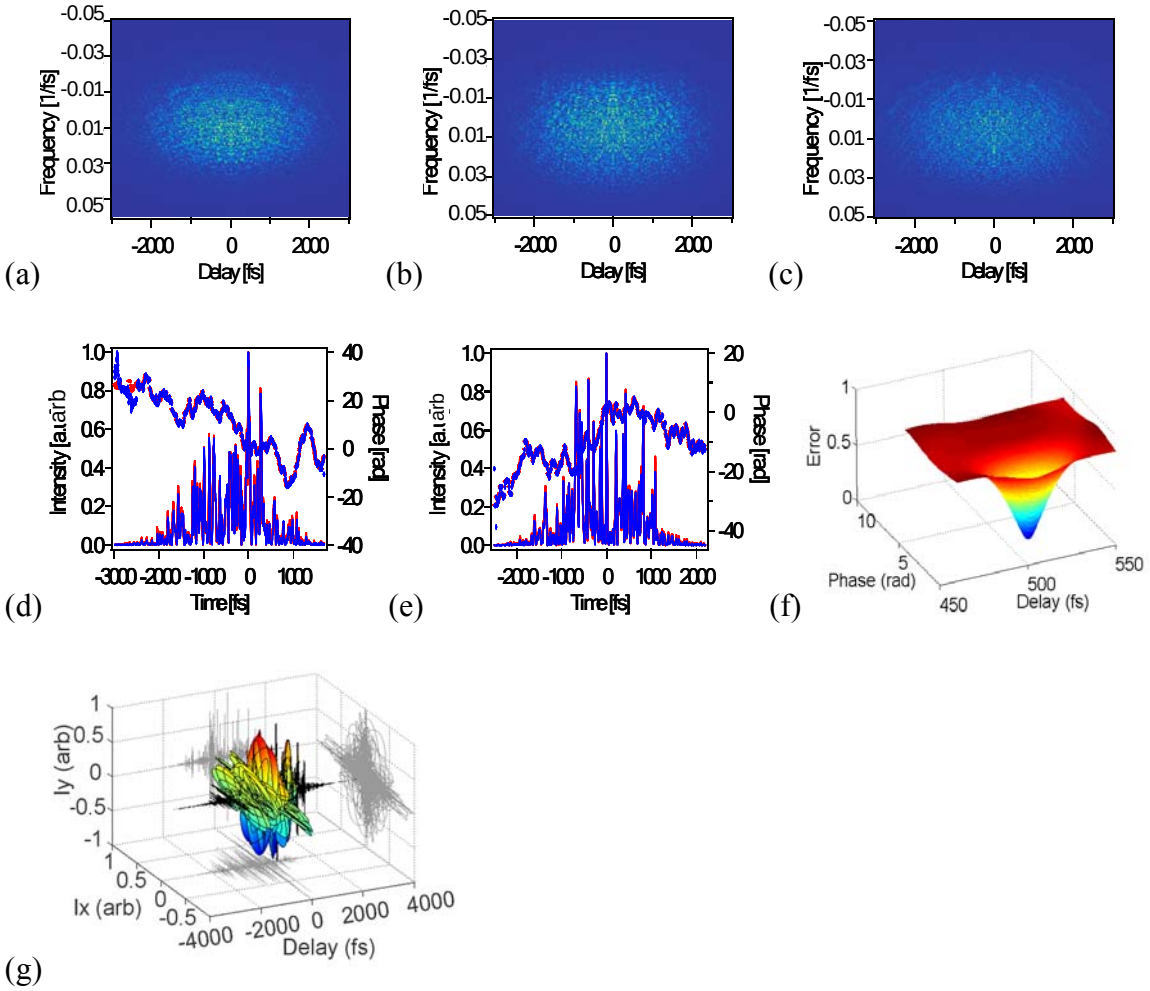

Figure 37. TURTLE retrieval steps for a randomly-generated very complex vector field. (a), (b), (c), Simulations of measured SHG FROG traces for $\tilde{E}_x(\quad)$, $\tilde{E}_y(\quad)$ and $\tilde{E}\ (\quad)$. (d), (e), Pulse fields $E_x(t)$, $E_y(t)$ obtained using the standard reconstruction algorithm (blue dots), compared to the generating fields (red solid line). (f) The error surface; and (g) sketch of the full vector field $\mathbf{E}(t)$.

Table 2. shows some cases with different pulse complexities. All these x and y components are generated from random pulses filtered by a clean Gaussian pulse with FWHM widths of Δt = 900 fs in the time domain and $\Delta\Omega$ = 0.3 rad/fs in the frequency domain. We chose relative delay and phase values of τ = 500 fs and $\theta = 0.33\pi$ rad, respectively for all cases. Without any noise added, the exactly correct relative delay and

relative phase can be reconstructed in each case. With 0.5% Poisson noised added, the retrieved values are varied by at most 1.3% in relative delay and 7.5% in relative phase.

Table 2. Different pulses with their reconstructed relative delay and relative phase.

TBP (x component)	TBP (y component)	Reconstructed τ	Reconstructed θ
84	121.8	501.23	0.329π
103.3	95	493.65	0.359π
57.7	89.5	501.59	0.325π
70.5	37.5	497.52	0.329π
100.4	79.2	499.54	0.333π
83.2	110.7	504	0.318π

5.4. Conclusions

We have analyzed the performance of TURTLE using SHG FROG for the self-referenced measurement of the complete vector-field intensity and phase of polarization-shaped ultrashort laser pulses. Our simulations show that TURTLE works very well, robustly yielding the complete vector polarization even of very complex pulses and in the presence of noise. Indeed, SHG FROG TURTLE minimization also reliably distinguishes the relative DOT of the polarizations. We found no nontrivial ambiguities. We expect this success to extend to TURTLE based on other FROG nonlinearities. We conclude that SHG FROG-based TURTLE is a reliable technique for self-referenced measurements of polarization states of even very complex polarization-shaped pulses.

CHAPTER 6

MEASURING TWO COMPLEX PULSES SIMULTANEOUSLY BY PG BLIND FROG

6.1 Introduction

Although, most applications of ultrashort pulses simply require the measurement of a single pulse, there are instances when the simultaneous characterization of two complex pulses is required. For example, when probing a material, both the input and the output pulses are required to obtain the properties of the material like the refractive index and the absorption coefficient [88, 89]. Some groups use autocorrelation and spectrum to characterize the property of the material. As mentioned in Chapter 1, autocorrelation fails to yield the phase information of the pulse which is very important to determine the optical property of the material. As a result, such method would lack sufficient information to determine the absorption coefficient or the refractive index of the material. Therefore, a technique to fully characterize the two pulses simultaneously would be useful. TREEFROG[90] is the first technique to measure two pulses simultaneously in a single spectrogram. It is based on multi-shot SHG FROG technique and a two-dimension blind deconvolution[91]. Unfortunately, it is not applicable to a complex pulse or a super continuum due to the limitation of the phase matching bandwidth from the second order nonlinear crystal. Additionally, TREEFROG needs an additional measurement on the spectrum of one of the unknown pulses to let the algorithm converge. Another technique[92] based on single shot PG FROG technique with the eigenvector method is also mentioned. But the phase of the gate pulse cannot be obtained because it uses PG

FROG technique and the gate pulse is the pulse intensity. The measured PG FROG trace does not contain the phase information of the gate pulse. Measuring two complex pulses or super continuum simultaneously in a single, simple and reliable device brings more difficult, but measuring two complex pulses simultaneously is needed in ultrafast laser pulse measurement. In this thesis, we use Polarization-gate (PG) blind FROG to solve this problem. The word "blind" comes from the two unknown pulses. It is unlike the traditional FROG technique in which either the unknown pulse gates itself or a known reference gates the unknown pulse. In PG blind FROG the unknown pulses gate each other; so we will have two traces. This is different from TREEFROG and the other techniques based on PG FROG. PG blind FROG consists of two PG FROG measurements and one iterative phase retrieval algorithm based on the GP algorithm. The phase information of each unknown pulse is contained in the PG FROG trace where this pulse acts as a probe pulse. The intensity of this probe pulse is constrained by the other PG FROG trace. Due to the constraint of the pulse intensity in the PG FROG trace, at this point no additional measurement of the spectrum is needed. This is different from previous techniques that need addition spectrum information to make the algorithm converge.

6.2 PG blind FROG Simulation

PG blind FROG involves using pulse 1 (gate pulse) to gate pulse 2 (probe pulse) on a $\chi^{(3)}$ nonlinear medium and vice versa. This is shown in Figure 38. The $\chi^{(3)}$ nonlinear medium can be a piece of glass or a piece of fused silica. Two PG FROG traces will be obtained on the camera.

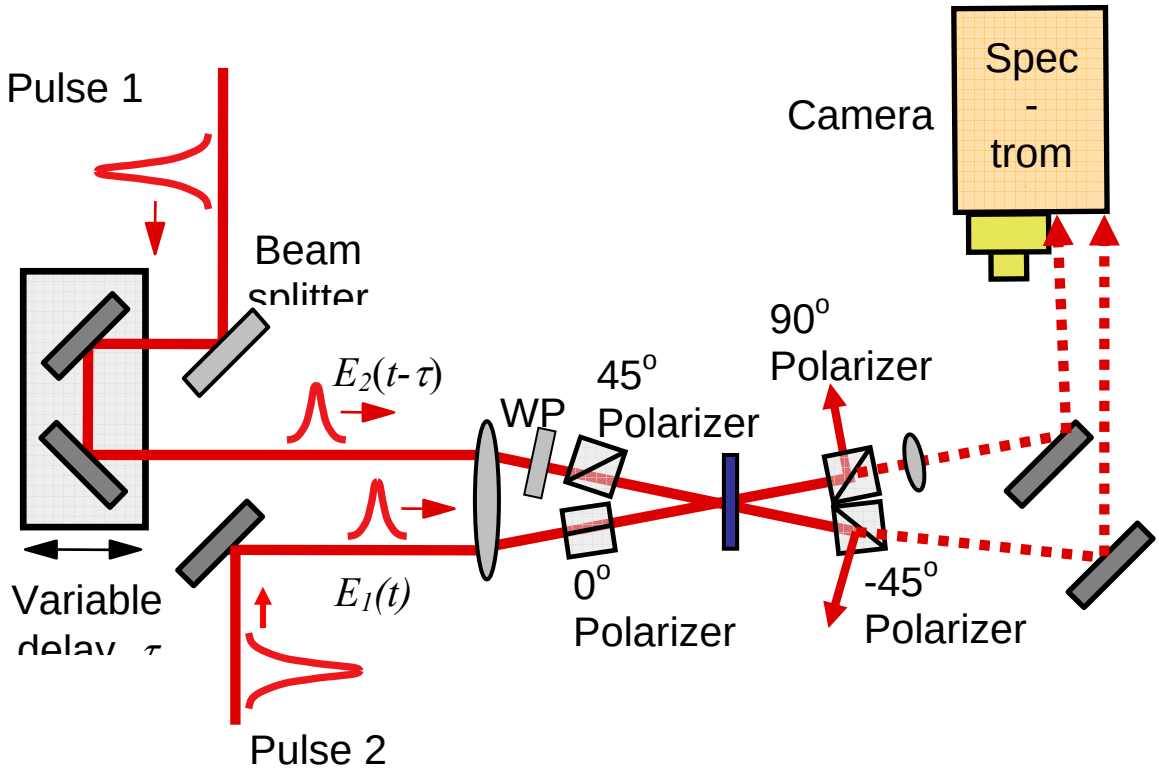

Figure 38. Apparatus of TG double Blind FROG

PG blind FROG can be described mathematically as

$$I_1(\omega,\tau)=\left|\int E_1(t)\left|E_2(t-\tau)\right|^2 e^{-i\omega t}dt\right|^2$$
$$I_2(\omega,\tau)=\left|\int E_2(t)\left|E_1(t-\tau)\right|^2 e^{-i\omega t}dt\right|^2 \quad , \tag{28}$$

where E_1 and E_2 are the unknown pulses, I_1 is the PG FROG trace with a gated pulse of $\left|E_2(t-\tau)\right|^2$, and I_2 is the PG FROG trace with gated pulse of $\left|E_1(t-\tau)\right|^2$. Once these two PG FROG traces are available, an iterative phase retrieval program will be used to retrieve the full information of $E_1(t)$ and $E_2(t)$.

This phase retrieval algorithm is based on the Generalized Projection algorithm. For more clear identification, inside the GP algorithm, each loop is named as an iteration, outside the GP algorithm, each loop is named as a cycle.

The algorithm starts with two random initial guess on $E_1(t)$ and $E_2(t)$. In each cycle, the first step is to run the GP algorithm to find a better guess for $E_1(t)$ from $I_1(\omega,\tau)$, the second step is to use this resulting $E_1(t)$ to find a better $E_2(t)$ from $I_2(\omega,\tau)$. The results of these better $E_1(t)$ and $E_2(t)$ are used as guesses for the next cycle. Each cycle results in a slightly better $E_1(t)$ and $E_2(t)$. The PG blind FROG algorithm continues until the resulting PG blind FROG traces match the experimentally generated trace (or until the error between these traces reaches a minimum). Similar to other FROG techniques, we use FROG errors as the criterion to define the convergence of the algorithm. In order to simulate the real experiment environment, we add 1% Poisson noise on each trace. Before the two traces are sent into the retrieval program, the noise deduction is used. The flowchart of the phase retrieval algorithm is shown in Figure 39

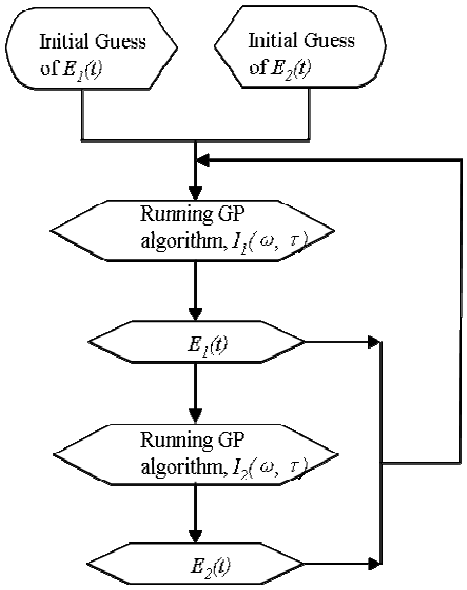

Figure 39. Flow chart of PG Blind FROG Algorithm

. We have showen some simulation examples below. They are ranging from simple pulses to extremely complex pulses. All these pulses are constructed as a function of time. The number of points is different in different examples depending on their complexity. In order to simulate the real experiment environment, we add 1% Poisson noise on each trace. Before the two traces are sent into the retrieval program, noise deduction is used.

(1) Simple Gaussian pulse with flat phase

Here, we represented each pulse with 256 points with a 3-fs time interval between points, while the full-width at half-maximum (FWHM) of the Et_1 is 100 fs and FWHM of Et_2 is 50 fs. Based on the two generated PG FROG traces with 1% Poisson noises added, correct pulses can be retrieved. The result is shown in Figure 40. So, PG blind FROG performs very well for two simple pulses.

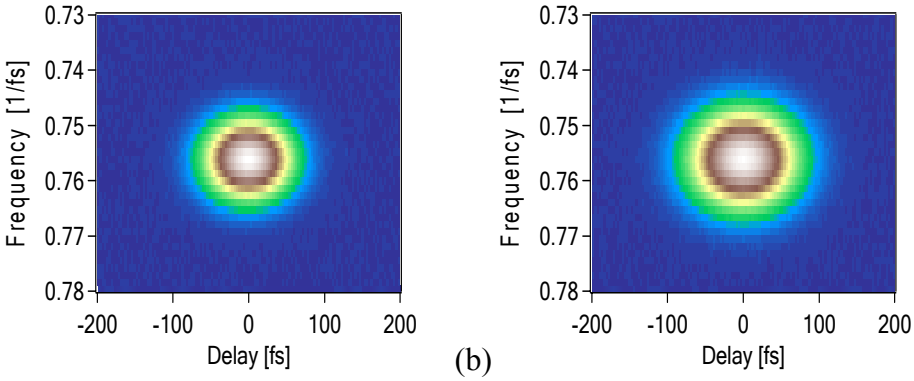

(a) (b)

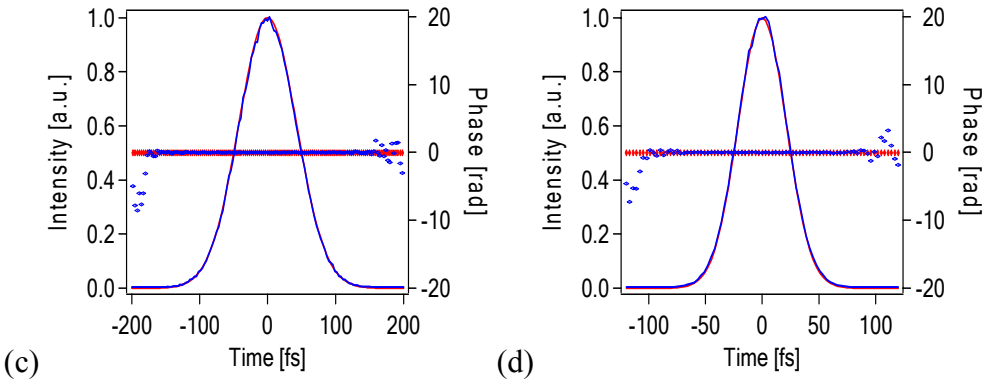

Figure 40. (a) PG blind FROG trace with signal field $E_{sig} = E_2(t)\left|E_1(t-\tau)\right|^2$, (b) PG blind FROG trace with signal field $E_{sig} = E_1(t)\left|E_2(t-\tau)\right|^2$, (c) generated and retrieved $E_1(t)$, (d) generated and retrieved $E_2(t)$. During the retrieval, the FROG errors for $I_1(\omega,\tau)$ and $I_2(\omega,\tau)$ are 2.099e-4 and 3.521e-4, respectively. The initial guess for both pulses are transfer-limited Gaussian pulse with FWHM value of 20 fs.

(2) Two chirped Gaussian pulses.

Based on the pulses in the first example, -50fs^2/rad GVD is added onto Et_1 and 100fs^2/rad GVD is added onto Et_2. Figure 41 shows the simulation result. We see that even for distorted pulses, PG blind FROG works very well.

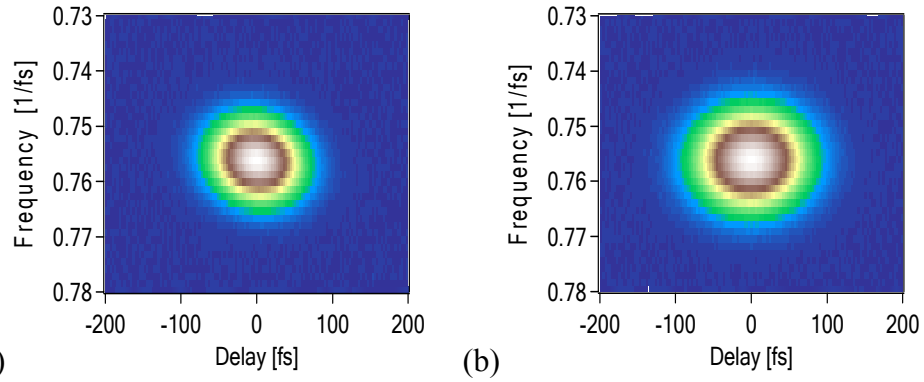

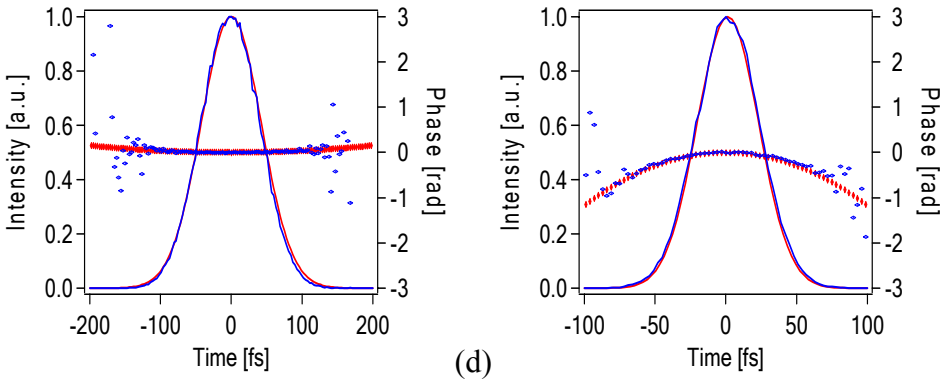

(c) (d)

Figure 41. (a) PG blind FROG trace with signal field $E_{sig} = E_2(t)\left|E_1(t-\tau)\right|^2$, (b) PG blind FROG trace with signal field $E_{sig} = E_1(t)\left|E_2(t-\tau)\right|^2$, (c) generated and retrieved E_1 , (d) generated and retrieved E_2, (c) and (d) are retrieved without any spectrum information. During the retrieval, the FROG errors for $I_1(\omega,\tau)$ and $I_2(\omega,\tau)$ are 8.11e-4 and 1.197e-3, respectively. The initial guess for both pulses is a transfer-limited Gaussian pulse with FWHM value of 20 fs.

(3) One simple pulse and one complex pulse

The simple pulse in this example is same as the Et_1 in the second example. The complex pulse is generated by the method discussed in Chapter 2. The TBP value of this complex pulse is 9.6. PG blind FROG is also able to retrieve this kind of moderately complex pulses. The result is shown in Figure 42

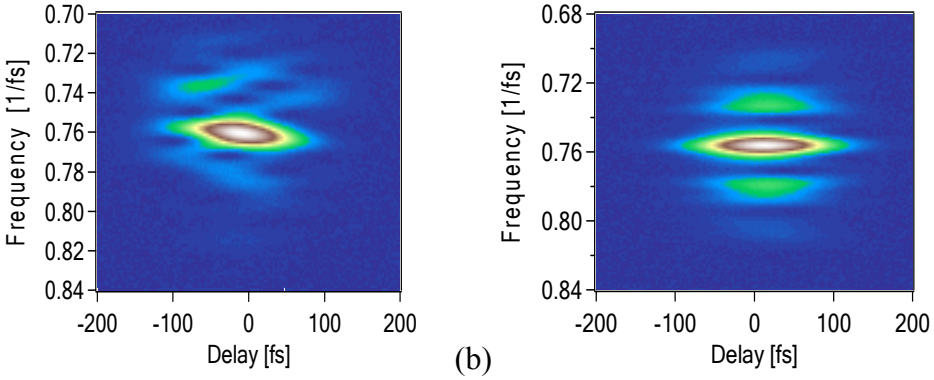

(a) (b)

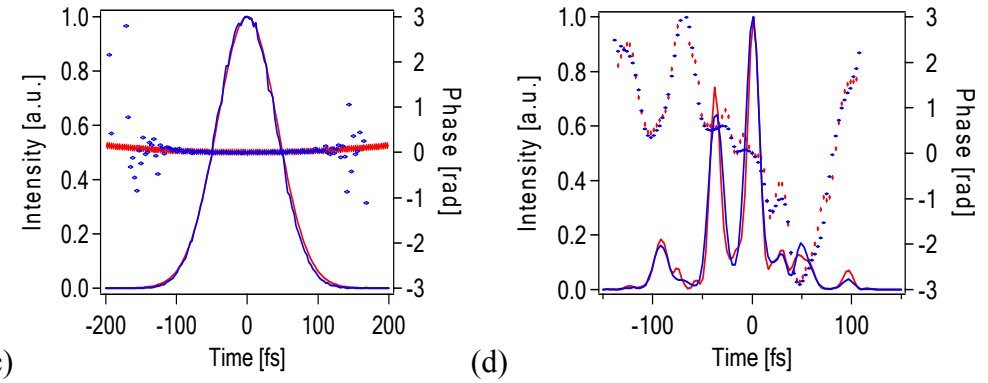

Figure 42. (a) PG blind FROG trace with signal field $E_{sig} = E_2(t)\left|E_1(t-\tau)\right|^2$, (b) PG blind FROG trace with signal field $E_{sig} = E_1(t)\left|E_2(t-\tau)\right|^2$, (c) generated and retrieved E_1 , (d) generated and retrieved E_2, (c) and (d) are retrieved without any spectrum information. During the retrieval, the FROG errors for $I_1(\omega,\tau)$ and $I_2(\omega,\tau)$ are 2.555e-3 and 3.950e-3, respectively. The initial guess for both pulses are random noises.

(4) Two complex pulses

In the examples, we represented each pulse with 512 points with a 3-fs time interval between points. Both Et_1 and Et_2 are complex pulses. Their TBP values are 39.4 and 55.9, respectively. The retrieval result is shown in Figure 43. From Figure 43, we can see that PG blind FROG performs very well for complex pulses.

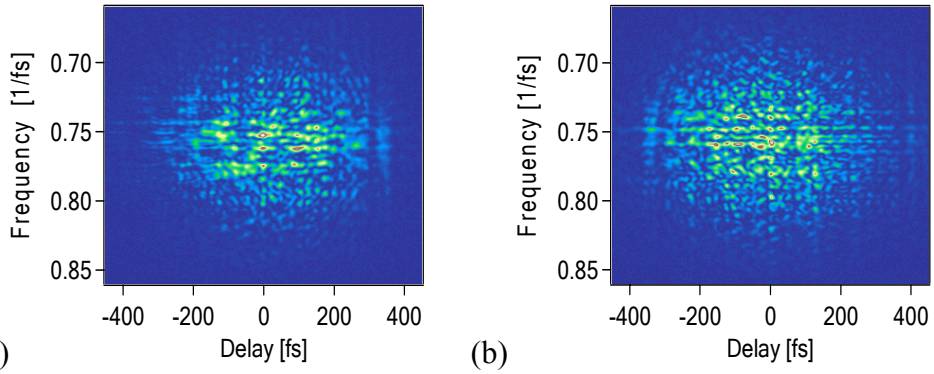

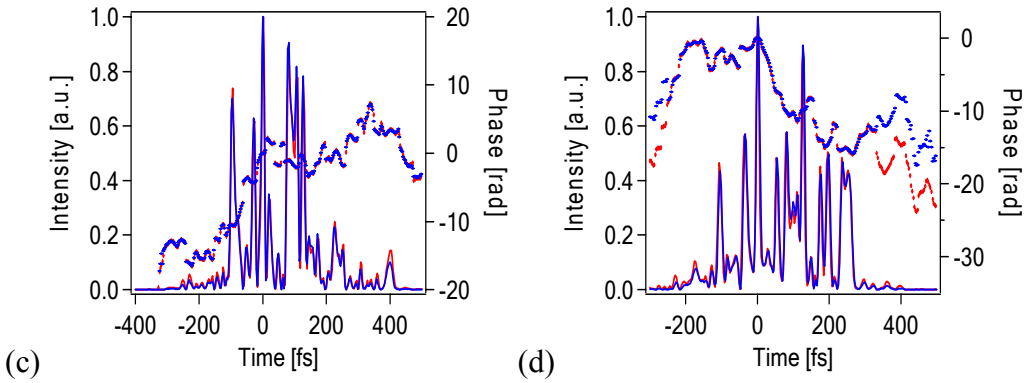

Figure 43. (a) PG blind FROG trace with signal field $E_{sig} = E_2(t)\left|E_1(t-\tau)\right|^2$, (b) PG blind FROG trace with signal field $E_{sig} = E_1(t)\left|E_2(t-\tau)\right|^2$, (c) generated and retrieved E_1 , (d) generated and retrieved E_2, (c) and (d) are retrieved without any spectrum information. During the retrieval, the FROG errors for $I_1(\omega,\tau)$ and $I_2(\omega,\tau)$ are 2.722e-3 and 3.719e-3, respectively. The initial guess for both pulses are random noises.

(5) Two extremely complex pulses

In the examples, we represented each pulse with 1024 points with a 3-fs time interval between points. Both Et_1 and Et_2 are extremely complex pulses. Their TBP values are 82.4 and 107.3, respectively. The retrieved result is shown in Figure 44. From this Figure 44, we can see that PG blind FROG performs very well for such extremely complex pulses.

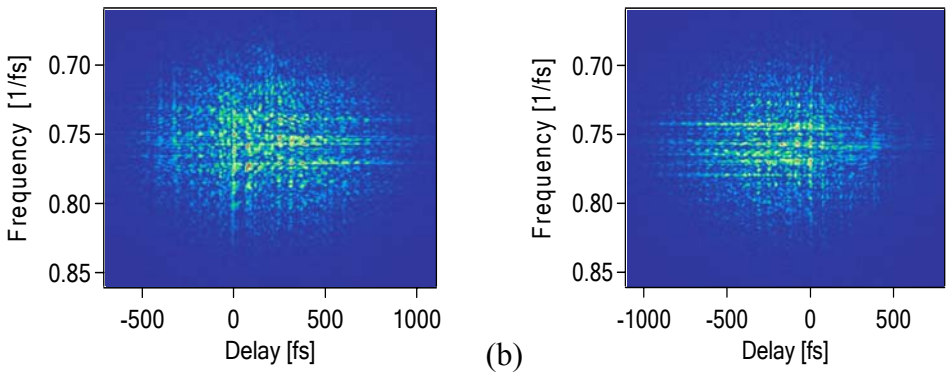

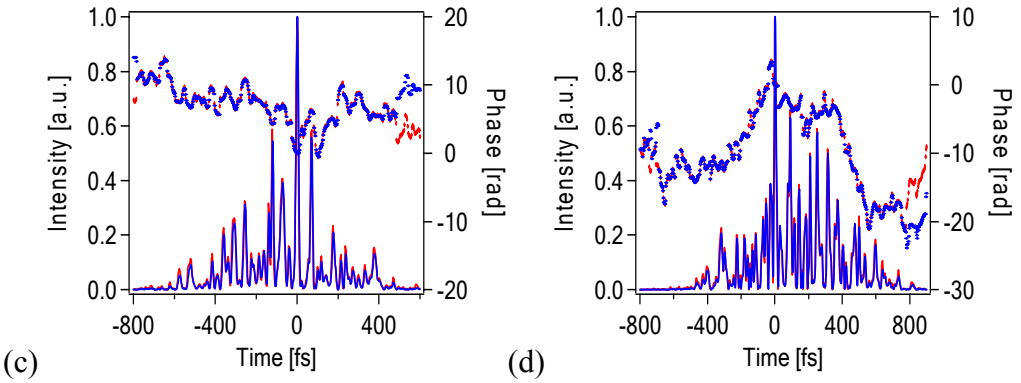

Figure 44. (a) PG blind FROG trace with signal field $E_{sig} = E_2(t)\left|E_1(t-\tau)\right|^2$, (b) PG blind FROG trace with signal field $E_{sig} = E_1(t)\left|E_2(t-\tau)\right|^2$, (c) generated and retrieved E_1 , (d) generated and retrieved E_2, (c) and (d) are retrieved without any spectrum information. During the retrieval, the FROG errors for $I_1(\omega,\tau)$ and $I_2(\omega,\tau)$ are 2.69e-3 and 2.425e-3, respectively. The initial guess for both pulses are random noises.

6.3 Discussion

Since PG blind FROG is based on PG FROG, no ambiguity issue is found. The phase information of the probe pulse is contained in the corresponding PG FROG trace. It inherits the advantages and disadvantages of PG FROG, such as characterizing the pulse uniquely, except the zero order and first order phase. The nonlinear-optical process is automatically phase-matched. Two consequences result: (1) alignment is easy; and (2) PG FROG has a broad bandwidth. Therefore, PG blind FROG is an ideal technique to measure both broadband and complex pulses.

One disadvantage of PG blind FROG is that it requires a high-quality polarizer, which is very expensive. In addition, a high-quality polarizer tends to be thick, which spreads the pulse in time as a result of material dispersion. Furthermore, polarizers are not available in the spectral region of the deep UV(<~250nm). This limits the usage of PG blind FROG in the UV region. However, there is a plethora of research and industrial applications (telecommunications, medical imaging, etc) which operate in the visible and

near-IR region, which ensures the usefulness of this robust technique. A second disadvantage of PG blind FROG is the power issue. Since it involves third order nonlinearity, a lower output power is yielded by weaker or longer pulse. This is only a slight disadvantage and will become even more minimal as the average power of ultrafast lasers increases with the advances in technology.

Overall, TG double blind FROG is an ideal technique to measure two complex pulses simultaneously in visible and near IR region.

6.4 Conclusion

PG blind FROG is a versatile and robust technique to measure two pulses simultaneously without nontrivial ambiguities. Due to its advantages, it is ideal to measure very complex pulses and super continuum without any additional information of the spectrum.

APPENDIX 1

NELDER-MEAD METHOD

Nelder-Mead (NM) method is also named as down hill simplex method. It inherits the concept of simplex method and used to minimize an objective function in a many-dimensional space for nonlinear problems. In TURTLE technique, the objective function is

$$f(\theta,\tau)=\frac{\sqrt{\sum_{i,j=1}^{N}\left[I_{\eta}^{meas}(i,j)-I_{\eta}^{calc}(i,j)\right]^{2}}}{\sqrt{\sum_{i,j=1}^{N}\left[I_{\eta}^{meas}(i,j)\right]^{2}}}$$

This equation is obvious nonlinear and the two unknowns are θ and τ. Since NM method's initial condition is same as simplex method that if we have one variable, a line segment is needed; if we have two variables, we need a triangle. This means three sets of variables are needed as the initial guess to form a triangle. In other words, our initial guess should be three vertices. Since variables in TURTLE are θ and τ, the initial guess is $V_k=(\theta_k,\tau_k),\ k=1,2,3$

Then, we evaluate the objective function by these three sets of initial guesses and order these three resulting values of the objective function. $f(\theta_1,\tau_1)\le f(\theta_2,\tau_2)\le f(\theta_3,\tau_3)$. For convenience, we define

$B=(\theta_1,\tau_1)\qquad G=(\theta_2,\tau_2)\qquad W=(\theta_3,\tau_3)$

B means the best vertex, G means good vertex and W means worse vertex. Since the values at B and G are better than at W, the minimization direction should either be along BG or on the other side of BG relative to W. The next step is finding the midpoint M along BG.

$$M = (\frac{\theta_1 + \theta_2}{2}, \frac{\tau_1 + \tau_2}{2})$$

The value of f decreases from W to B and from W to G, so we suppose the feasible region is on the other side of the triangle along BG. This new point R is the reflected point of W along BG. But the line of WR is not perpendicular to BG. To obtain point R, we have to connect WM and extend WM to R. The length of RM is same as WM.

$$R = M + (M - W) = 2M - W = (\theta_1 + \theta_2 - \theta_3, \tau_1 + \tau_2 - \tau_3)$$

If the value of $f(R)$ is less than $f(W)$, we have moved into the correct direction toward the minimum. The new triangle is BGR. Then, we extend R further to obtain a better value. What we need to do is extending MR further to point E. The distance of ER is same as the distance of MR. therefore, we will obtain

$$E = R + (R - M) = 2R - M = (\frac{3(\theta_1 + \theta_2)}{2} - \theta_3, \frac{3(\tau_1 + \tau_2)}{2} - \tau_3)$$

If the value of $f(E)$ is less than $f(R)$, we have a new vertex, and the newer triangle is BGE. Then, iteratively repeating these steps can obtain the minimum.

On the other hand, if the value of $f(R)$ is same as $f(W)$, we can not form a new triangle and replace W with R. We have to use another two midpoints, one is the midpoint of WB and the other is the midpoint of WG. After comparing the vale of f at these two midpoints, we will choose the midpoints which yields lower f. A new triangle is formed by BG and this new midpoint. If both values at the midpoints are greater

than $f(W)$, then a new triangle is form by BM and the midpoint of BW. After the new triangle is formed, we repeat the step from the beginning. The point W is replaced and forms a new triangle for next searching until the criteria is met.

REFERENCES

1. Lepetit L., Cheriaux G. and Joffre M., Linear techniques of phase measurement by femtosecond spectral interferometry for applications in spectroscopy. J. Opt. Soc. Am. B. 12,12: p. 2467,1995.

2. Fittinghoff David N., Bowie Jason L., Sweetser John N., Jennings Richard T., Krumbuugel Marco A., Delong Kenneth W., Trebino Rick and Walmsley Ian A., Measurement of the intensity and phase of ultraweak, ultrashort laser pulses. Opt. Lett. 21,12: p. 884,1996.

3. Walmsley C. Iaconis and I. A., Spectral phase interferometry for direct electric-field reconstruction of ultrashort optical pulses. Optics Letters. 23: p. 792,1998.

4. Rick Trebino Daniel J. Kane, Using phase retrieval to measure the intensity and phase of ultrashort pulses: Frequency-resolved optical gating. J. Opt. Soc. Am. A. 10,1993.

5. Kosik Ellen M., Radunsky Aleksander S., Walmsley Ian A. and Dorrer Christophe, Interferometric technique for measuring broadband ultrashort pulsesat the sampling limit. Opt. Lett. 30,3: p. 326,2005.

6. Baum Peter, Lochbrunner Stefan and Riedle Eberhard, Zero-additional-phase spider: Full characterization of visible and sub-20-fs ultraviolet pulses. Opt. Lett. 29,2: p. 210,2004.

7. Maier M., W. Kaise, and J.A. Giordmaine, Ultrashort pulsewidth laser ranging system employing a time gate producing an autocorrelation and method therefore. Phys. Rev. Lett. 17,1966.

8. Kintzer E. S. And Rempel, C., Near-surface second-harmonic generation for autocorrelation measurements in the uv. Appl. Phys. B. 42,2: p. 91,1987.

9. Kenneth L. Sala Geraldine A. Kenney-Wallace, and Gregory E. Hall, Cw autocorrelation measurements of icosecond laser pulses. IEEE J. Quan. Elec. 16,1980.

10. Wyatt R., and Marinero, E. E., Versatile single-shot background-free pulse duration measurement technique, for pulses of subnanosecond to picosec-ond duration. Appl. Phys. . 25: p. 297,1981.

11. K. W. Delong and Rick Trebino J. Hunter and W. E. White, Frequency-resolved optical gating with the use of second-harmonic generation. J. Opt. Soc. Am. B. 11,1994.

12. Delong K., Fittinghoff, D., Trebino, R., Sullivan, A., Hunter, J.,White, W., and Kane, D., Frequency-resolved optical gating: Measuring the intensity and phase of an ultrashort laser pulse. Ultrafast Phenomena IX (Barbara, P., Knox, W., Mourou, G., and Zewail, A., eds.), Springer Series in Chemical Physics: p. 127,1994.

13. Kane D., Taylor, A., Trebino, R., and Delong, K., Single-shot measurement of the intensity and phase of femtosecond uv laser pulse using frequency-resolved optical gating. Opt. Lett. 19: p. 1061,1994.

14. Kane D. And Trebino, R., Characterization of arbitrary femtosecond pulses using frequency resolved optical gating. IEEE J. Quan. Elec. 29: p. 571,1993.

15. Kane D. And Trebino, R., Single-shot measurement of the intensity and phase of a femtosecond pulse," In ultrafast pulse generation and spectroscopy. Bellingham: SPIE Press. 1861: p. 18,1993.

16. Trebino Rick, Frequency-resolved optical gating: The measurement of ultrashort laser pulses. Kluwer Academic Publishers 2002.

17. Iaconis C. And Walmsley, I. A., Self-referencing spectral interferometry for measuring ultrashort optical pulses. IEEE J. Quan. Elec. 35: p. 501,1999.

18. E. Tokunaga and A. Terasaki T. Kobayashi*, Frequency-domain interferometer for femtosecond time-resolved phase spectroscopy. Optics Letters. 17,1992.

19. Christophe Dorrer Nadia Belabas, Jean-Pierre Likforman, and Manuel Joffre, Spectral resolution and sampling issues in fourier-transform spectral interferometry. J.Opt.Soc.Am.B. 17,2000.

20. E. Zeek A.P. Shreenath, P. O'shea, M. Kimmel, R. Trebino, Simultaneous automatic calibration and direction-of-time removal in frequency-resolved optical gating. Appl. Phys. B. 74,2002.

21. Kenneth W. Delong David N. Fittinghoff, Rick Trebino, Bern Kohler, Kent Wilson, Pulse retrieval in frequency-resolved optical gating based on the method of generalized projections. Optics Letters. 19: p. 2152,1994.

22. Jain A., Fundamentals of digital inage processing. Upper Saddle River, NJ: Prentice-Hall, Inc,1989.

23. Stark H, Image recovery: Theory and application. Orlando: Academic Press,1987.

24. Yudilevich E., Levi, A., Habetler, G. J., and Stark, H., Restora-tion of signals from their signed fourier-transform magnitude by the method of generalized projections. Journal of the Optical Society of America B-Optical Physics A-Optics, Image Science and Vision. 4: p. 236,1987.

25. Rick Trebino Kenneth W. Delong, David N. Fittinghoff, John N. Sweetser, Marco A. Krumbügel, Bruce A. Richman and Daniel J. Kane, Measuring ultrashort laser pulses in the time-frequency domain using frequency-resolved optical gating. Rev. Sci. Instrum. 68,1997.

26. S. Linden H. Giessen, and J. Kuhl, Xfrog - a new method for amplitude and phase characterization of weak ultrashort pulses. Phys.stat.sol. (B). 206,1998.

27. John N. Sweetser David N. Fittinghoff, and Rick Trebino, Transient-grating frequency-resolved optical gating. optics Letters. 22,1997.

28. Dongjoo Lee Selcuk Akturk, Pablo Gabolde, and Rick Trebino, Experimentally simple, extremely broadband transient-grating frequency-resolved-opticalgating arrangement. OPTICS EXPRESS. 15,2007.

29. Boyd R, Nonlinear optics. Academic Press,2003.

30. Dorine Keusters Howe-Siang Tan, Patrick O'shea, Erik Zeek, Rick Trebino, Warren S. Warren, Relative-phase ambiguities in measurements of ultrashort pulses with well-separated multiple frequency components. J. Opt. Soc. Am. B. 20,2003.

31. Akturk S., Kimmel, M., O'shea, P., Tebino, R., Naumov, S., Sorokin, E., and Sorokina, I., Measuring several-cycle 1.5-m pulses using frequency-resolved optical gating. Opt. Express. 11: p. 3461,2003.

32. L.Xu E.Zeek, and R. Trebino, Simulations of frequency-resolved optical gating for measuring very complex pulses. J. Opt. Soc. Am. B. 25: p. A70,2008.

33. K. W. Delong Rick Trebino and Daniel J. Kane, Comparison of ultrashort-pulse frequency-resolved-optical-gating traces for three common beam geometries. J.Opt.Soc.Am.B. 11: p. 1595,1994.

34. S. Linden J. Kuhl, and H. Giessen, Amplitude and phase characterization of weak blue ultrashort pulses by downconversion. Opt. Lett. 24,1999.

35. Jennifer P. Ogilvie Delphine Débarre, Xavier Solinas, Jean-Louis Martin, Emmanuel Beaurepaire And and Joffre Manuel, Use of coherent control for selective two-photon fluorescence microscopy in live organisms. Opt. Express. 14: p. 759,2006.

36. A. M. Weiner J. P. Heritage, and J. A. Salehi, Encoding and decoding of femtosecond pulses. Opt. Lett. 13: p. 300,1998.

37. I.H Chowdhury Xianfan Xu, and A.M. Weiner, Laser machining using temporally controlled ultrafast pulses. CLEO. 2,2004.

38. C. J. Bardeen V. V.Yakovlev, J. A.Squier, K. R. Wilson, S. D. Carpenter, P. M.Weber, Effect of pulse shape on the efficiency of multiphoton process: Implications for biological microscopy. J. Biomedical Opt. 4: p. 362,1999.

39. A.M.Weiner, Femtosecond pulse shaping using spatial light modulators. Rev. Sci. Instr. 71: p. 1929,2000.

40. Erik Zeek Kira Maginnis, Sterling Backus, Ulrich Russek, Margaret Murnane,G´Erard Mourou, Henry Kapteyn, and Gleb Vdovin, Pulse compression by use of deformable mirrors. Opt.Lett. 24: p. 493,1999.

41. C. W. Hillegas J. X. Tull, D. Goswami, D. Strickland, and W. S. Warren, Femtosecond laser pulse shaping by use of microsecond radio-frequency pulses. opt. Lett. 19: p. 737,1999.

42. E. Frumker E. Tal, and Y. Silberberg, and D. Majer, Femtosecond pulse-shape modulation at nanosecond rates. Opt. Lett. 30: p. 2796,2005.

43. E. Frumker D. Oron, D. Mandelik, and Y. Silberberg, Femtosecond pulse-shape modulation at kilohertz rates. opt. Lett. 29,2004.

44. Xun Gu Lin Xu, Mark Kimmel, Erik Zeek, Patrick O'shea, Aparna P. Shreenath, Rick Trebino, and Robert S. Windeler, Frequency-resolved optical gating and single-shot spectral measurements reveal fine structure in microstructure-fiber continuum. Opt. Lett. 27: p. 1174,2002.

45. V. V. Lozovoy I. Pastirk, and M. , Multiphoton intrapulse interference. Pulse spectral phase characterization and compensation. Optics Letters. 29: p. 775,2004.

46. Pamela Bowlan Pablo Gabolde, Aparna Shreenath, Kristan Mcgresham, Rick Trebino, and Selcuk Akturk, Crossed-beam spectral interferometry: A simple, high-spectral-resolution method for completely characterizing complex ultrashort pulses in real time. Opt. Express. 14,2006.

47. Andrius Baltu˘Ska Maxim S. Pshenichnikov, and Douwe A. Wiersma, Amplitude and phase characterization of 4.5-fs pulses by frequency-resolved optical gating. Opt. Lett. 23: p. 1474,1998.

48. Altes Richard A., Detection, estimation, and classification with spectrograms. J. Acoust. Soc. Am. 67: p. 1232,1980.

49. Kane Daniel J., Real-time measurement of ultrashort laser pulses using principal component generalized projections. IEEE Journal of Selected Topics in Quantum Electronics 4: p. 278,1998.

50. Cohen L., Time-frequency analysis. Englewood Cliffs, NJ: Prentice-Hall,1995.

51. David N. Fittinghoff Kenneth W. Delong, Rick Trebino, and Celso L. Ladera, Noise sensitivity in frequency-resolved optical-gating measurements of ultrashort pulses. J. Opt. Soc. Am. B. 12: p. 1955,1995.

52. Boor Carl De, A practical guide to splines New York : Springer-Verlag,1978.

53. Papoulis Athanasios, The fourier integral and its applications. New York : Springer-Verlag,1987.

54. Wiener N, Extrapolation, interpolation, and smoothing of stationary time series. New York: Wiley,1949.

55. Deng G., and Cahill, L.W, An adaptive gaussian filter for noise reduction and edge detection. Nuclear Science Symposium and Medical Imaging Conference. 13,1993.

56. Jansson P, Deconvolution of images and spectra. New York : Academic Press,1997.

57. Allen Jont B., Short term spectral analysis, synthesis, and modification by discrete fourier transform IEEE TRANSACTIONS ON ACOUSTICS, SPEECH, AND SIGNAL PROCESSING. 25,3: p. 235,1977.

58. Kuo Bahram Javidi and Chung-Jung, Joint transform image correlation using a binary spatial light modulator at the fourier plane. Appl. Opt. 27: p. 663,1988.

59. Gating Practical Issues in Ultrashort-Laser-Pulse Measurement Using Frequency-Resolved Optical, Practical issues in ultrashort-laser-pulse measurement using frequency-resolved optical gating. IEEE J. Quant. Electron. 32: p. 1253,1996.

60. W. H. Press W.T. Vetterling, and S. A. Teukolsky, Numerical recipes. Cambridge, U.K: Cambridge Univ. Press,1992.

61. Martinez Juan L. A. Chilla and Oscar E., Direct determination of the amplitude and the phase of femtosecond light pulses. Opt. Lett. 16: p. 39,1991.

62. Balakishore Yellampalle * Kiyong Kim, and Antoniette J. Taylor, Amplitude ambiguities in second-harmonic generation frequency-resolved optical gating. Optics Letters. 32,2007.

63. R. P. Scott , N. K. Fontaine, Jing Cao, Katsu Okamoto, B. H. Kolner, J. P. Heritage, and S. J. Ben Yoo, High-fidelity line-by-line optical waveform generation and complete characterization using frog. Opt. Express. 15,2007.

64. C. W. Siders A. J. Taylor, and M. C. Downer, Multipulse interferometric frequency-resolved optical gating: Real-time phase-sensitive imaging of ultrafast dynamics. Opt. Lett. 22: p. 624,1997.

65. Craig W. Siders Jennifer L. W. Siders, Fiorenzo G. Omenetto, and Antoinette J. Taylor, Multipulse interferometric frequency-resolved optical gating. IEEE J. Quan. Elec. 35: p. 432,1999.

66. Rundquist J. Peatross and A., Temporal decorrelation of short laser pulses. J. Opt. Soc. Am. B. 15: p. 216,1998.

67. Jung-Ho Chung Andrew M. Weiner, Ambiguity of ultrashort pulse shapes retrieved from the intensity autocorrelation and the power spectrum. IEEE JOURNAL ON SELECTED TOPICS IN QUANTUM ELECTRONICS. 7,2001.

68. Kazunori Naganuma Kazuo Mogi, and Hajime Yamada, General method for ultrashort light pulse chirp measurement. IEEE JOURNAL OF QUANrUM ELECTRONICS. 25,6,1989.

69. Warren S. Warren Herschel Rabitz, and Mohammed Dahleh, Coherent control of quantum dynamics: The dream is alive Science. 259: p. 1581,1993.

70. T. Brixner G. Krampert, T. Pfeifer, R. Selle, G. Gerber, M .Wollenhaupt, O. Graefe, C. Horn, D. Liese, and T. Baumert, Quantum control by ultrafast polarization shaping. Phys. Rev. Lett. 92,2004.

71. T.Brixner N.H.Damrauer, G.Krampert, P.Niklaus, and G.Gerber, Adaptive shaping of femtosecond polarization profiles. J. Opt. Soc. Am. B. 20,2003.

72. T. Suzuki S. Minemoto, T. Kanai, and H. Sakai, Optimal control of multiphoton ionization process in aligned i2 molecules with time-dependant polarization pulses. Phys. Rev. Lett. 92,13: p. 133005,2004.

73. M. Kakehata R. Ueda, H. Takada, K. Torizuka, and M. Obara, Combination of high-intensity femtosecond laser pulses for generation of time-dependent polarization pulses and ionization of atomic gas. Appl. Phys. B. 70,2000.

74. Eric Constant Vladimir D. Taranukhin, Albert Stolow, and P.B. Corkum, Methods for the measurement of the duration of high-harmonic pulses. Physical Review A. 56,5,1997.

75. Marc M. Wdfers Hitoshi Kawashima, and Keith A. Nelson, Optical control over two-dimensional lattice vibrational trajectories in crystalline quartz. J. Chem. Phys. 108: p. 10248,1998.

76. David Kupka Philip Schlup, and Randy A. Bartels, Simplified polarization pulse shaper using a birefringent prism. Rev. Sci. Instruments accepted for publication,2009.

77. Mateusz Plewicki Fabian Weise, Stefan M. Weber, and Albrecht Lindinger, Phase, amplitude, and polarization shaping with a pulse shaper in a mach-zehnder interferometer. Applied Optics. 45,32,2006.

78. Gerber T. Brixner and G., Femtosecond polarization pulse shaping. Optics Letters. 26,2001.

79. Omid Masihzadeh Philip Schlup, and Randy A. Bartels, Complete polarization state control of ultrafast laser pulses with a single linear spatial light modulator. Optics express. 15,26,2007.

80. A. E. Paul J. A. Bolger, and Arthur L. Smirl, J. G. Pellegrino, Time-resolved measurements of the polarization state of four-wave mixing signals from gaas multiple quantum wells. J. Opt. Soc. Am. B. 13,1996.

81. J. A. Bolger A. E. Paul, and Arthur L. Smirl, Ultrafast ellipsometry of coherent processes and exciton-exciton interactions in quantum wells at negative delays. Phys. Rev. B. 54,1996.

82. W. J.Walecki D. N. Fittingho, A. L. Smirl and R. Trebino, Characterization of the polarization state of weak ultrashort coherent signals by dual-channel spectral interferometry. Opt. Lett. 22: p. 81,1997.

83. J. Piasecki B. Colombeau, M. Vampouille, C. Froehly, and J. A. Arnaud, Nouvelle methode de mesure de la reponse impulsionnelle des fibres optiques. Appl. Opt. 19: p. 3749,1980.

84. Haas B., Determination of weak optical pulses in amplitude and phase by measurement of the transient polarization state. Opt. Lett. 24: p. 543,1999.

85. Juan José Ferreiro Raúl De La Fuente, and Elena López-Lago, Characterization of arbitrarily polarized ultrashort laser pulses by cross-phase modulation. Opt. Lett. 26: p. 1025,2001.

86. Philip Schlup Omid Masihzadeh, Lina Xu, Rick Trebino, and Randy A. Bartel, Tomographic retrieval of the polarization state of an ultrafast laser pulse. Opt. Lett. 33: p. 267,2008.

87. Lagarias J.C., J. A. Reeds, M. H. Wright, and P. E. Wright, Convergence properties of the nelder-mead simplex method in low dimensions. SIAM Journal of Optimization. 9: p. 112,1998.

88. Saari Arvi Freiberg and Peeter, Picosecond spectrochronography. IEEE J. Quan. Elec. 19,1983.

89. M.-A. Mycek S. Weiss, J.-Y. Bigot, S. Schmitt-Rink, D. S. Chemla, and W. Schaefer, Femtosecond time-resolved free-induction decay of room-temperature excitons in gaas quantum wells. Appl. Phys. Lett. 60,21,1992.

90. Kenneth W. Delong Rick Trebino, and William E. White, Simultaneous recovery of two ultrashort laser pulses from a single spectrogram. J. Opt. Soc. Am. B. 12,12,1995.

91. Rodenburg B. C. Mccallum and J. M., Simultaneous reconstruction of object and aperture functions from multiple far-field intensity measurements. J. Opt. Soc. Am. A. 10,2,1993.

92. Daniel J. Kane G. Rodriguez, A. J. Taylor, and Tracy Sharp Clement, Simultaneous measurement of two ultrashort laser pulses from a single spectrogram in a single shot. J. Opt. Soc. Am. B. 14,1997.

VITA

Lina Xu was born in Beijing, P. R. China. She received the degree of Bachelor of Science in Optoelectronics from Chongqing University, Chongqing, China, 2001. She received her Master of Science in Physics from Mississippi State University, US, 2004. She came to the school of Physics, Georgia Institute of Technology, Atlanta, USA to pursue her PhD degree in 2005. She joined Dr. Rick Trebino's group in 2005.